The copyright of this thesis rests with the University of Cape Town. No quotation from it or information derived from it is to be published without full acknowledgement of the source. The thesis is to be used for private study or non-commercial research purposes only.

University of Cape Town

UNIVERSITY OF CAPE TOWN

CHRIS BARNARD DIVISION OF CARDIO-THORACIC SURGERY:
CARDIOVASCULAR RESEARCH UNIT

IN VIVO MECHANICAL LOADING CONDITIONS OF PECTORALLY IMPLANTED CARDIAC PACEMAKERS:

FEASIBILITY OF A FORCE MEASUREMENT SYSTEM AND CONCEPT OF AN ANIMAL-HUMAN TRANSFER FUNCTION

SUBMITTED TO THE UNIVERSITY OF CAPE TOWN IN PARTIAL FULFILMENT OF THE REQUIREMENTS FOR THE DEGREE
MSC (MED) IN BIOMEDICAL ENGINEERING

AUTHOR : MICHAEL HAMMAN DE VAAL

SUPERVISOR: DR. THOMAS FRANZ

DATE: 12 NOVEMBER 2009

Declaration

I, *Michael Hamman de Vaal (South African ID: 8210035123089)*, hereby declare that the work on which this dissertation is based is my original work (except where acknowledgements indicate otherwise) and that neither the whole work nor any part of it has been, is being, or is to be submitted for another degree in this or any other university.

I empower the university to reproduce for the purpose of research either the whole or any portion of the contents in any manner whatsoever.

Signature: ……

Date: ……

Dedication

The “kick” of scientific discovery and education wanes, wears off and is ultimately unsustainable without the emotional support of interpersonal relationships made possible by the grace of God through His son, Jesus Christ. This piece of work, how intermediate or imperfect it might be, is a dedication to this fact. *Soli Deo Gloria!*

Acknowledgements

This thesis was prepared at the Cardiovascular Research Unit of the Chris Barnard Division of Cardio-Thoracic Surgery.

First of all, my great appreciation and thanks goes out to my supervisor, Dr. Thomas Franz, for good communication, maintaining high levels of excellence, an open door policy, prompt and thorough feedback, epic long meetings wrestling with various concepts and explanations, and for trying to teach me the balance between perfection and getting the work done.

On the side of our research collaborators, I would like to thank Mr. Jim Neville and Mr. Micah Litow. Thank you very much for being willing to include me in this project, as well as for your helpful comments throughout. I am privileged to have met you and to have had the chance to pick your brains in order to learn from your many years working in industry.

To Prof. Peter Zilla, thank you very much for facilitating a great working environment: stimulating and fun to work in.

For a number of people providing essential assistance to this project: Thank you very much to Dr. Paul Human and Mr. Rauf Sayed for statistical advice, Mrs. Melanie Black and Mrs. Subash Padayache for performing the histology, Prof. Peter Zilla for histological assessment, Mr. Bruno Orlandi for making with Instron fittings, and also Prof. Stephen Beningfield, Ms. Patronella Samuels, Ms. Sharon Heyne and Ms. Nazlea Behardien-Peters for enabling and conducting MRI and CT imaging.

On a personal note, I would like to extend my utmost thanks to my parents, siblings, girlfriend, friends, CVRU colleagues and my girlfriend's family (the Leydens). I want to make special mention of a few people (apart from emotional support): Pa (financial support), Ma ("*yster*" proofreading), Mirelle (Kisses and arms, Sundays and work-dinners), Alma (many late night studies), Bern (temp office space), Karen (all-day write-ups), Albert (lunches), Hugo (climbing), Coos (telling it like it is), Corver (*swemmies*), Letchemie and Jenny (Monday lunchtimes), Ross, Dr. Warton etc. (insightful conversations), friends at Shofar Cape Town (encouragement) and the Straatligkinders (musical support).

Summary

The need for smaller implantable cardiac pacemakers (pacemakers) has increased the mechanical loading demand placed on current and future devices. Knowledge about *in vivo* mechanical loading is required for improved mechanical design of pacemakers. A measurement system for investigating *in vivo* mechanical loading on a pectorally implanted pacemaker was developed by research collaborators. This system featured implantable instrumented pacemakers (IPM) capable of measuring *in vivo* contact force and acceleration data, and transmitting this data wirelessly.

The objectives of this study were to assess the feasibility of this system for measuring *in vivo* mechanical loading on pectorally implanted pacemakers, to compare differences in mechanical loading experienced by pacemakers in different pectoral implant positions (i.e. sub-muscular and sub-coetaneous) and to formulate a concept of an interspecific transfer function for predicting the *in vivo* mechanical loads on sub-muscularly implanted pacemakers in humans, by using data obtained from baboons.

Six IPMs were implanted bilaterally in the sub-muscular and sub-coetaneous positions in three adult male Chacma baboons. After sufficient healing (8 weeks), data were obtained from various experiments performed on the conscious and anaesthetized baboon.

Analysis of the acquired data revealed the feasibility of using this measurement system for measuring *in vivo* mechanical loading on pacemakers. This was based on the adequate design of the measurement system in terms of its wireless data acquisitioning capabilities, its ability to synchronize *in vivo* force measurement with real-time video data, good force responsiveness, good force measurement repeatability and acceptable force measurement accuracy. The Tekscan contact force sensors used yielded good repeatability as was evident from the low variation of the *in vivo* reference measurements: 4.1±2.9, 3.8±4.0, 3.9±1.6 and 4.7±2.1%, respectively, for all 6 sensors per IPM (acquired during conscious activities over an eight day period). Despite the inability to verify the *in vivo* force measurement accuracy of these sensors, it was deemed acceptable based on extensive preconditioning and calibration procedures performed, comparable *in vivo* forces measured between different IPMs, development of a comprehensive voltage-force conversion method (that accommodated for sensor drift and disregarded unfiltered RF noise spikes) and other indirect methods of evaluation. Suggested improvements to the measurement system and associated experiments include improving the assembly of the sensors onto the IPM, increased control over parameters involved in voltage-force conversion and adjusting surgical techniques for optimal healing of sub-coetaneous implants.

Experimental sample sizes from this feasibility study did not allow for the acquisition of statistically significant results (n = 3 sub-muscular, n = 1 sub-coetaneous). However, results provided valuable insight into *in vivo* forces experienced by pacemakers that have not been measured before. It was found that the force experienced by each IPM was subject-specific, depending on geometry, tension in and compression of the structures surrounding the implanted device. Considering conscious activities, (1) While the force increased with the intensity of the movements, the data obtained did not allow a clear ranking of specific movements (e.g. pushing or pulling) or of the specific position of the arm (excluding the adducted arm) with regard to the force placed on the implant, (2) for both implant positions, higher force events occurred infrequently (95% of force data fell between 0.8 and

1.2 of resting force), and resting forces were comparable, (3) a more severe loading distribution was measured by the sub-muscular IPMs (higher frequency at higher magnitudes), compared to sub-coetaneous IPMs, and (4) maximum forces were up to five times the resting force. The effect of conscious muscle tone was observed in the decrease of resting force from the conscious to the anaesthetized animals, a decrease of 32%, 34% and 49%, respectively, for the three sub-muscular devices and 10% for the sub-coetaneous device.

The formulation of the concept of an interspecific transfer function was based on determining if a relationship existed between the in-line muscle force, morphometric parameters and force experienced by an IPM in baboons – and if this relationship applied in humans. Baboons were considered to be the most suited laboratory animal for this application, based on shoulder anatomy and morphology similar to humans. Using data acquired from baboons, a multiple linear regression analysis was performed with the force measured by the IPMs as the response and different combinations of other relevant parameters as the regressors. An $R^2 = 0.71$ (n = 51) was obtained from four IPMs considered and deemed reasonable based on a follow-up analysis that showed the mechanical soundness of the correlation. Regressors that significantly correlated with the response (total force measured by the IPM) included the in-line muscle force, in-line muscle tension, width of the muscle over the IPM and measured muscle length; all parameters of the *pectoralis major* muscle overlying the subM IPM. This relationship was shown to be suitable to use with human data, on the condition that the predicted force on an IPM in humans is corrected for the difference in angles of muscle attachment between the two species. It is suggested that additional parameters, identified in this study, be included in future considerations of this interspecific transfer function. Upon validation of this concept in future studies, the in-line muscle force and morphometric parameters only need to be measured or estimated in humans to be able to predict subject-specific *in vivo* mechanical loading on pacemakers in humans. Furthermore, validation of this concept implies that no further animal experimentation will be required.

Table of contents

LIST OF ABBREVIATIONS X

LIST OF SYMBOLS XI

LIST OF FIGURES XV

LIST OF TABLES XX

1. INTRODUCTION 1

1.1. Background and motivation 1

1.2. Objectives 3

2. LITERATURE REVIEW AND THEORY 4

2.1. Implantable cardiac pacemaker devices 4

2.1.1. Description, function and extent of use 4

2.1.2. System designs 4

2.2. Implantation of pacemakers 5

2.3. Skeletal muscle 7

2.3.1. Function, form and physiology 7

2.3.2. Activation of muscle 9

2.3.3. Force generating properties 10

2.3.4. Measurement of force developed in muscle 11

2.3.5. Musculoskeletal models for force estimation 12

2.4. *In vivo* contact force measurements 13

2.5. Comparison of relevant features of baboons and humans 13

2.6. Intraspecific and interspecific scaling 15

2.6.1. Scaling in biology 15

2.6.2. Scaling in terrestrial support 16

2.6.3. Musculoskeletal scaling of pectoral structures between baboons and humans 18

3. MATERIALS AND METHODS 1

3.1. Measurement systems 18

3.1.1. Normal force measurement 18

3.1.2. Electrical stimulation and in-line force measurement 22

3.2. Preconditioning and calibration 23

3.2.1. Force sensor preconditioning and calibration 23

3.2.2. Accelerometer calibration 26
3.2.3. Buckle strain transducer calibration 26
3.3. *In vivo* loading environment of the instrumented pacemaker in the baboon 26
3.3.1. Experimental design 26
3.3.2. Implantation, post-implant healing and system checks 28
3.3.3. Experiments on conscious baboons 28
3.3.4. Experiments on anaesthetized baboons 29
3.4. Morphometric measurements 32
3.5. Histological analysis 33
3.6. Data Analysis 33
3.6.1. Pre-processing of raw instrumented pacemaker data 33
3.6.2. Conversion of force sensor data from voltage to force 33
3.6.3. Conversion of accelerometer data from voltage to acceleration 34
3.6.4. Conversion of buckle strain transducer from voltage to force 34
3.6.5. Extracting resting sensor voltages 34
3.6.6. Post-processing of force data from force sensors 35
3.7. Interspecific transfer function concept for predicting *in vivo* forces on implanted pacemaker in humans 37
3.7.1. Proposed concept 37
3.7.2. Correlation of experimental parameters 38
4. *IN VIVO* MECHANICAL LOADING CONDITIONS OF INSTRUMENTED PACEMAKER .. 39
4.1. Performance of data acquisition system 39
4.2. Evaluation of the acquired force sensor data 39
4.2.1. Effect of preconditioning and experimental conditions on calibration curves 39
4.2.2. Choice of suitable calibration curves 40
4.2.3. Ranges and observed trends of the force sensor data for evaluating conversion of sensor voltage to sensor force 41
4.3. Healing of implants and histology of device encapsulation 46
4.4. Morphometric measurements 46
4.5. *In vivo* loading during conscious activities of baboons 49
4.6. Range of motion experiments on anaesthetized baboons 52
4.7. Manual external compression experiments on anaesthetized baboons 55
4.8. Electrical stimulation experiments on anaesthetized baboons 58
4.9. Sensor interaction and transient response 60

4.10. Correlation of total force on IPM with morphometric data 62

4.11. Discussion 64

4.11.1. Feasibility of *in vivo* normal force measurement system 64

4.11.2. Evaluation of *in vivo* experimental outcomes 71

5. CONCEPT OF AN INTERSPECIFIC TRANSFER FUNCTION 74

5.1. Correlation of experimental parameters 74

5.2. Formulation of concept 76

5.2.1. Approach 76

5.2.2. Parameters that governed the normal force on the sub-muscular IPM 77

5.2.3. Robustness of the established intraspecific correlation for baboons 82

5.2.4. Assessment of suitability of the intraspecific correlation for humans 82

5.2.5. Final concept 84

5.3. Discussion 86

6. CONCLUSIONS AND RECOMMENDATIONS 89

6.1. Conclusions 89

6.2. Recommendations 90

Improvement of the *in vivo* force measurement system 90

Measurement of *in vivo* mechanical loading on implanted pacemakers 90

Refinement and validation of interspecific transfer function 91

REFERENCES 92

APPENDICES 99

A. Voltage-force conversion method for force sensors 99

A.1. Overview 99

A.2. Custom high-pass filter for obtaining the valid minimum sensor measurement per experiment 100

A.3. Assumptions regarding sensitivity and sensor voltage offset 104

A.4. Adjustment of *in vivo* sensor data for use with post-explant calibration curves 105

A.5. Utilizing resting sensor voltage to accommodate for variation of valid minimum sensor voltage 107

B. *In vivo* morphometric and force measurements 109

C. Results of the strongest intraspecific correlation obtained from linear regression analysis 112

List of abbreviations

ATP	Adenosine triphosphate
ANOVA	Analysis of variance
Chat12	12 mm Chatillon experiments (digital force gauge with 12 mm rigid and flat endplate)
Chat76	76 mm Chatillon experiments (digital force gauge with 76 mm rigid and flat endplate)
El,0° - Abd,0°	Anatomical position
El,-10° - Abd,0°	Elevated at -10°, Abducted at 0° - relative to anatomical position
El,135° - Abd,0°	Elevated at 135°, Abducted at 0° - relative to anatomical position
El,135° - Abd,45°	Elevated at 135°, Abducted at 90° - relative to anatomical position
El,135° - Add,45°	Elevated at 135°, Adducted at 45° - relative to anatomical position
El,45° - Abd,0°	Elevated at 45°, Abducted at 0° - relative to anatomical position
El,45° - Abd,45°	Elevated at 45°, Abducted at 90° - relative to anatomical position
El,45° - Add,45°	Elevated at 45° - Adducted at 45° - relative to anatomical position
El,90° - Abd,0°	Elevated at 90°, Abducted at 0° - relative to anatomical position
El,90° - Abd,90°	Elevated at 90°, Abducted at 90° - relative to anatomical position
El,90° - Add,45°	Elevated at 90°, Adducted at 45° - relative to anatomical position
EMG	Electromyography
eStim	Electrical stimulation
ICD	Implantable cardioverter defibrillator
IPG	Implantable pulse generator
IPM	Instrumented pacemaker
NIH	National Institutes of Health
PCSA	Physiological cross-sectional area
Pec major (sternum)	The portion of the *pectoralis major* muscle that originates from the sternum (and usually overlies the IPM)
RF	Radio Frequency
ROM	Range of motion
SubM	Sub-muscular implant position of an implantable pacemaker
SubQ	Sub-coetaneous implant position of an implantable pacemaker
VHM	Virtual Human Male of the NIH Visible Human Project

List of symbols

A	Surface area of a self-similar object (Chapter 1)
A_D	Area of the principle surface of instrumented pacemaker not covered in sensors
A_N	Area of the principle surface of instrumented pacemaker covered in sensors
A_T	Area of the principle surface
b	Scaling exponent of biological allometric equation
c_a	Axial damping component of the pectoralis major muscle
c_r	Transverse damping component of the ribcage
c_{t1}	Transverse damping component of pectoralis major muscle
c_{t2}	Transverse damping component of pectoralis minor muscle
D_D	Force distribution on principle plane of instrumented pacemaker not covered in sensors
D_S	Force distribution on principle plane of instrumented pacemaker covered in sensors
f_1	Unadjusted raw calibration curve
f_2	Calibration curve adjusted to the origin by offsetting it by the zero-load offset voltage
f_3	Calibration curve adjusted in the direction of the origin by offsetting it by valid minimum sensor voltage
F_{buckle}	Force exerted by the muscle wound through the buckle
F_{chat12}	12 mm Chatillon force data
F_{chat76}	76 mm Chatillon force data
F_{IL}	In-line force developed by the contracting muscle
F_{ILmax}	Maximum in-line force developed by the contracting muscle
F_{ILmean}	Mean in-line force developed by the contracting muscle
F_{ILrest}	Resting in-line force developed by the contracting muscle
$\frac{dF_{IL}}{dw_{m,IPM}}$	Distribution of in-line muscle force throughout the width of the muscle
F_m^0	Maximum isometric force that a muscle can produce
F_N	An arbitrary normal force measured by a force sensor
F_N'	An actual arbitrary force exerted on the force sensor
F_{N0}	Zero-load force (at zero-load offset sensor voltage)
F_{Nerr}	Error between the actual and measured normal force measured by a force sensor

F_{Nrest}	The normal force measured by a sensor when the test subject is at rest
F_{NT}	The total normal force measured on the principle plane of the instrumented pacemaker
F_{NTmax}	The maximum total normal force measured on the principle plane of the instrumented pacemaker
F_{NTmean}	The mean total normal force measured on the principle plane of the instrumented pacemaker
$F_{NTmedian}$	The median total normal force measured on the principle plane of the instrumented pacemaker
F_{NTrest}	The total normal force measured on the principle plane of the instrumented pacemaker when the test subject is at rest
F_{NTstd}	The standard deviation of the total normal force measured on the principle plane of the instrumented pacemaker
F_{Nx}	An arbitrary normal force measured by the force sensor x (for x = 1, 2, 3, 4, 5 or 6)
k_a	Axial elastic component of the pectoralis major muscle
k_r	Transverse stiffness component of the ribcage
k_{t1}	Transverse stiffness component of pectoralis major muscle
k_{t2}	Transverse stiffness component of pectoralis minor muscle
L_m	Muscle fibre length
L_m^0	Optimal muscle fibre length
L_m^{meas}	Measured muscle length
L_r	Characteristic length of the ribcage determined by the rib geometry and curvature responsible for its axial stiffness and damping
M	Body mass
M	Mass of a self-similar object (Chapter 1)
M_m	Mass of the excised *pectoralis major* muscle
*P*0, *P*2.5, *P*50, etc.	0^{th}, 3^{rd}, 50^{th} etc. percentiles
P_{NT}	The total normal pressure measured on the principle plane of the instrumented pacemaker
$P_{NTmedian}$	The median total normal pressure measured on the principle plane of the instrumented pacemaker
P_{NTrest}	The total normal pressure measured on the principle plane of the instrumented pacemaker when the test subject is at rest
r	Linear dimension of self-similar object (Chapter 1)
T_a	Response time period of accelerometers
T_{amb}	Ambient temparature

$t_{m,cb}$	Thickness of the *pectoralis major* muscle at the crossbar of buckle strain transducer
t_{mu}	Thickness of the *pectoralis minor* muscle
V	Volume of a self-similar object (Chapter 1)
V_m	Volume of the excised *pectoralis major* muscle
V_N	An arbitrary sensor voltage of a force sensor
$V_{N(f1)}$	An arbitrary sensor voltage of a force sensor on the unadjusted raw calibration curve
$V_{N(f2)}$	An arbitrary sensor voltage of a force sensor on the calibration curve adjusted to the origin by offsetting it by the zero-load offset voltage
$V_{N(f3)}$	An arbitrary sensor voltage of a force sensor on the curve adjusted in the direction of the origin by offsetting it by valid minimum sensor voltage
ΔV_{Nbr}	The distance of the valid minimum relative to the resting sensor voltage, also referred to as the distance "below rest"
ΔV_{Ncal}	Calibrated voltage range
V_{Nmin}	The minimum sensor voltage of a force sensor
V_{Noff}	Zero-load offset sensor voltage (this parameter is equivalent to the resting sensor voltage of the unloaded sensor)
$V_{Noff(f1)}$	Zero-load offset sensor voltage on the unadjusted raw calibration curve
$V_{Noff(f2)}$	Zero-load offset sensor voltage on the calibration curve adjusted to the origin by offsetting it by the zero-load offset voltage
$V_{Noff(f3)}$	Zero-load offset sensor voltage on the calibration curve adjusted in the direction of the origin by offsetting it by valid minimum sensor voltage
V_{Nperc}	An arbitrary percentile value of a sensor voltage data set
$\frac{\Delta(V_{Nperc})}{\Delta(perc)}$	The slope of the straight line between every pair adjacent of percentiles increments
$V_{Nperc\text{-}P0}$, $V_{Nperc\text{-}P3}$, $V_{Nperc\text{-}P50}$, etc.	0^{th}, 3^{rd}, 50^{th} etc. percentiles values of a sensor voltage data set
V_{Nrest}	The sensor voltage of a force sensor when the test subject is at rest
V_{Nvmin}	The valid minimum sensor voltage of a force sensor, i.e. was not caused by signal noise
$V_{Nvmin(f1)}$	The valid minimum sensor voltage of a force sensor on the unadjusted raw calibration curve
$V_{Nvmin(f2)}$	The valid minimum sensor voltage of a force sensor on the calibration curve adjusted to the origin by offsetting it by the zero-load offset voltage
$V_{Nvmin(f3)}$	The valid minimum sensor voltage of a force sensor on the calibration curve adjusted in the direction of the origin by offsetting it by valid minimum sensor voltage

$V_{Nvmin\ exp,m}^{series,d}$	The valid minimum sensor voltage for a particular experiment (*d*), when considering the data obtained for all experiments within the particular series of experiments (*d*)
V_{Nx}	An arbitrary sensor voltage of the force sensor x (for x = 1, 2, 3, 4, 5 or 6)
$w_{m,cb}$	Width of the *pectoralis major* muscle at the crossbar of the buckle force transducer
$w_{m,IPM}$	Width of the *pectoralis major* muscle where it overlies the instrumented pacemaker
Y	Dependent parameter of biological allometric equation
Y_0, Y_1, Y_2	Normalization constants of biological allometric equations
α	Operator indicating proportionality
θ	angle of pennation (the fibre angle relative to the line of action)
λ	Filter threshold (of the custom high-pass filter)
ρ	Density of a self-similar object (Chapter 1)
ρ_m	Density of the *pectoralis major* muscle
σ_m	Tension in the *pectoralis major* muscle
σ_{mu}	Tension in the *pectoralis minor* muscle
ψ_1, ψ_2	Angles of muscle attachment (angle that muscle attached to its origin and insertion, respectively)
ϕ	Slope threshold between percentile increments of equal size

List of figures

Figure 1: Typical shapes of commercially available pacemakers: a) an implantable pulse generator/pacemaker (IPG) and b) an implantable cardioverter defibrillator (ICD). Pictures courtesy of Medtronic. 5

Figure 2: Pectoral implant positions showing, the typical position of a pectorally implanted pacemaker in the, a) sub-muscular (subM) implant position and the b) sub-coetaneous (subQ) implant position. 6

Figure 3: Levels of organization of skeletal muscle. Adapted from Peterson (2007). 8

Figure 4: Architectural properties of muscle determine the line of action of a muscle 9

Figure 5: Force-length relationship of skeletal muscle as a result of overlapping myosin (thick) and actin (thin) filaments. Three lines indicate the active, passive and total force developed in the muscle. Adapted from Peterson (2007). 11

Figure 6: Example of transducer used for in vivo force measurement. Adapted from Knudson (2007). 12

Figure 7: Hill-type model for contraction dynamics of a muscle. Adapted from Peterson (2007). 12

Figure 8: Musculature of the human chest indicating, specifically indicating the two pectoral muscles, i.e. pectoralis major and pectoralis minor, adapted from Van De Graaf (2002) 15

Figure 9: High-level description of the normal force measurement system. 19

Figure 10: The instrumented pacemaker, indicating the force sensor numbering, the principal surface and the sensor cover plates: a) front view and b) side view. 20

Figure 11: Buckle strain transducer: a) picture and b) schematic illustration of how the muscle was wound through the buckle and how the contracting muscle exerted a force on the buckle. 23

Figure 12: Two calibration curves for the same sensor at sequential time points (>1 hour), displaying sensor drift and change in sensitivity. These changes were reflected by the calibrated voltage range (ΔV_{Ncal}) and the zero-load voltage offset (V_{Noff}), respectively. 24

Figure 13: Instron calibration fixture for instrumented pacemaker (IPM), showing different locating and adjusting settings for preventing any movement of the IPM during calibration procedures. 25

Figure 14: Example of a post-explant calibration curve of a force sensor that was offset to the origin and fitted with a 5^{th} degree polynomial function. 26

Figure 15: The approach to in vivo data acquisition from baboon and timelines from implantation to final data acquisition 27

Figure 16: Pectoral region of Chacma baboon immediately after implantation of the IPMs. The different implant positions (subQ and subM) are indicated. 28

Figure 17: Convention of key upper arm positions used in the ROM experiments, illustrated on an IPM implanted on the right side, showing both anterior and medial veiws of these positions: a) the position of an IPM implanted relative to the arm, b) the different physiological ranges of motion positions of the upper arm and c) definitions of the different upper arm postions. 30

Figure 18: Size and shape comparison of instrumented pacemaker to Chatillon digital force gauge endplate: a) 76 mm endplate and b) 12 mm endplate 31

Figure 19: Representation of experimental setup of anaesthetized eStim monitor sets 31

Figure 20: Experimental setup of the electrical stimulation (eStim) experiments. Beads glued to the surface of the muscle assisted the analysis of dimensional changes due to muscle contraction with a two camera orthogonal setup (not part of this study). 32

Figure 21: The proposed concept of the interspecific transfer function. This concept proposes using of the total force experienced by the IPM (F_{NT}) in baboons (input) to predict the F_{NT} in humans (output). It followed an indirect route involving relating the relevant muscle in-line force (F_{IL}) and morphometric parameters to the F_{NT}, as was measured in baboons. This relationship was then proposed to be suitable for use in humans. 37

Figure 22: All pre-implant and post-explant calibration curves for two selected sensors illustrating, a) the comparable calibration curves for both pre-implant and post-explant (sensors of SN068 and SN069) b) comparable calibration curves for pre-implant and post-explant respectively, but not between pre-implant and post-explant calibration curves (sensors of SN074 and SN076). 40

Figure 23: The most suited post-explant calibration curves chosen for each sensor of these four IPMs, i.e. SN068, SN069, SN076 and SN074, showing the sensor specificity of the calibration curves. 41

Figure 24: Box plots of selected sensors showing the typical force sensor voltage (V_N) ranges acquired from the most suited post-explant calibration curves (PE ΔV_{Ncal}) and different series of in vivo experiments. The box plots indicate percentile values of sensor data combined for a complete series of experiments. The resting voltage indicated (V_{Nrest}) was averaged per series of experiments. No eStim experiments were performed for SN074 and SN076 (Section 4.8). 42

Figure 25: Change in calibrated voltage range (ΔV_{Ncal}) of each sensor during subsequent post-explant calibrations, normalized to the first calibration event. Examples are shown of sensors assembled on the IPM according to different methods a) SN069 (standard sensor assembly) and b) SN076 (non-standard sensor assembly). 43

Figure 26: Typical examples of the mean and standard deviation of the resting sensor voltage (V_{Nrest}) and the valid minimum sensor voltage (V_{Nvmin}) for a sensor over all the in vivo experiments, showing a) & b) the V_{Nrest} and V_{Nvmin} per series of experiment for sensor 5 of SN068 and sensor 4 of SN076; and c) & d) the normalized V_{Nrest} for each series of experiment, as well as for each "state" of the muscle. It can be seen that the muscle of the anaesthetized baboon is the same for ROM, chat76 and chat12 experiments. All series of experiments displayed in the time order in which it occurred. Error bars not visible were too small to show up on this graph. Normalization to the mean value obtained from the experiments on conscious baboons. No eStim experiments performed for SN076 (and SN074). 45

Figure 27: Cross sectional views of the pectoral region of the baboon and human (Virtual Human Male data set - (Spitzer et al. 1996)), showing the axial section at the middle of the sternum, indicating anterior-posterior (front-to-back) and lateral (femur-to-femur) distances of a) baboon and b) human. The corresponding sagittal section at medial third of the clavicle is also shown for c) baboon and d) human. Note that axial distances between humans and baboons were not according to same scale, however only the ratio of measurements were needed. The position of the non-functional IPM implanted for imaging purposes is indicated with the white arrows. Although the

human data did not include an implanted pacemaker, the location of one was estimated and indicated accordingly..... 48

Figure 28: Position of IPM relative to surrounding skeletal structures for the baboon, indicated by a black arrow. Different views are presented and included a) an isometric view, b) a frontal view and c) a top view. Imaging artefacts present in the CT data were responsible for the bad resolution of the IPM compared to the skeletal structures. 49

Figure 29: A typical example of the total normal force (F_{NT}) over time plot from the experiments on conscious baboons. This plot shows both the individual force sensor measurements (F_{Nx}) and the total force exerted on the IPM (F_{NT}). 49

Figure 30: Histograms of the total normal force (F_{NT}) data points measured by IPMs during the experiments on conscious baboons, with normalized number of observations shown in a logarithmic scale. Data is shown for a) SN068 (subM), b) SN069 (subM), c) SN076 (subM) and d) SN074 (subQ). The maximum total normal force (F_{NTmax}) shown for each IPM was confirmed by synchronous video recordings. 50

Figure 31: Box plot comparing all F_{NT} data points amongst different IPMs (with n > 720 000 for each IPM) 51

Figure 32: The peak force (F_{NT}) relative to the resting force (F_{NTrest}) of physical actions associated with the 30 maximum force peaks measured during experiments on conscious baboons. Certain movements in certain of the baboons did not yield F_{NT} peaks which fell into the top 30 peaks, which is clear from the data shown. 52

Figure 33: A typical example of the total normal force (F_{NT}) versus time plot from the force measurement ROM experiments, showing the extracted peaks of F_{NT} data. This figure shows the peaks classified for the adduction and abduction (circles), elevation and lowering (triangles) and circumduction (diamonds) movements..... 53

Figure 34: Total normal force (F_{NT}) produced by different positions of the upper arm during force measurement ROM experiments showing a) the identified positions of the upper arm for the anterior and medial views (A-J), b) the extracted peak total normal forces (Peak F_{NT}) (mean ± std) and c) the normalized peak force (F_{NT}) relative to the resting force (F_{NTrest}) (mean ± std)..... 53

Figure 35: Different positions of the IPM relative to surrounding musculoskeletal structures during adduction as observed in the fluoroscopy ROM experiments. These images show anterior-posterior fluoroscopy taken of the chest of baboon #575. The position of the femur and the considered IPM are shown for a) & b) adduction causing “sandwich” compressive force on (subM – black arrow) IPM, c) the baboon at rest and d) & e) adduction causing “rolled out” compressive force on (subQ – white arrow) IPM. 55

Figure 36: Typical examples of manual external compression experiments (76 mm Chatillon and 12 mm Chatillon) showing: a) the force applied by the Chatillon digital force gauge with a 76 mm endplate (F_{chat76}) and the measured total normal force (ΔF_{NT}) plotted against time; and b) the force applied by the Chatillon digital force gauge with a 12 mm endplate (Fchat12) and the measured sensor normal force (ΔF_{Nx}) plotted against time. Both these graphs show peaks extracted from the Chatillon force data and corresponding IPM data. 56

Figure 37: Box plots showing the ratio of the change of total normal force measured by the IPM (ΔF_{NT}) and the force applied by the Chatillon with the 76 mm endplate (F_{chat76}) for each IPM. Each

data point used for these box plots was the ratio between corresponding ΔF_{NT} and F_{chat76} extracted during the 76 mm Chatillon experiments. 57

Figure 38: Box plots showing the ratio of the change of total normal force measured by the IPM (ΔF_{NT}) and the force applied by the Chatillon with the 12 mm endplate (F_{chat12}) for each IPM. Each data point used for these box plots was the ratio between corresponding ΔF_{NT} and F_{chat12} extracted during the 12 mm Chatillon experiments. No sufficient extractable data was available for certain sensors and hence the corresponding box plots were omitted. Data from s3 of SN074 yielded negative values over a wide range – only the upper range fell within the specified scale. 58

Figure 39: A typical example of a response from an electrically stimulated muscle, showing the peaks extracted from the in-line muscle force (F_{IL}) and total force on the IPM (F_{NT}) data. 59

Figure 40: The in-line muscle force (F_{IL}) produced by corresponding eStim current amplitude, in the order as they occurred experimentally, showing results of: a) SN068 (chronic implant), b) SN069 (chronic implant), c) SN066.1 (acute implant) and d) SN066.2 (acute implant). The scattered data points indicate maximum F_{IL} developed for the corresponding discrete eStim amplitude levels, indicated by the solid line. 59

Figure 41: Force responses of in-line muscle force (F_{IL}) and corresponding total force on the IPM (F_{NT}), caused by electrical stimulation of the pec major (sternum) muscle overlying the IPM. Simple linear regression yielded the trendlines plotted for each IPM. 60

Figure 42: Examples of sensor interaction and transient response showing, a) chat12 experiments: sensor voltage (V_N) response of sensors 5 and 6 showing simultaneous measurement of force (A) and sensor interaction (C) respectively and b) post-explant calibration event: sensor voltage (V_N) response of all sensors clearly showing the sensor being calibrated and the measurements induced by sensor interaction. The transient response of sensor voltage was also clearly observed when the calibration load was released. c) Diagram indicating location of the sensors on the IPM. 61

Figure 43: The total resting force (F_{NTrest}) measured by the IPMs for different series of experiments, although the "state" of the pectoralis major muscle for each series was the same, i.e. anaesthetized muscle. The asterisk (*) indicates the F_{NTrest} for the chat12 experiments of SN074 was 514.11 N, but for reasons of scale, the y-axis was limited. 69

Figure 44: The total resting force (F_{Nrest}) measured by the IPMs for all series of experiments, except for the manual external compression experiments (chat76 and chat12). These results corresponded with the "state" of the muscle for each series of experiments, i.e. muscle of conscious baboon, muscle of anaesthetized baboon and exposed muscle. No eStim data were obtained from SN076 and SN074. The acute IPM used (SN068) in both animals yielded comparable results to the chronic IPMs (SN068 and SN069). 70

Figure 45: Predicted vs. observed values for the total force exerted on the IPM (F_{NT}) in the baboon. The predicted results were obtained from the intraspecific correlation equation that was established. The dashed line shows the 95% confidence interval. 75

Figure 46: The total force (F_{NT}) experienced by the subM implanted IPM and the factors that influenced its magnitude showing, a) a simplified representation and b) an equivalent mechanical model displaying the model parameters. 78

Figure 47: Concept of the interspecific transfer function used to relate the total force experienced by a subM IPM in vivo (F_{NT}) in baboons to the F_{NT} in humans. This concept utilized the influence of the

in-line muscle force (F_{IL}) and morphometric parameters on F_{NT} in baboons, to find a similar relationship in humans and thereby yielding the F_{NT} in humans. 85

Figure 48: Sensor voltage (V_N) data from of a typical experiment indicating, a) the V_N data sorted in an ascending order, b) a zoomed view of the V_N data sorted in an ascending order, indicating the 0^{th} to the 3^{rd} percentile in 0.25 percentile increments, c) a histogram of the V_N data points and d) a zoomed view of the histogram of the V_N data points, indicating the 0^{th} to the 3^{rd} percentile in 0.25 percentile increments..... 101

Figure 49: Lower percentiles of a single sensor over a whole series of experiments. The percentile values are indicated in 0.25 percentile increments. 102

Figure 50: Lower range percentiles of sensor voltages against percentile increments for a typical experiment, with data points between each percentile increment being equal. The 0^{th}-percentile to 3^{rd}-percentile are shown, as well as the identified valid minimum sensor voltage for the monitor event..... 103

Figure 51: Adjusting an arbitrary in vivo sensor voltage data point (V_N) to obtain its corresponding approximated sensor force data point (F_N). For purposes of illustration, the scale of this figure is exaggerated. 105

Figure 52: Demonstrating the method for utilizing the maximum distance from the valid minimum sensor voltage (V_{Nvmin}) relative to the resting sensor voltage (V_{Nrest}) for comparable force estimations (F_N) between experiments in the same series. The “below rest” interval (ΔV_{Nbr}) for each experiment is shown, from which the largest interval was chosen to calculate V_{Nvmin} for each, and offset to obtain $f_3 = f_{3p} = f_{3q}$..... 108

Figure 53: A histogram showing the distribution of residuals obtained from the multiple linear regression analysis performed for case C of Table 7. The smooth line shows the expected normal. 113

Figure 54: Normal probability plot of the residuals which shows the expected normal values against the corresponding residual values, obtained from the multiple linear regression analysis performed for case C of Table 7. 114

Figure 55: Observed values of F_{NT} against the corresponding residuals, obtained from the multiple linear regression analysis performed for case C of Table 7. 112

List of tables

Table 1: Emperical and theoretical scaling patterns of bone and muscle stress in terrestrial animals, adapted from (Biewener 2000). Theoretical scaling relationship for bone and muscle are the same, since scaling relationship is derived from groups of samples (e.g. bone or muscle) having the same density, respectively. 17

Table 2: Geometric information of the instrumented pacemaker 19

Table 3: Performance characteristics of the FlexiForce contact force sensors, as reported by its manufacturer (Tekscan 2005). 20

Table 4: Normalized values of the resting sensor voltage (V_{Nrest}) (mean ± std) of all 6 sensors per IPM, for different "states" of the muscle overlying the IPM (pectoralis major). No eStim experiments performed for SN076 (and SN074). 46

Table 5: Morphometric measurements of test subjects are shown, together with relevant implant and explant information. Muscle parameters presented are for the pectoralis major muscle specifically. 47

Table 6: The type of sensor interaction caused by sensor calibration events (compression of a single sensor), indicating direct interaction (+), inverse interaction (-) and no interaction (0) 62

Table 7: Linear regression analyses results between different combinations of experimentally measured parameters. 74

Table 8: Model parameters that influenced the total normal force on the IPM (F_{NT}) were affected by the indicated morphometric parameters. The availability of morphometric data for baboons and humans are shown. In addition, the intraspecific and interspecific relative difference of the morphometric parameters is proposed. Finally, the intraspecific and interspecific influence of these morphometric parameters on F_{NT} is proposed. 80

Table 9: An assessment to determine the robustness of the intraspecific correlation established in baboons. This was done by investigating whether intraspecific linear relationships between the identified morphometric parameters and associated model parameters existed. This assessment was performed one parameter at a time, assuming all other parameters, of an equivalent experimental setup, remained constant. 82

Table 10: An assessment to determine the suitability of using the intraspecific correlation established in baboons for humans. This was done by investigating whether interspecific linear relationships between morphometric and associated model parameters existed. This assessment was performed one parameter at a time, assuming all other parameters, of an equivalent experimental setup, remained constant. 83

Table 11: In vivo morphometric measurements and force results from experiments on conscious baboons, range of motion, 76 mm Chatillon and eStim experiments. 109

Table 12: In vivo force measurement of 12 mm Chatillon experiments 110

Table 13: Resting force measured by individual sensors (F_{Nrest}) and calculated total resting force on the principle surface of IPM (F_{NTrest}). All forces are in Newtons. 111

Table 14: Summary of multiple linear regression analysis performed for case C of Table 7 112

Table 15: Analysis of variance (ANOVA) of the multiple linear regression analysis performed for case C of Table 7. 112

Table 16: Correlations of the regression coefficients of the multiple linear regression analysis performed for case C of Table 7. 113

1. Introduction

1.1.Background and motivation

Implantable cardiac pacemaker devices (or just: pacemakers) are complex devices for artificially managing cardiac arrhythmias in patients. These devices have been "proven to reduce mortality in specific high-risk patient populations" (Maisel et al. 2006) and provide significantly increased benefits (clinical and financial) compared to purely pharmacological treatment of patients with cardiac arrhythmias (Cleland et al. 2005). Pacemakers fall into two main categories, which are implantable pulse generators (IPG) and implantable cardioverter defibrillators (ICD).

In recent years several emerging factors have increased the mechanical demands placed on implanted pacemakers. These include major technological advances in pacemaker design and function, making it possible to reduce the size of pacemakers (especially its thickness) (Furman 2002; Maisel et al. 2006; Shmulewitz et al. 2006). In addition, these technological advances, coupled with clinical advances, have also made the use of pacemakers in younger patient populations more feasible (Friedman 1992; Furman 2002; Antretter et al. 2003). Younger populations of patients are also relatively more active than patients traditionally receiving pacemakers. The increased mechanical demands impose an increased demand on the structural integrity and mechanical longevity of the devices. These demands have to be addressed in the device development stage through tailored structural design.

Increased mechanical loading on pacemakers may have a detrimental effect on the reliability of the device. While the device reliability remains uncertain and difficult to quantify (Maisel et al. 2006), the most important (yet elusive) measure of reliability is a malfunction of the system, because no single measure accurately reflects all complexities in a verifiable fashion (Wilkoff 2006). Nevertheless, high levels of reliability for pacemakers are crucial, since device malfunction has various clinical and financial implications for recipient health, care provider and device manufacturers (Maisel et al. 2001; Maisel et al. 2006). Even if device malfunction does not occur, reduced reliability of pacemakers can lead to advisories by manufacturers on potential device failure. Although not as severe as device malfunctions, advisories by manufacturers also have detrimental consequences (Llewellyn et al. 1989). The importance of high device reliability is further emphasized by the increased prevalence of pacemaker usage (Maisel et al. 2001) and by a recent study showing that patients preferred device longevity over a decreased pacemaker size (Wild et al. 2004).

Nevertheless, pacemakers (i.e. IPGs and ICDs) deliver "dramatic life-sustaining and life-saving effectiveness" despite all of the abovementioned complexities (Wilkoff 2006), and a suspected influence on the device reliability therefore justifies and necessitates further investigation.

Currently, very little information is available regarding the *in vivo* mechanical loading conditions (magnitude and cycles) experienced by implanted pacemakers. Studies aimed at characterizing these loading conditions mainly involved tests on human cadavers by research collaborators (unpublished data). Cadaver tests rely on, and are limited to, passive movements of the upper extremities. The limitations of these studies are mainly that true *in vivo* loading conditions are not reached, due to various factors. These factors include, amongst others, differences in tissue properties, no conscious

muscle tone, no breathing loads and no dynamic changes within the implant site during healing. These physiological differences may be less limiting in certain situations, e.g. for the testing of mechanical loadings on the implanted device in a simulated vehicle crash (where inertia forces are likely to dominate considerably due to the deceleration upon impact). However, these differences put into question the validity of the data for other situations such as day-to-day activities of the recipient. To the author's knowledge, no data have been published specifically on the *in vivo* loading conditions of the structure of an implanted pacemaker device.

An additional unknown factor to the mechanical loading conditions of an implanted pacemaker was whether a pacemaker is subjected to a different loading severity during normal physiological conditions, based on its implanted position. Of particular interest is the difference in loading experienced by the two most common implant positions, i.e. the sub-muscular and sub-coetaneous implant positions in the pectoral region.

Research collaborators (CRDM, Medtronic Inc., Minneapolis, USA) undertook a project to define the actual mechanical use condition stresses vs. product survival capability strengths, in order to provide design margin information and design input to produce products of higher quality and improved reliability.

In the first phase of reaching this objective, research collaborators developed a system that enabled investigation into the *in vivo* mechanical loading conditions on implanted pacemakers. This system utilized technology that can facilitate the synchronization of video footage with high bandwidth, wirelessly acquired force and acceleration data. This data conveyed valuable information about the loading conditions on these devices associated with a multitude of activity events when implanted. Advances in miniaturized technologies have enabled the development of this type of system, which have proved to be of great importance in the development of, amongst others, the medical device industry (Shmulewitz et al. 2006). The system was developed to a level where it could be tested in pre-clinical animal studies, as reported here. For the animal-to-human transfer function, the study incorporated the investigation of a relationship between the in-line force and corresponding normal force of the *pectoralis major* muscle, proposed by Micah Litow (Neurological Division, Medtronic Inc.).

The Cardiovascular Research Unit at the University of Cape Town and research collaborators had jointly undertaken the first phase of this project, which was concerned with: (1) the evaluation of the feasibility of using data obtained from this baboon model to predict *in vivo* loading conditions of implanted pacemaker in humans and (2) the acquisition and comparison of *in vivo* mechanical loading data of pacemakers implanted in sub-coetaneous and sub-muscular positions in the pectoral region of non-human primates (Chacma baboons).

1.2. Objectives

This MSc project was a feasibility study that formed part of the abovementioned project, with the following objectives:

- Evaluate feasibility of the system, developed by research collaborators, for measuring *in vivo* mechanical loading conditions on an implanted pacemaker in baboons;
- In baboons, evaluate the *in vivo* mechanical loading conditions of pacemakers implanted pectorally in the sub-muscular and sub-coetaneous implant positions, respectively;
- Propose a concept of an interspecific transfer function to predict the *in vivo* mechanical loading on pectorally implanted pacemaker in humans using the loading acquired in the baboons.

This report starts with a review of literature and theory relevant to this project. In Chapter 3, the system for measuring *in vivo* forces on an implanted pacemaker, the system for measuring in-line muscle force and measurements of relevant baboon morphology are described, along with the data analysis performed. The *in vivo* pacemaker mechanical loading (force), in-line muscle force and morphometric measurement results obtained for evaluating system feasibility and *in vivo* loading conditions of a pacemaker in baboons are reported in Chapter 4. These *in vivo* results are also discussed in the same chapter. Chapter 5 reports correlations performed that were required for the formulation of the concept for the interspecific transfer function, the formulation itself and its subsequent discussion. Finally, conclusions are drawn from the discussed findings and recommendations for further research are presented in Chapter 6.

2. Literature review and theory

2.1. Implantable cardiac pacemaker devices

2.1.1. Description, function and extent of use

As mentioned previously, implantable cardiac pacemaker devices are complex devices for artificially managing cardiac arrhythmias in patients. These devices fall into two main categories; namely implantable pulse generators (IPG) and implantable cardioverter defibrillators (ICD). The current leading IPG and ICD that are being used, typically operate as follows: an electrical impulse(s) is generated due to sensorial feedback, which is (are) delivered by means of a transvenous lead(s) connected to the heart muscle itself. Feedback is received from sensors on the lead(s) that ultimately enables the regulation of the heartbeat. The electrical impulses are controlled by firmware controls (integral device software) and are optimally adjusted according to the individual patient's pacing needs and feedback received from lead sensors (Jeffrey et al. 1998).

The original function of IPGs was to treat cardiac arrhythmias (i.e. bradycardia and tachycardia), while ICDs were used to terminate severe abnormal cardiac rhythms (e.g. atrial and ventricular fibrillation). However, recent technological advances in pacemaker and lead technology have stimulated the design and production of hybrid devices combining functionalities, according to the patient-specific pacing requirements (Jeffrey et al. 1998; Cannom et al. 2004).

A study based on reports submitted to the Food- and Drug Administration (FDA) by manufacturers, presented data on the extent of use of these devices. The study showed that over 2.5 million IPGs and ICDs were implanted from 1990-2002 in the United States, while the annual number of IPGs implanted increased 3-fold over this period (Maisel et al. 2006).

2.1.2. System designs

Current leading pacemakers consist of dedicated programmable hardware, firmware controls (integral device software), an on-board battery, hermetically sealed housing and lead-specific connectors. Although pacing equipment started out as large external "appliances" during its development in the 1950's and 1960's, all devices are currently of a general shape as shown in Figure 1. The volume of currently used ICDs has dramatically decreased from the first implantable devices in the mid-1990's (currently ≅40 cm^3), while IPGs are much smaller (≅15 cm^3) (Costeas et al. 2000). The housing structure is made of a metallic body and a non-conducting head (for insertion of stimulation leads) that adhere to biocompatibility, strength and conductivity requirements, which are all hermetically sealed (Maisel et al. 2006).

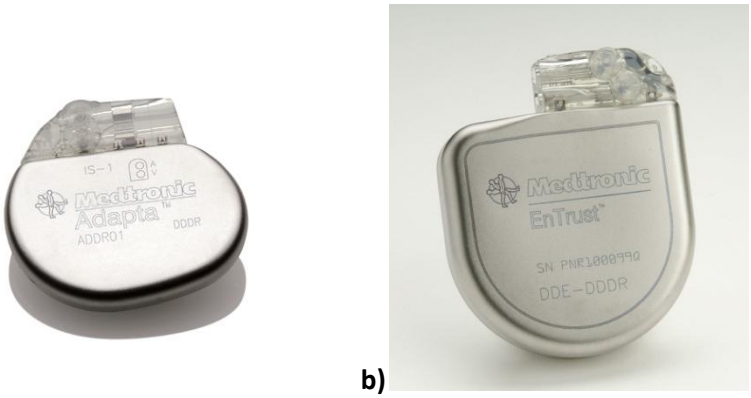

a) **b)**

Figure 1: Typical shapes of commercially available pacemakers: a) an implantable pulse generator/pacemaker (IPG) and b) an implantable cardioverter defibrillator (ICD). Pictures courtesy of Medtronic.

A pacing lead connects to the pacemaker on one side and to the heart muscle on the other side. Variations in lead design (according to the application) include variations on the type of lead that is used (e.g. composition, shape, electrode configuration, method of fixation, and various other special features) and the position that these leads will be attached to the heart muscle (e.g. ventricular or atrial position) (Brinker et al. 2005).

The firmware control of pacemakers is programmable to the patient's specific pacing needs. Patient management software enables physicians to access and organise the pacemaker history data, enables caregivers to remotely update pacemaker performance to clinical information systems and also enable nationwide monitoring of recipient patients conditions to help improve overall care of current and future recipient patients (Maisel et al. 2006).

The selection of a specific pacemaker, leads and supporting software that the patient requires, follows after a thorough assessment of an individual patient. A pacemaker is chosen according to available resources, the patient's pacing needs and physical condition (Brinker et al. 2005).

2.2. Implantation of pacemakers

Current commercially available pacemakers (IPGs and ICDs) are relatively small, which makes pacemaker surgery a minimally invasive procedure that is routinely performed (Kenny 2005).

The implantation procedure is governed by the type of device and leads that are chosen according to the patient's needs, as well as the physical condition of the patient in terms of suitable venous access, suitable implantation pocket conditions, dominant side of patient, etc. The suitable site for venous access to the right atrium (e.g. subclavian, axillary or cephalic veins) determines the appropriate site for the implantation pocket. After a suitable site has been decided on, safe venous lead access must first be identified, after which a pocket must be created for the pacemaker (the location of the pocket being the implant position). Thereafter, the lead must be introduced into the heart muscle, connected to the pacemaker, the pacemaker and redundant lead inserted in the pocket, and the pocket closed (Brinker et al. 2005).

Implantation sites include the abdominal, retromammary and pectoral regions. The abdominal region is mostly used when the physical conditions of the pectoral region are inappropriate for implantation. The retromammary position (in women) is preferred, mainly for cosmetic considerations (Kenny 2005). Pectorally implant positions have been shown to cause fewer

complications as opposed to abdominal implant positions (Kron et al. 2001) and are consequently the more frequently utilized implant sites.

The outside of the pacemaker housing is covered with a biocompatible material which, depending on implant position, can cause full/partial encapsulation of a device by a fibrotic capsule due the body's normal immune response to a foreign body (Ratner et al. 2004).

Complications associated with implantation pockets include skin erosion/necrosis, pocket haematoma, seroma, wound infection, dehiscence, device migration, lead fracture and dislodgment (Gold et al. 1996). The size of the implantation pocket also plays an important role, since too small a pocket may result in severely increased tension exerted on the overlying tissue, while too large a pocket may lead to Twiddler's syndrome, future migration or flipping of the device (Brinker et al. 2005). Furthermore, if the pocket is made too superficial in the layer of skin, it may lead to a pain syndrome requiring re-operation (Furman 2002). Due to the sizable implications on finances and patient health when implanting and maintaining pacemakers systems (Maisel et al. 2001), complications need to be minimized.

Two of the more common pectoral implantation sites used is the sub-muscular (subM) and the sub-coetaneous (subQ) implant positions. A subM pacemaker is implanted beneath the *pectoralis major* muscle and on top of the ribcage (partly on the *pectoralis minor*, subject-dependent), while a subQ pacemaker is implanted sub-coetaneously on the fascia of the *pectoralis major* muscle, as illustrated in Figure 2. Variations on the incisions used to make a pocket for the subM pacemaker have been reported, but ultimately the pacemaker is located beneath the *pectoralis major* (Costeas et al. 2000).

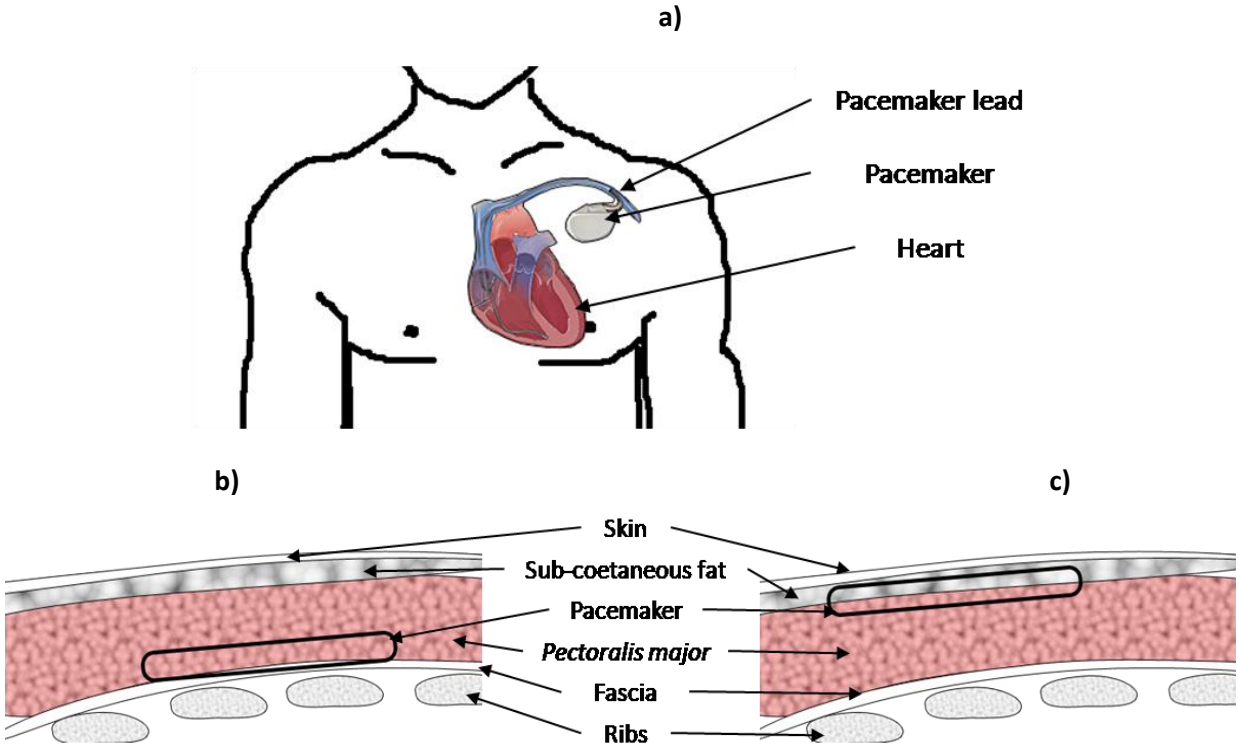

Figure 2: Pectoral implant positions showing, the typical position of a pectorally implanted pacemaker in the, a) sub-muscular (subM) implant position and the b) sub-coetaneous (subQ) implant position.

Various advantages and disadvantages of subM and subQ implant positions have been reported that indicate different viewpoints on the most suited implant position (Gold et al. 1996; Costeas et al. 2000; Furman et al. 2001). The advantages of the subQ implant position include simple surgical procedures, shorter procedural times and overall complication rates that are comparable to subM implants (Gold et al. 1996). The same authors suggest, however, that the subM position is better suited than the subQ position for a number of reasons. These include the reduction of skin necrosis observed at the pacemaker edges, pain caused by incorrectly implanted subQ pacemakers and increased psychological well-being of recipients and their families because of a less protrusive implant. Certain adverse health conditions regarding pectoral regions dictate that the subM position be used, e.g. sparse sub-coetaneous tissue, size of device to be implanted, impending skin erosion from a previous device, concerns about cosmetic appearances, etc. (Brinker et al. 2005).

Recently, a third pectoral implant position was also described, namely the intra-muscular position (between the heads of the *pectoralis major* muscle) (Kistler et al. 2004). It has started to gain popularity over the traditionally used subQ implantations for various reasons, including an improved cosmetic result, the potential advantage of less erosion of overlying tissue and comparable procedural difficulty and time.

2.3. Skeletal muscle

Although skeletal muscle function, morphology, physiology, activation and force generating properties have been extensively described in literature, aspects applicable to this study are briefly discussed below. Sections 2.3.1, 2.3.2 and 2.3.3 were adapted from Sherwood (2004) and Peterson (2007), unless otherwise indicated.

2.3.1. Function, form and physiology

All living cells possess some sort of ability to move and redistribute intracellular components, although the moving specialists by far are muscle cells. Three types of muscle cells occur in humans and animals, namely skeletal, smooth and cardiac muscle. Skeletal muscles exert force not only for the translation of joints, but also to maintain resting posture (resting conscious tone) and joint stability.

Considering only skeletal muscle (henceforth: muscle), the basic building block of a muscle is the muscle cell, also known as muscle fibre, which extends along the entire length of muscle. These fibres are striated by a highly organized internal arrangement called myofibrils. Each myofibril is a specialized contractile element of regular arrangement that consists of highly organized cytoskeletal elements, i.e. thick filaments (assemblies of the myosin protein) and thin filaments (assemblies of three proteins: actin, tropomyosin and troponin). Together these two filaments form the sarcomere – the smallest functional unit of the muscle. These levels of muscle structure are shown in Figure 3.

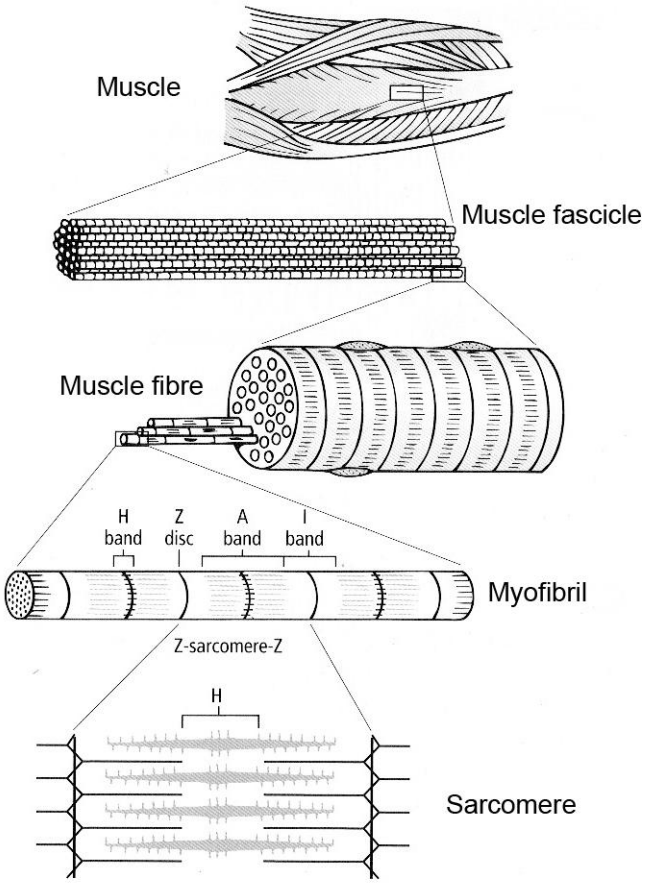

Figure 3: Levels of organization of skeletal muscle. Adapted from Peterson (2007).

Three types of skeletal muscle fibres exist and are classified based on their metabolic capabilities, i.e. the ability to hydrolyse and synthesize adenosine triphosphate (ATP) required for energy. These include slow-oxidative (type I) fibres, fast-oxidative (type IIa) fibres and fast-glycolytic (type IIb) fibres. As the names also imply, the different fibres mainly affect the velocity of fibre contraction and the type of enzymatic machinery used for ATP formation. All skeletal muscle contain different amounts of all these fibres, which are determined by the muscle function.

A muscle contracts (and therefore exerts force) when an electrical impulse of sufficient magnitude activates the muscle. This electrical impulse acts as input stimulus that initiates a chain reaction of chemical processes, collectively referred to as an action potential. The action potential causes opposing filaments (thick and thin) to connect (known as cross bridges), after which the thin element slides inward relative to the stationary thick element and finally the opposing filaments release. This process by which force is produced is known as the sliding filament mechanism of muscle contraction. One such iteration caused by an action potential is defined as a muscle twitch.

The force that a whole muscle exerts depends on how these contracting fibres are arranged in terms of the muscle line-of-action (or force-generating axis), as shown in Figure 4. Different arrangements of muscle fibres naturally occur and are referred to as the muscle architecture. The muscle architecture is described by the angle of pennation (the fibre angle relative to the line of action – θ) and the muscle fibre length (L_m), also shown in this figure.

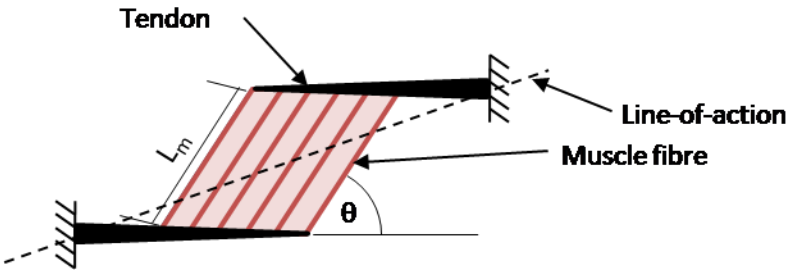

Figure 4: Architectural properties of muscle determine the line of action of a muscle

A sheath of connective tissue covers each muscle fibre, which then joins in bundles or groups of muscle fibres. The connective tissue also extends beyond the ends of the muscle to form a tendon. These tendons consist of tough connective tissue that attaches the muscle to the bone. They act as the pathway through which muscle force is transmitted to bone.

All of the abovementioned structures are responsible for distinct, passive material properties of muscle. Muscle exhibits an onset of passive resistance when stretched beyond the optimal muscle fibre length (L_m^0) (see Section 2.3.3 below) and also a viscoelastic response to compressive forces, which is influenced by the muscle fibre orientation relative to the applied force (Van Loocke et al. 2008). Although muscle density measurement has been shown to depend on the fixation method of the muscle, a value of 1.0597 g/cm^3 has been established as the density for all mammalian skeletal muscle tissue (Ward et al. 2005).

2.3.2. Activation of muscle

A single input stimulus (or action potential) of a muscle fibre is responsible for a muscle twitch. Muscle fibres exhibit a unique property of being able to exert an increased strength of contraction upon receiving repetitive stimulation. Whereas a single action potential will be responsible for a contraction force of the muscle fibre at a certain magnitude, a second action potential occurring before the fibre has had the chance to completely recover, will have a cumulative effect in the magnitude of contraction force, i.e. summation of twitches. If a muscle fibre is stimulated so rapidly that it does not have any chance to recover between stimuli, a certain maximal sustained contraction occurs, known as tetanus.

A muscle can either be activated physiologically via the central nervous system, or artificially by an exogenous electrical signal (electrical stimulation). This input stimulus stimulates a number of different motor neurons leading to the muscle fibres. As a single motor neuron enters a muscle, the axon of the neuron branches out to individually innervate a number of muscle fibres. Each muscle fibre is only innervated by a single motor neuron. When this motor neuron is activated, all muscle fibres it supplies are stimulated to contract simultaneously. This single motor neuron and all its fibres that activate simultaneously is referred to as a motor unit. A whole muscle contains many motor units with fibres evenly distributed throughout the muscle. The more motor units stimulated, or recruited, the stronger the contraction of the muscle will be, i.e. gradation of muscle contraction. The magnitude of strength by which a muscle contracts, depends in part on the size of the motor unit, i.e. the number of fibres innervated per motor neuron. This number varies widely throughout the body and is determined by the function of the muscle.

Maximum voluntary contraction refers to the maximal state of tetanic muscle contraction at which a contraction can be sustained, which is never 100% of all motor units within a muscle.

In order to prevent or reduce muscle fatigue from occurring during sustained contractions, physiological activation of muscle by the central nervous system occurs asynchronously. This means that the body alternates the activation of motor units to allow for recovery time for the muscle fibres of these motor units. Studies in electrical stimulation of muscle have attempted to simulate this action of the central nervous system. Traditionally, this was done by using stimulus signals consisting of short trains of electrical input at constant time intervals (constant frequency trains - CFT). Later, variable time intervals (variable frequency trains - VFT) were used in an attempt to minimize muscle fatigue associated with electrical stimulation (Binder-Macleod et al. 1998). These methods, however, cannot compete with the central nervous system's ability to minimize muscle fatigue. The main reason for this is that physiological muscle activation adapts to fatiguing conditions by recruiting different motor units, as well as changing firing rates (Bobet et al. 1998).

2.3.3. Force generating properties

The factors that influence the magnitude of force produced by a whole muscle are,

- Number of fibres contracting;
- Tension developed by each contracting fibre;
- Angle of pennation (Figure 4).

Despite the unknown interaction complexity of these factors, it is clear that they do not function independently from each other (Huijing 1995; Van den Bogert et al. 1998). These factors are briefly discussed below.

The total number of fibres that contract during muscle contraction is determined by the number of motor units recruited, the number of muscle fibres in each motor unit and the number of muscle fibres available to contract (e.g. number of fibres in a whole muscle, presence of disease, etc.).

The tension developed by each contracting fibre is influenced by a number of factors. These include the frequency of stimulation (twitch summation and tetanus, described in the preceding section), the extent of fatigue (duration of activity, physiological or exogenous stimulation, fibre-type), muscle fibre length at the onset of contraction (force-length relationship) and thickness of muscle fibres. A relationship exists between the muscle fibre length at the onset of contraction and the maximal tetanic force that a muscle can exert at that length. This relationship is illustrated in Figure 5 and has been defined in terms of the optimal muscle fibre length (L_m^0), i.e. the length at which the muscle can generate maximum force. This relationship exists due to the relative position between the thin and thick elements of the muscle (Section 2.3.1), which determine the magnitude of contraction force that a muscle fibre can develop. When muscle fibre length (L_m) is greater than approximately 1.1 L_m^0, muscle starts to exhibit a passive resistance against being stretched, as also shown in this figure.

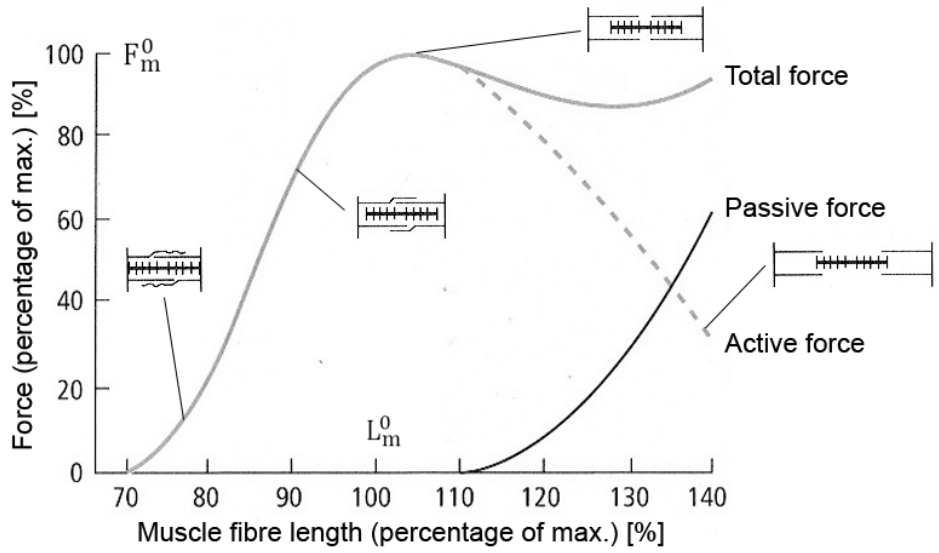

Figure 5: Force-length relationship of skeletal muscle as a result of overlapping myosin (thick) and actin (thin) filaments. Three lines indicate the active, passive and total force developed in the muscle. Adapted from Peterson (2007).

Although the measurement of the thickness of each muscle fibre is unpractical due to its microscopic size, it is represented by the well defined parameter of the physiological cross-sectional area of the muscle (PCSA) (Powell et al. 1984). In a certain sense, the PCSA is the accumulation of the muscle fibre thickness. It also accommodates for the angle of pennation and has been defined as,

$$PCSA = \frac{M_m \cos\theta}{\rho_m L_m^0} \quad (1)$$

In this equation, M_m is the muscle mass, θ the angle of pennation, ρ_m is the muscle density, and L_m^0 the optimal muscle fibre length. The PCSA is directly related to the maximum isometric force that a muscle can produce at its optimal fibre length (F_m^0) (Biewener 2000).

2.3.4. Measurement of force developed in muscle

Physical measurement of force is mainly restricted to research laboratories performing animal experiments, since measurement in humans was restricted to minimally invasive measurement in superficial tendons (Finni et al. 1998), or measurement during surgical procedures (Dennerlein et al. 1998). The most common method reported for measuring muscle force in test animals was by connecting a transducer (in the shape of a buckle) to the muscle tendon, as shown in Figure 6.

Such a buckle typically consists of an arrangement of strain gauges connected to a rigid frame. The tendon of the considered muscle can then be wound through this buckle. The strain measurements are related to an equivalent tensile force developed in the muscle, which is obtained by performing an equivalent calibration procedure (Knudson 2007).

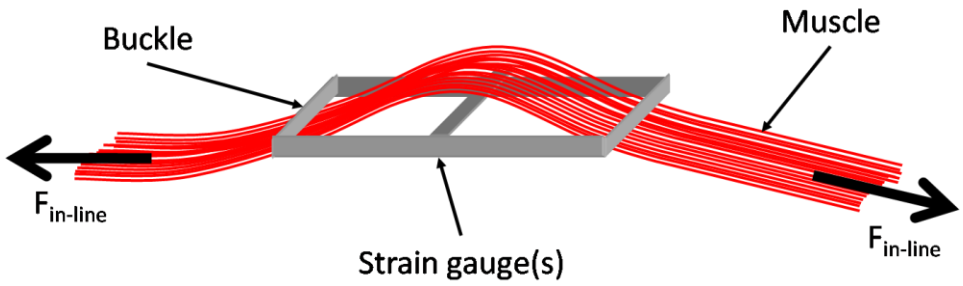

Figure 6: Example of transducer used for in vivo force measurement. Adapted from Knudson (2007).

2.3.5. Musculoskeletal models for force estimation

Complications and restrictions of measuring *in vivo* muscle activity and forces directly necessitate the development of non-invasive procedures to determine the force developed in a muscle. In order to achieve this aim, theoretical models have been developed in which the skeletal and muscle properties are both represented. These models allow theoretical simulations of muscle contraction, ensuring that results are consistent with Newtonian mechanics as well as with known properties of muscles. To successfully describe muscle activity and forces (or components thereof), an appropriate muscle model must be derived or identified for each particular application, after which the input parameters (muscle properties) must be obtained experimentally and/or from published data (Van den Bogert et al. 1998). A number of relevant and important research questions can be answered through the use of these models.

Despite certain limitations and complexities involved, various models have been proposed for simulating muscle activity and forces. All of these models are either based on phenomenological or mechanistic premises (or a combination of both) (Van den Bogert et al. 1998). Phenomenological models are more commonly used and are based on empirical observations of muscle contractions. These are not concerned with representing the mechanism of muscle force production. Most phenomenological models are based on the model first described by Hill (1938). This model describes a muscle consisting of a contractile element in series with an elastic element (both representing the active force in the muscle) and this whole unit in parallel with a series element (representing the passive force in the muscle), as shown in Figure 7.

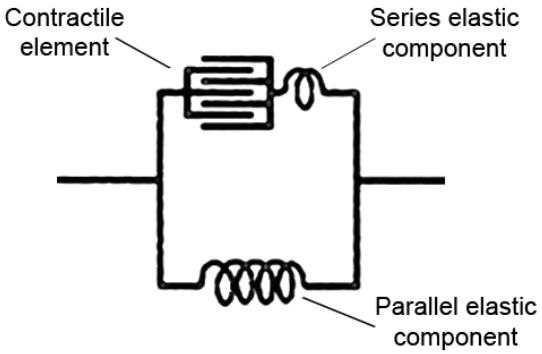

Figure 7: Hill-type model for contraction dynamics of a muscle. Adapted from Peterson (2007).

Contrary to phenomenological models, mechanistic models are built from basic contraction mechanisms and are primarily based on the sliding filament theory of muscle contraction, originally proposed by Huxley (1957).

The main obstacles in modelling the force exerted by muscles are the lack of studies reporting successful validation of muscle force estimates and the usable interfaces for implementing this information in the clinical setting (Erdemir et al. 2007).

An indirect analytical method has also been used to determine joint reaction forces, representing the resultant action of all the muscles crossing that particular joint. This method is called inverse dynamic analysis and often used in clinical gait analysis. It was formulated based on the basic principle that muscles produce skeletal movement and ground reaction forces (Vaughan et al. 1992). The main disadvantage of this method is, however, that it does not represent individual muscles forces, even with the addition of muscle electromyography (EMG) data (Zajac et al. 2003).

2.4. *In vivo* contact force measurements

Many biomedical engineering studies have been requiring the measurement of *in vivo* contact forces, especially in orthopaedic applications. Although many systems have been proposed for use (Otto et al. 1999), two commercially available systems have gained increasing popularity for these types of applications, mainly because of their thinness. These force measurement systems are based on capacitive and piezo-resistive technologies, respectively. Examples of these systems are the Novel AJP system from *Novel* (capacitive) and the Tekscan system from *Tekscan* (piezo-resistive). A recent study reported the comparative advantages of one sensor technology over the other (Martinelli et al. 2006). While conclusions from this study were not made on the most suited measurement system for all types of applications, it provided valuable guidance with this decision, based on the experimental use-conditions.

Concerning Tekscan sensors, reported findings show a number of aspects that needs to be considered to ensure good sensor performance (in terms of accuracy and repeatability), of which the main elements are discussed here. A validation study of these sensors (Luo et al. 1998) reported that Tekscan sensors are sensitive to surface conditions, loading speeds and temperature (especially >30°C). Furthermore, sensors are not suitable for hard surface contact and sensor measurements varied between sensors. Therefore, it is recommended that calibrations be performed for each sensor under the actual experimental conditions. Sensors are also reported to be unable to conform to spherical surfaces and displays creep (drift) artefacts. Furthermore, it is advantageous to distribute a load over the whole sensing area of these sensors (Martinelli et al. 2006).

These abovementioned findings are also reflected in the recommendations for optimal sensor performance made by the Tekscan sensor manufacturer (Tekscan 2005; Tekscan 2008). Recommendations from the manufacturers additional to the abovementioned include treating the sensing area as a single contact point, avoiding shear forces on the sensor and preconditioning the sensors to experimental conditions, i.e. loading and temperature. In addition, sensors need to be calibrated individually over force ranges greater than the expected experimental load ranges and excessively high experimental loads need to be avoided, in order to prevent the sensor from reaching saturation. Furthermore, sensors were found not to be influenced by changes in humidity.

2.5. Comparison of relevant features of baboons and humans

The Chacma baboon (*Papinio ursinus*) and Human (*Homo sapiens sapiens*), hereafter: baboon and human are members of the biological order of primates (Voisin 2006). The Chacma baboon has a body mass ranging from 15 to 31 kg and are quadrupedal (Fleagle 1999) and (Anonymous 2007),

although have also been described to walk on their knuckles or in the classical way (Voisin 2006) (opportunistic bipedal). The average human adult male has a body mass ranging from 76 to 83 kg (Anonymous 2006) and are bipedal. The musculoskeletal material properties of muscles, bones and tendons of both species (and essentially for all mammals) are the same (Biewener 2000). Similar muscle physiology and material properties of mammals meant that the force production of mammalian muscles scales with two-thirds the power of muscle mass, i.e. with cross-sectional area (Marden et al. 2002) (see also Section 2.6).

Baboons and humans have similar shoulder complexes that include 3 bones (scapula, clavicle and humerus), more than 20 muscles (species dependant) and 4 joints. Variations of the morphology of the skeletal structure and allometry of the upper limbs amongst primates depend on the differing upper limb locomotor functions or manipulation behaviour (Voisin 2006). A clavicle enables an animal to have complete mobility of its shoulder joint (adduction, abduction and circumduction), since it functions as a strut to support the shoulder complex (Swatland 1994). However, the clavicle is absent in the shoulder joint of most other large animals available for laboratory use, e.g. pigs, dogs, cats, sheep, etc. These animals possess cursorial limbs – joints adapted for running, which limits the range of physiological limb motion to a large extent. Consequently, animals suitable for laboratory tests, such as baboons, are well suited for comparative studies pertaining to the human shoulder complex.

As mentioned in Section 2.2, the two main muscles associated with pectoral implants of pacemakers are the *pectoralis major* and *pectoralis minor* muscles. In humans, the *pectoralis major* muscle has a wide origin that stretches from the upper six upper costal cartilages, over the sternum, up to the medial half of the clavicle and its two heads (clavicular and sternocostal) and inserts in the lateral lip of the intertubecular sulcus of the humerus (Moses et al. 2005). The *pectoralis minor* originates from the anterior surface of ribs III to V and inserts onto the medial surface of the coracoid process of the scapula (Moses et al. 2005). Both of these muscles are shown in Figure 8.

In an attempt to accurately represent a muscle with such a widely spread origin, previous studies of musculoskeletal modelling of the upper limb represented the *pectoralis major* as three separate muscles, e.g. (Garner et al. 2000; Holzbaur et al. 2005). Each of these separate muscle had its own origins and insertions. Although the locations of the insertions were in near proximity to each other, the origins of the muscles were widely spread out over the chest area, thereby representing the wide area of origin of the *pectoralis major* muscle. The origins of these different muscle segments were the clavicle, sternum and ribs, respectively.

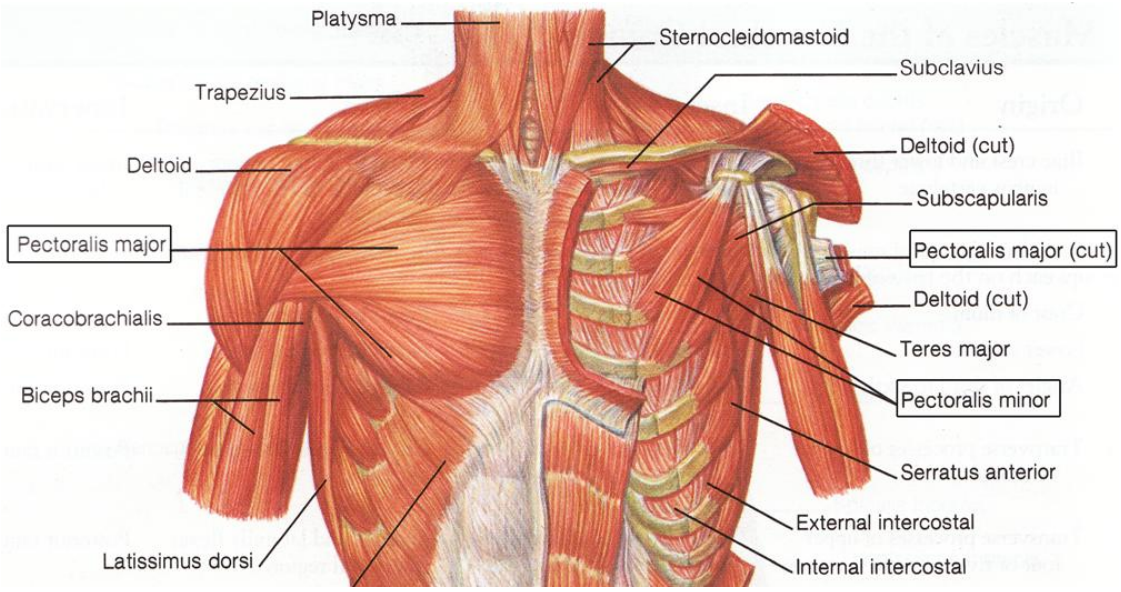

Figure 8: Musculature of the human chest indicating, specifically indicating the two pectoral muscles, i.e. pectoralis major and pectoralis minor, adapted from Van De Graaf (2002)

2.6. Intraspecific and interspecific scaling

2.6.1. Scaling in biology

In a general sense, biological diversity is a matter of size, since the size of an organism plays a very important role in its functioning and survival. Together with the change in size of a physical or biological system, the relationships amongst its different components and processes need to change accordingly to ensure continuation of the normal functioning of the organism. Various anatomical and physiological characteristics of organisms change in such a way that they remain self-similar (even over wide range of scales), i.e. the same relationship between critical structural and functional parameters is maintained. The relationships between these parameters as a function of change in size can be described by a power function, as is well established in biology. In biology, these power functions are also called allometric equations and have the following form:

$$Y = Y_0 M^b \tag{2}$$

In this equation, *Y* is the dependant parameter, Y_0 is a normalization constant (dependent on the measurement unit) and *M* is the independent parameter (typically body mass) and *b* is the scaling exponent. This equation is called allometric, since in biology the exponent *b* is typically not equal to 1 (*b* = 1 – isometric, b ≠ 1 – allometric). One of the most common examples of allometry is geometric scaling. Any object with a self-similar shape can be described to change in surface area or volume as a function of a linear dimension. For example, consider a group of self-similar spheres each with a linear dimension (r), surface area ($A = \pi r^2$), volume ($V = 4/3\ \pi r^3$), mass (M) and density (D). If the density remains constant for all the spheres, and M α V, then the linear dimension, r, or surface area, A, can be expressed as a function of mass as follows:

$$r = Y_1 M^{1/3} \text{ and } A = Y_2 M^{2/3} \tag{3}$$

In this equation Y_1 and Y_2 are the normalized constants that depend on the measurement units. The same principal is valid if organisms that vary in size maintain self-similar shapes. However, in biology, this is usually not the case. The reason for this is that there are very strong constraints on the structure and function of various components that do not allow organisms to preserve the same geometric relationships as size changes over several orders of magnitude. Different parameters have different allometrical (or scaling) relationships, depending on various specific constraints. For many of these parameters, scaling relationships have been found by obtaining empirical data and fitting linear regressions to log-transformed data. Although not necessarily this simple, detailed investigations in obtaining these scaling relationships have been performed. There are still certain scaling relationships that warrant proper theoretical explanation, but certain seemingly universal principals for biological scaling have been proposed.

In biology, scaling relationships have traditionally been studied at three different levels, i.e. within individual organisms, amongst individuals of different sizes and within assemblages of multiple individuals or species of organisms. Furthermore, scaling relationships have been derived for numerous traits ranging from cellular structure to whole organism anatomy and physiology to life history and ecological attributes. Some of these traits include terrestrial support, lifespan, time to reproductive maturity, metabolic rate, force per motor size and heart and respiratory rates, to name but a few.

This section was adapted from Brown (2000).

2.6.2. Scaling in terrestrial support

Scaling with regards to musculoskeletal systems has been investigated in the broad area of scaling relationships in terrestrial support. Considering the differences and similarities of only baboons and humans, these organisms have different sizes and locomotor anatomies made of materials having the same properties. (The locomotor anatomy determines whether an animal is bipedal, opportunistic bipedal, quadrapedal, etc.) This meant that variation exists in the structural mechanical design due to these abovementioned constraints. Constraint in mechanical design of these biological structures exists in particular because all structures are subjected to the same external environment, i.e. gravity. Therefore, the skeletal and musculature elements (with similar material properties) have to possess a sufficient capacity to transmit forces safely, to provide biological support and to enable movement. These factors govern the scaling of the mechanical design of terrestrial support systems of different sizes.

The scaling patterns of different properties of muscle and bone have been reported, as shown in Table 1.

Table 1: Emperical and theoretical scaling patterns of bone and muscle stress in terrestrial animals, adapted from (Biewener 2000). Theoretical scaling relationship for bone and muscle are the same, since scaling relationship is derived from groups of samples (e.g. bone or muscle) having the same density, respectively.

		Area	**Force**	**Stress**
Empirical	**Bone**	$\alpha M^{0.72}$	$\alpha M^{0.73}$	$\alpha M^{0.01}$
	Muscle	$\alpha M^{0.79}$	$\alpha M^{0.73}$	$\alpha M^{-0.06}$
Theoretical		$\alpha M^{3/4}$	$\alpha M^{3/4}$	αM^{0}

Scaling patterns observed for musculoskeletal design of terrestrial mammals suggest that differential mechanical constraints functioned over different ranges of size and taxa (size range typically from 0.1 to 300 kg). No general scaling relationship explains these differences, and simple geometric scaling is not sufficient. For example, the geometric scaling of self-similar organisms means that stresses and strains should increase $\alpha M^{1/3}$ (Eq.(3)). For organisms made of the same material properties, this suggests a drastic reduction in the safety factor of terrestrial support structures of larger organisms. The actual limiting constraints over much of the terrestrial size range are maintaining peak stress (i.e. strength) and safety factors. Theoretically, peak stress scales according to stress similarity, i.e. αM^{0} (Table 1). However, it has been suggested that stiffness is the key constraint in animals of small to medium size ($0.03 < M < 30$ kg). A constraint of stiffness enables effective control of limb motion for animals of smaller size. This is explained best by considering the fact that the force-length relationship in muscles (Section 2.3.3) reveals that the ability of muscles to produce force is greatly reduced at very long lengths (> 20% L_m^0) or very short lengths (< 20% L_m^0). Consequently, when tendons and bones are too slender relative to the forces they needed to transmit, the resulting deflection may require excessive length change of the muscle fibres (L_m^0), placing the muscle at a disadvantage for effective control of limb motion. Empirically, stiffness scales according to geometric similarity, i.e. $\alpha M^{1/3}$ (Eq.(3)).

When comparing parameters between organisms of different sizes, different relationships exist for different parameters depending on the applicable constraints. Parameters that change according to size (allometric relationship) are also referred to as scale-variant parameters (αM^{b}, $b \neq 0$), e.g. bone length, PCSA, etc. On the other hand, parameters that do not change according to size (isometric relationship) are referred to as scale-invariant parameters (αM^{b}, $b = 0$), e.g. muscle density, peak muscle stress, etc. While scale-invariant parameters require size-dependant changes, scale-variant parameters are adjusted in the terrestrial organism design to maintain a constant mechanical safety factor (ratio of failure stress and peak functional stress) or achieve appropriate limb stiffness of their biological support systems, despite differences in size and locomotor anatomy.

Therefore, the main consequence of these constraints on terrestrial mammals (< 300 kg) is that changes in locomotion posture occurrs in order to enable terrestrial mammals to match locomotor forces to the scaling of bone and muscle areas. In other words, posture-related changes take place so that the musculoskeletal structures can adhere to these constraints of stress and/or stiffness. This is evident in the more upright posture of larger animals compared to smaller animals – as revealed in the comparatively more upright posture of humans to baboons.

This section was adapted from Biewener (2000).

2.6.3. Musculoskeletal scaling of pectoral structures between baboons and humans

Evidently there will be differences when considering strength and force requirements of the musculoskeletal systems amongst baboons of different sizes, as well as between baboons and humans that differed in size and locomotor anatomy. Therefore, parameter-specific scaling relationships needs to be considered when scaling parameters amongst different baboons (intraspecific scaling) and between baboons and humans (interspecific scaling), respectively. These scaling relationships also need to take any other required constraints into consideration.

The mechanical properties of vertebrate skeletal muscle are generally scale-invariant (i.e. density, constant stress and strain), while muscle force generating requirements scale proportional to scale-variant changes in muscle fibre cross-sectional area (which is therefore related to the PCSA) (Biewener 2000; Lieber et al. 2000; Marden et al. 2002). In other words, the maximum force produced by the muscle scales linearly with the corresponding PCSA (proportionality), or it would scale to M according to a power function, i.e. $\alpha M^{3/4}$ (Table 1).

Scaling of parameters, used to predict the force produced by muscle, however, have different constraints. It has been suggested by Winby (2008) that crucial parameters of the commonly used Hill muscle model be scaled in such a way as to maintain the force generating characteristics of a musculotendon unit, which is subject-specific. These force generating characteristics are reflected in the optimal muscle fibre length and tendon slack length. Maintaining these properties is best achieved by scaling that preserves the operating range when the muscle was maximally activated.

3. Materials and methods

3.1. Measurement systems

3.1.1. Normal force measurement

Research collaborators developed an *in vivo* normal force measurement system for the acquisition of typical pacemaker *in vivo* loading conditions (i.e. force and acceleration) in acute or chronic animal studies. This system consisted of an instrumented pacemaker (henceforth: IPM), radio frequency (RF) transceivers (2x), PC based data acquisition system and a synchronous video recording system, as shown in Figure 9.

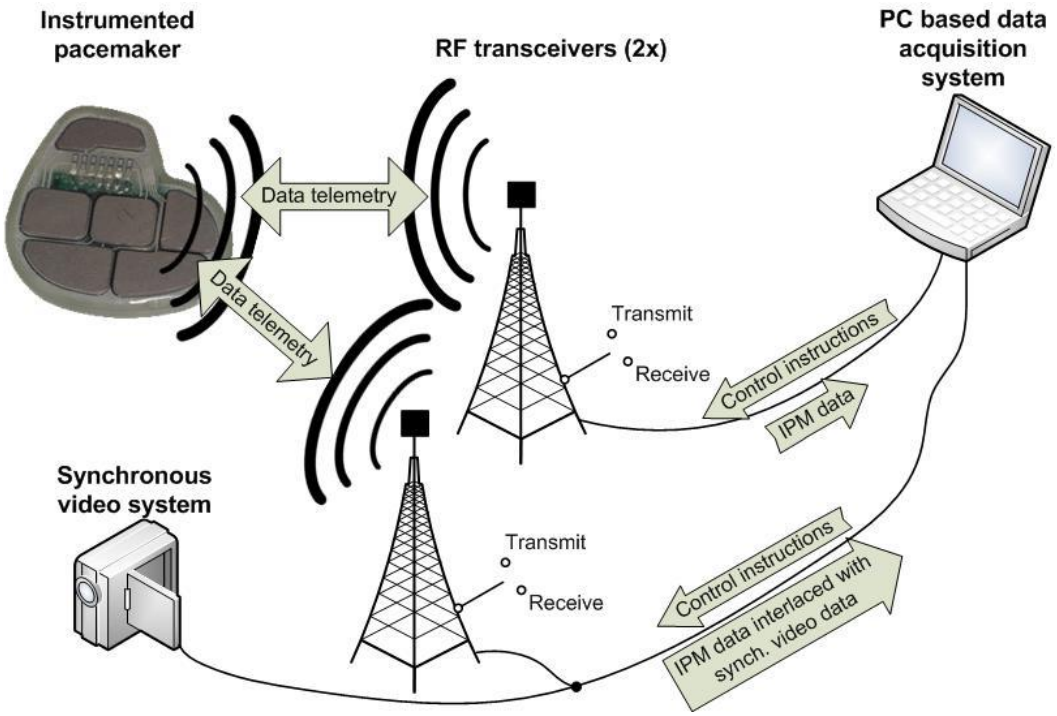

Figure 9: High-level description of the normal force measurement system.

Table 2 and Figure 10 provide details of the custom-built IPM, which comprised the following principal components:

- 6x contact force sensors (custom manufactured for optimal compressive force range of 18-36 N, Tekscan, Boston, MA);
- Sensor cover plates (made from Titanium);
- 1x Three-axis accelerometer (±10 g full scale per axis, Freescale Semiconductor, Tempe, AZ);
- RF based data system;
- Micro-controller;
- Real-time clock;
- High energy lithium battery.

Table 2: Geometric information of the instrumented pacemaker

Description	**Value**
Mass [g]	40
Volume [cm^3]	29
Dimensions (w x l x h) [mm]	64 x 61 x 11
Principal surface area covered with normal force sensors (A_{NT}) [mm^2]	1414
Principal surface area (A_T) [mm^2]	2539
Ratio of force sensing to total area (A_{NT}/A_T) [-]	0.56

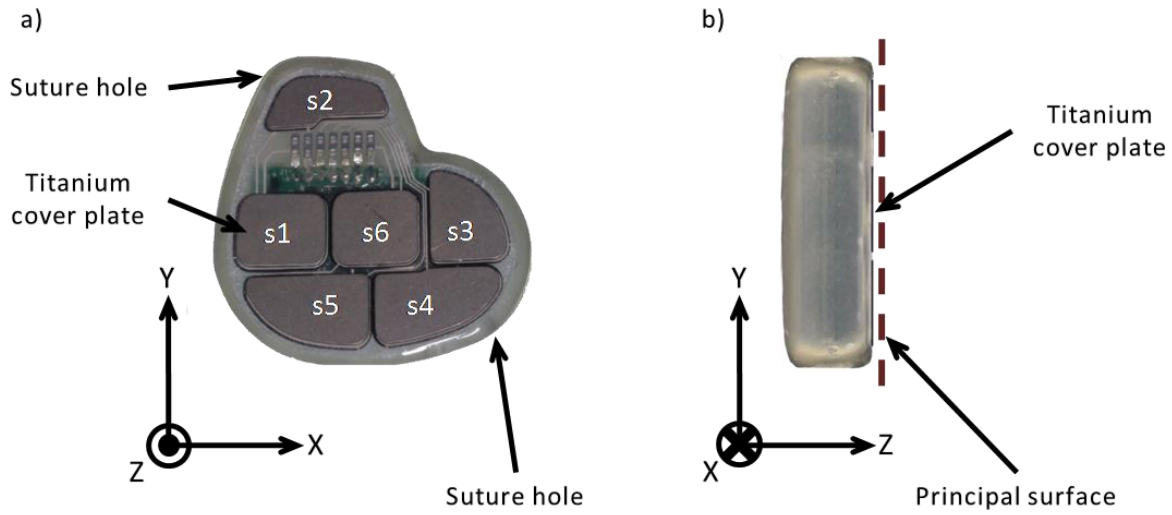

Figure 10: The instrumented pacemaker, indicating the force sensor numbering, the principal surface and the sensor cover plates: a) front view and b) side view.

Table 3: Performance characteristics of the FlexiForce contact force sensors, as reported by its manufacturer (Tekscan 2005).

No	Measure of performance	Description
1	Repeatability	The ability of the sensor to respond similarly to a repeatedly applied constant force: Sensor voltage response changed <±2.5% for a full scale conditioned sensor, when 80% force was applied.
2	Hysteresis	The difference in the sensor voltage response during dynamic applications of the same loads (loading and unloading). Sensor voltage response changed <4.5% of full scale, when 80% force was applied.
3	Drift	The change in sensor voltage when a constant force was applied for a period of time. Sensor voltage response changed <3% per logarithmic time scale for a constant applied force of 90% the sensor rating.
4	Temperature sensitivity	Variance of the sensor voltage to an increase in operating temperature. Sensor voltage response increased <0.36% per °C. The operating temperature range was -9˚C to 60˚C.

The *contact* force sensors from Tekscan will henceforth be referred to as force sensors. Defining characteristics of these sensors were presented in Section 2.4, which include their size (small, thin) and configurability required for this application. Other characteristics pertaining to the sensor performance are shown in Table 3.

As shown in Figure 10, the sensors were all mounted on the principal surface of the IPM, which provided a rigid and flat supporting surface. As per manufacturer recommendation, a piece of rigid material (i.e. sensor cover plate) was placed over each sensor to ensure distribution of the applied force over the whole sensing. Furthermore, the sensor cover plates also prevented application of shear forces on sensors, which can cause sensor damage. In the development stage of the IPMs, it was shown that the contact area, contact location and contact force distribution of a force applied on a single sensor cover plate had no significant effect on the force measured by the underlying

sensor. In other words, the force sensor measured the total resultant normal component (F_N) of the total force exerted on a sensor cover plate independent of contact area, location or force distribution over the sensor cover plate. Therefore, all force measurements reported for the IPM were only measured in the direction normal to its principal plane – e.g. the total force measured by the IPM is the normal component of the total force exerted on the IPM.

The sensors of two of the six IPMs used in these experiments, SN074 and SN076, were assembled on the IPMs in a non-standard manner, as opposed to the standard manner. The non-standard assembly involved inserting a very thin (±0.03 mm) polyolefin gasket around the edge of the sensing area of a sensor. The standard assembly then omitted this additional gasket. The motivation for this non-standard assembly was to attempt to reduce the anticipated "ink conductance" drift of the sensors, which was presumably influenced by the *in vivo* environmental conditions (temperature and humidity), as suspected in development stage of the IPMs (unpublished data).

The accelerometer was mounted inside the IPM assembly, since acceleration was not dependant on sensor location. It measured acceleration in the x-, y- and z-direction as indicated in Figure 10.

The component assembly was encapsulated in a medical grade epoxy cast in the shape of a commercially available pacemaker structure and hermetically sealed to withstand *in vivo* environmental conditions and sterilization procedures. Suture holes were drilled into the epoxy cast for locating the device *in vivo*.

The IPMs used in these experiments provided the means of measuring *in vivo* (normal) force magnitudes and acceleration exerted on the device as a function of time. These IPMs did not have any pacing capabilities and hence no pacing tests were conducted in these experiments.

The function of the RF telemetry system was to control and facilitate transmission of force sensor and accelerometer data from the IPM (henceforth: raw IPM data) to the data acquisition system. The *force* sensors and accelerometers had a maximum response time of 5 µs and 1 ms, respectively. Data transmission occurred at a 10-bit data resolution and a maximum sampling frequency 1000 Hz (signal quality dependant). The sampling frequency was deemed sufficiently fast for this application, due to the relatively long time required for significant change in force exerted on the sensors. This relatively long time was simply due to actual physical movement or muscle contraction that had to occur to exert a significant change in force on a sensor, which was comparatively slow. Furthermore, acceleration was an auxiliary measured parameter of which the magnitude at such high frequencies was not of critical importance. To prevent premature depletion of the IPM battery, pre-programmed operation modes were developed. These operation modes enabled the device to only transmit data for a specified period of time. At the end of this period, data transmission ceased and the device returned to a default "sleep" mode using minimal battery power. An instruction sent via the RF transceiver can activate (or "wake up") data transmission for a period of time specified by the user.

The RF transceiver was connected via a serial connection to the RS232 port of the PC (laptop) that controlled data acquisition with custom code in LabVIEW (National Instruments Corp., Austin, TX). Synchronous video footage was also recorded in order to relate type of activity performed by/on the considered test subject, to the forces and acceleration measured by the IPM.

Data acquired from the IPMs consisted of two datasets with exactly the same sensor data when synchronous video was recorded (Figure 9), i.e., raw IPM data and raw-interlaced IPM data. The latter were raw IPM data interlaced with synchronous video recordings. For some monitor events no raw-interlaced IPM data were recorded, since no synchronous video footage was recorded during certain monitoring events. Different datasets were recorded according to need, i.e. when extra IPM data needed to be recorded without the need for video equipment setup and extra video data storage, only one dataset was recorded (raw). Alternatively, when information about a specific movement was needed together with the IPM data, both datasets were recorded (raw and raw-interlaced). The most suited data set was used for the required analysis.

3.1.2. Electrical stimulation and in-line force measurement

This system consisted of an electrical stimulation (eStim) component as well as an in-line force measurement component. It was developed to artificially induce a muscle contraction of an anaesthetized baboon muscle and then to measure the resultant force, or the in-line muscle force (F_{IL}), developed in that particular muscle.

The eStim component consisted of a standard neuromuscular stimulator (FHC, Bowdoin, ME) which sent electrical impulses via wired pre-gelled surface electrodes sutured to the exposed muscle of interest near its origin and insertion, respectively. The in-line force measurement component consisted primarily of a custom-made buckle strain transducer, a Wheatstone-bridge amplifier and code written in LabVIEW.

The custom-made buckle strain transducer consisted of a rectangular, stainless steel frame, a removable crossbar and two strain gauges, as shown in Figure 11a. The frame was made of square bars (4 mm) and had outer dimensions of 66 x 100 mm, while the crossbar was a half cylinder with ø4 mm that located onto the frame. Data transmission of the analogue strain gauge signal was digitized and transmitted at the same sampling frequency as the IPM data, although extra processing of this strain gauge signal caused a delay of the strain gauge signal relative to IPM data of approximately 0.5 s. Digitized strain gauges data from the buckle strain transducer had resolution of approximately 0.01 V.

To attach the buckle to the muscle, the muscle was exposed by removing overlying skin, and isolated by bluntly dissecting soft tissue surrounding the muscle. The rectangular frame was then placed over the largest portion of the muscle which also covers the IPM, after which the muscle was pulled through the frame and finally the removable crossbar was inserted underneath the muscle, as shown in Figure 11b. The forces exerted by a contracting muscle wound through the buckle as described above are also shown in the figure. The deformation measured by the strain gauges was then related to the F_{IL} developed in the muscle.

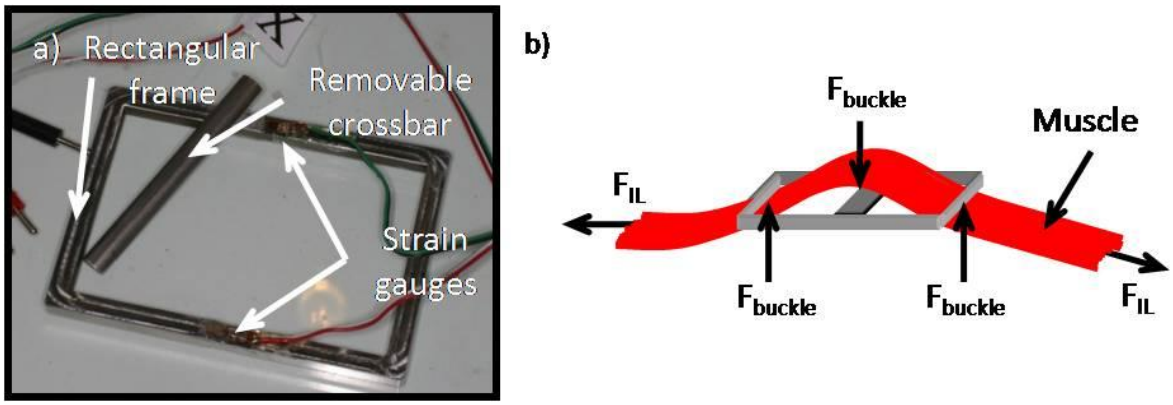

Figure 11: Buckle strain transducer: a) picture and b) schematic illustration of how the muscle was wound through the buckle and how the contracting muscle exerted a force on the buckle.

3.2. Preconditioning and calibration

3.2.1. Force sensor preconditioning and calibration

Manufacturers of the contact force sensors recommended preconditioning and calibration as essential to achieve accurate results from converting sensor voltage, V_N, to sensor force, F_N, since it lessened the effect of drift and hysteresis. The preconditioning and calibration procedures are described below.

3.2.1.1. Preconditioning

Preliminary studies of these force sensors mounted on an IPM revealed that changing experimental conditions (loading and temperature) caused the sensor measurements to drift and changes in the measurement sensitivity. This drift was best observed in the change of the zero-load offset sensor voltage, V_{Noff}. The zero-load force at V_{Noff} was defined as F_{N0} (i.e. F_{N0} = 0 N). The change in sensitivity was best observed in the change of the calibrated voltage range of the sensor, ΔV_{Ncal}. To illustrate these changes, consider a sensor that had a constant preload for a relatively long period of time, after which the preload was reduced to zero. Immediately after reducing the load to zero, the sensor was first calibrated, and then again an hour later. These two calibration curves are shown in Figure 12 and clearly illustrate the change of V_{Noff} and ΔV_{Ncal}.

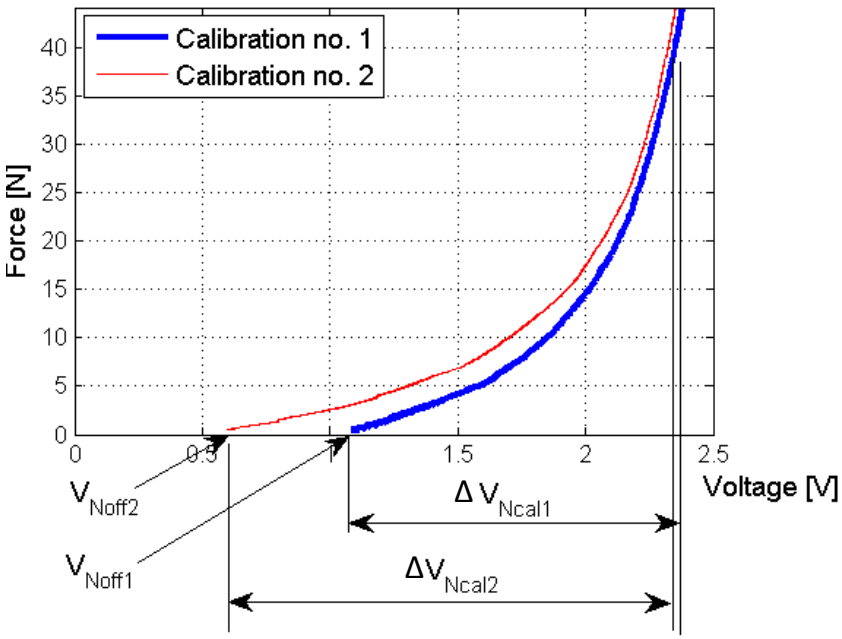

Figure 12: Two calibration curves for the same sensor at sequential time points (>1 hour), displaying sensor drift and change in sensitivity. These changes were reflected by the calibrated voltage range (ΔV_{Ncal}) and the zero-load voltage offset (V_{Noff}), respectively.

Sensor behaviour observed in preliminary studies and obtained from literature were considered to make the following assumptions regarding the change of ΔV_{Ncal} and ΔV_{Noff} for each sensor mounted on an IPM:

1. ΔV_{Ncal} and V_{Noff} were only determinable by a calibration procedure;
2. Preconditioning of the sensor was required for stabilization of ΔV_{Ncal} and V_{Noff} which involved simulating typical experimental conditions (loading and temperature);
3. A change in the preload (or resting load or constant load) on the sensor, F_{Nrest}, had the following influence on the calibration curve over a period of time: if $F_{Nrest2} > F_{Nrest1}$ then $V_{Noff2} > V_{Noff1}$;
4. A change of temperature had an influence on ΔV_{Ncal} and V_{Noff};
5. A change in ΔV_{Ncal} and V_{Noff} during these experiments, occurred at a sufficient rate to be classified as stable during an experimental recording duration of a sensor;
6. Sensitivity and the drift of V_{Noff} for a stabilized sensor remained stable amidst acute changes in F_N.

Preconditioning of the IPMs prior to implantation consisted of preloading each sensor ($F_{Nrest} > 0$) and simulating *in vivo* environmental conditions (humidity ≅ 100%, T_{amb} = 37˚C) for a period of 4 weeks. The sensors of SN066 were not preconditioned, since this device was only used for electrical stimulation experiments, and it was assumed that the F_{Nrest} would be negligibly low during these experiments.

From the pre-study feasibility studies, developers concluded that preconditioning would assist in reaching high confidence sensor stability for reliable estimations of the *in vivo* sensitivity and drift.

3.2.1.2. Calibration

All force sensor calibrations were performed on a universal testing machine with a 500N static load cell, using accompanying Merlin software (Instron 5544, Instron Corp., Norwood, MA). Each sensor was calibrated individually. Calibration involved using the Instron to apply a ramping compression force from 0 to 44.5 N (10 lbs) at a cross-head speed of 0.254 mm/min with a Ø9.5 mm stainless steel pin (flat contact surface) on the centre of the sensor cover plate of the sensor being calibrated. Transmission of IPM data was activated to enable sensor data and Instron force data to be recorded simultaneously. The IPM was located with a custom locating fixture during the calibration procedure, as shown in Figure 13.

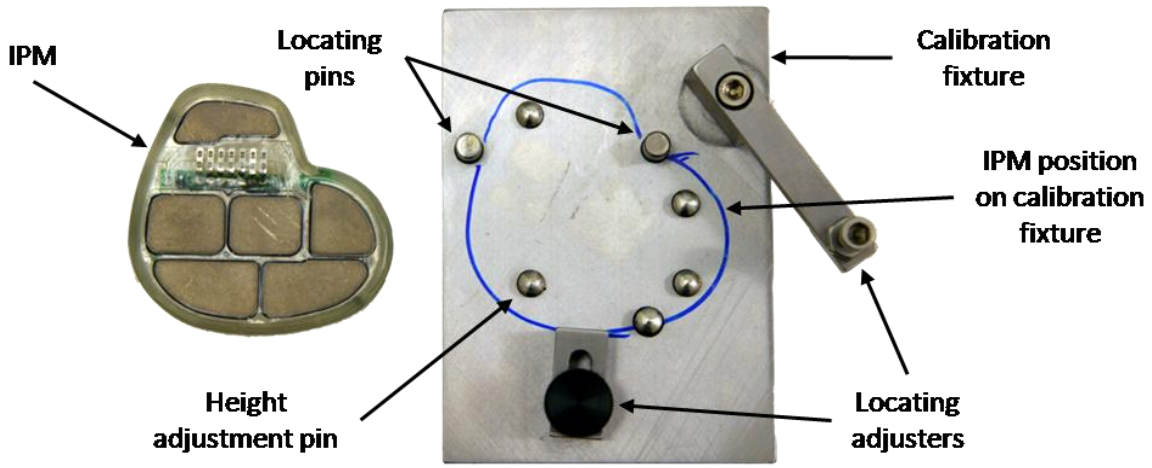

Figure 13: Instron calibration fixture for instrumented pacemaker (IPM), showing different locating and adjusting settings for preventing any movement of the IPM during calibration procedures.

Pre-implant calibrations were performed for each sensor, once at 15 days, and twice at 2 days prior to implantation (-360hr, -48hr, -47hr), during the preconditioning phase at T_{amb} = 37°C. Ethylene oxide sterilization of the unloaded IPMs (F_{Nrest} = 0 for each sensor) was performed 1 day prior to implantation, which included having ambient temperature at 55°C and relative humidity of 0.6 for 12 hours. Post-explant calibrations were performed for each sensor and consisted of three calibration events (c1, c2 or c3) at 4 hours, 24 hours and 48 hours post-explant (04hr, 24hr, 48hr) at T_{amb} = 20°C. The sensors of two IPMs, SN074 and SN076, were not calibrated at 48 hours post-explant. The sensors of SN066 were only calibrated once prior to electrical stimulation experiments, since it was only used in the electrical stimulation experiments.

The Instron force data and the corresponding sensor voltages were correlated to create sensor-specific calibration curves using code in MATLAB (MathWorks Inc., Natick, MA). Due to factors influencing sensor sensitivity and drift (e.g. fibrotic encapsulation of implanted IPM, changing F_{Nrest}), as well as the relatively short time interval between experimental data acquisition and post-explant calibrations, a post-explant calibration curve was chosen for each sensor which was assumed to be most representative of its behaviour *in vivo*. The most suited post-explant calibration curve was the curve that displayed the smallest ΔV_{Ncal}. This choice criterion presumed that both F_{Nrest} and T_{amb} dropped upon explantation. This decline of F_{Nrest} and T_{amb}, combined with the effect of applying a load on a sensor during a calibration event, were assumed to cause the gradual increase of ΔV_{Ncal} (and decrease of V_{Noff}) over time.

To accommodate for the effect of a changing V_{Noff}, the calibration curve for each sensor was offset by its V_{Noff} to start from the origin (offset to origin). Hereafter it was approximated with a 5th degree polynomial, as shown in Figure 14. These polynomial functions fitted on the post-explant calibration curves for each sensor.

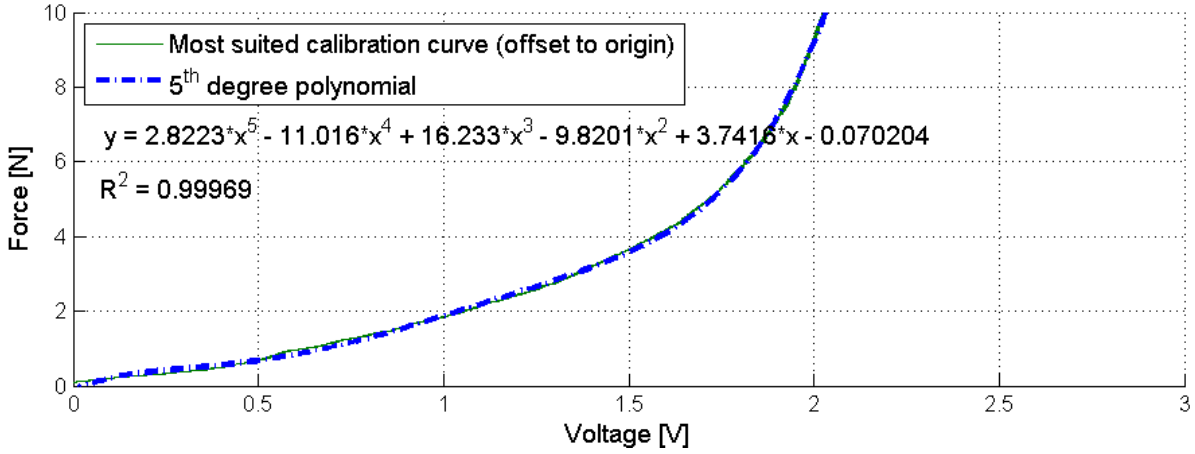

Figure 14: Example of a post-explant calibration curve of a force sensor that was offset to the origin and fitted with a 5th degree polynomial function.

3.2.2. Accelerometer calibration

The calibration procedure that was sufficient for the three-axis accelerometer consisted of the following: The IPM was held in different rest positions in line with the known axes of acceleration, to cause a 1g, 0g and -1g gravitational acceleration on each axis of acceleration respectively. A straight line was fitted through these accelerometer measurements for each axis of acceleration which was used for converting accelerometer voltages, V_{ax}, V_{ay} and V_{az}, to acceleration, a_x, a_y and a_z, respectively.

3.2.3. Buckle strain transducer calibration

The buckle strain transducer of the in-line force measurement system was received pre-calibrated from research collaborators. The calibration curve for the buckle was adjusted to the origin, which meant that the buckle strain transducer voltage data, V_{IL}, was offset to zero in order to convert and consequently converted to the in-line force of the muscle, F_{IL}. Data from preliminary studies revealed that the voltage signal of this buckle strain transducer was repeatable, accurate and did not drift.

3.3. *In vivo* loading environment of the instrumented pacemaker in the baboon

3.3.1. Experimental design

An overview of the approach to acquire the *in vivo* data from the baboon part of this study is presented in Figure 15. After ethics approval, the procedures and experiments outlined below were performed for each implanted IPM, unless indicated otherwise. A series of experiments consisted of different experiments performed under similar experimental conditions (loading and temperature). Each experiment involved acquisition of force sensor and accelerometer voltage data (and possibly synchronous video data) over the duration of a single activation period of the IPM. A single activation period of the IPM did not last for more than 5 minutes, before it returned to a "sleep"

mode where sensor data was no longer transmitted. The system design only enabled data acquisition from a single IPM at a time. The sequence at which different series of experiments were performed, as well as other important time points are indicated in this figure. Experiments on the conscious baboons were performed over eight days per animal, while experiments on anaesthetized were performed over three hours per animal. Experiments on the anaesthetized baboons were performed three to seven days after the experiments on the conscious baboons. Animal preparation and experimental setup prior to ROM experiments took approximately 30 minutes, and prior to eStim experiments took approximately 20 minutes.

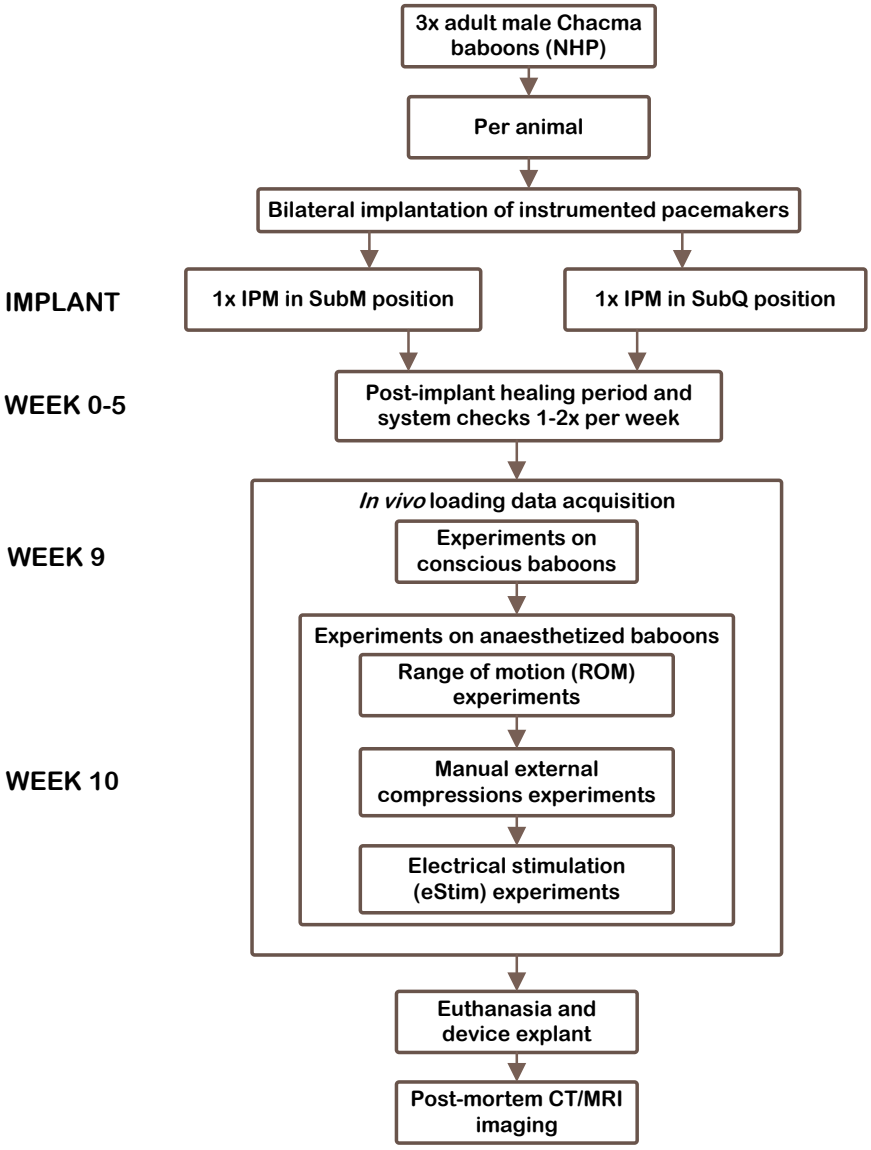

Figure 15: The approach to in vivo data acquisition from baboon and timelines from implantation to final data acquisition

The study was approved by the appropriate institutional review boards of the University of Cape Town (RECREF: 007-022). All experimental procedures described below followed the detailed instructions of the approved protocol, although the description given below only summarizes these procedures. The protocol focused on the replacement, refinement and reduction of the use of

animals as put forth by internationally recognized protocols in the humane use of laboratory animals (Robinson 2005).

3.3.2. Implantation, post-implant healing and system checks

The implantations of the IPMs were performed using standard surgical techniques for sub-coetaneous (subQ) and sub-muscular (subM) implantation of cardiac pacemakers in humans.

Implantations of the IPMs were performed bilaterally in the pectoral region of three adult male Chacma baboons (weight at time of implant: 20.6 ± 1.15 kg) in the subQ and subM position, respectively. These IPMs were oriented with the positive z-axis facing outwards (Figure 10) and with the device in any suitable rotation. Upon insertion into the bluntly dissected pocket, the IPM was sutured to the overlying (for subM) or underlying (for subQ) *pectoralis major* muscle. The pectoral region of a Chacma baboon, immediately after implantation of the subQ and subM devices, is shown in Figure 16.

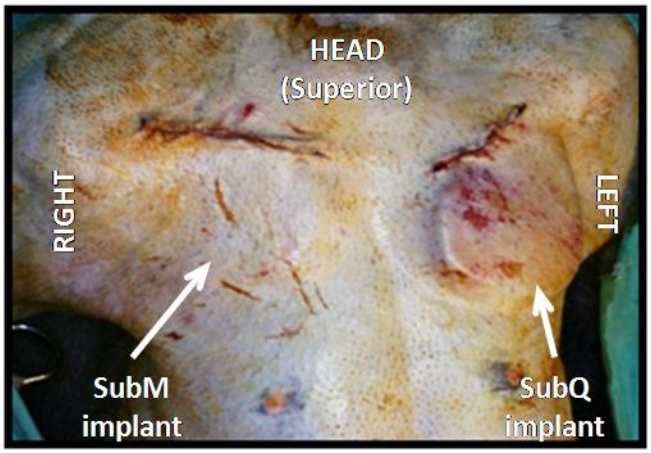

Figure 16: Pectoral region of Chacma baboon immediately after implantation of the IPMs. The different implant positions (subQ and subM) are indicated.

A six-week healing period was planned after implantation to allow wound healing and fibrous encapsulation of the IPMs before commencing with experiments on conscious baboons. IPM function and telemetry operation were checked once or twice a week during this period to ensure proper functioning of equipment. This was done by simply “waking up” each IPM for a short period of time and confirming sensor function and proper signal reception.

3.3.3. Experiments on conscious baboons

The aim of these experiments was to obtain sufficient loading data as an indication of typical *in vivo* loading conditions during conscious activities. It also served to obtain synchronous video and IPM data for correlating the conscious activity performed by the baboon to the force measured by the IPM.

These experiments were performed at the holding facility with the animals kept in indoor cages. Data was acquired during repeated sessions (experiments) daily, totalling data acquired for 5 - 15 minutes daily over 6 non-consecutive days, utilizing increased activity of the baboons prior to routine feeding. As many different recordings were performed as were feasible. These conscious activities performed by the baboons were expected to include pulling, pushing, climbing or other relevant activities that would exert forces on the implanted IPM.

3.3.4. Experiments on anaesthetized baboons

The aim of these experiments was to determine the cause and the magnitude of forces exerted on the IPMs under more controlled experimental conditions.

All experiments on the anaesthetized baboons were performed in the sequence listed below over approximately three hours, prior to the explantation of the IPMs. Each series of experiments consisted of three experiments per IPM (<100 seconds per experiment), except for the electrical stimulation (eStim) experiments, which consisted of thirteen experiments per IPM (<25 seconds per experiment).

3.3.4.1. Range of motion experiments

The *in vivo* position of the IPM, as well as the forces exerted on the implanted IPM during physiological ranges of motion (ROM) of the upper arm were investigated in these experiments. The ROM experiments consisted of two separate series of experiments, namely fluoroscopy ROM and force measurement ROM experiments. The fluoroscopy ROM experiments only involved the recording dynamic fluoroscopic data, while force measurement ROM experiments only involved the recording IPM and synchronous video data.

For both series of experiments, the applicable arm of the baboon was moved through physiological ranges of motion in each experiment. The following movements were performed:

- Adduction and abduction, defined as the arm pivoting around the shoulder joint in the axial plane – towards and away from the sagittal plane, respectively;
- Elevation, defined as the pivoting of the arm around the shoulder joint in the sagittal plane – towards and away from the axial plane, respectively;
- Circumduction, defined as the pivoting of the arm around the shoulder joing in the coronal (frontal) plane;

Due to the physiological limits to the ranges of upper arm motion, these movements did not necessarily occur purely in a single plane as described above, and therefore the convention described in Figure 17 was adopted. These descriptions of upper arm positions were all defined relative to the anatomical position, i.e. arms next to side of test subject, palms facing the anterior, as described by “El,0° - Abd,0°”. The relatively large anterior-posterior thickness of the baboon thorax caused the upper arms to rest on the operating table at an angle of about 10° in the negative direction, described by “El,-10° - Abd,0°”. The F_{NTrest} for each IPM was recorded with the arm in this position.

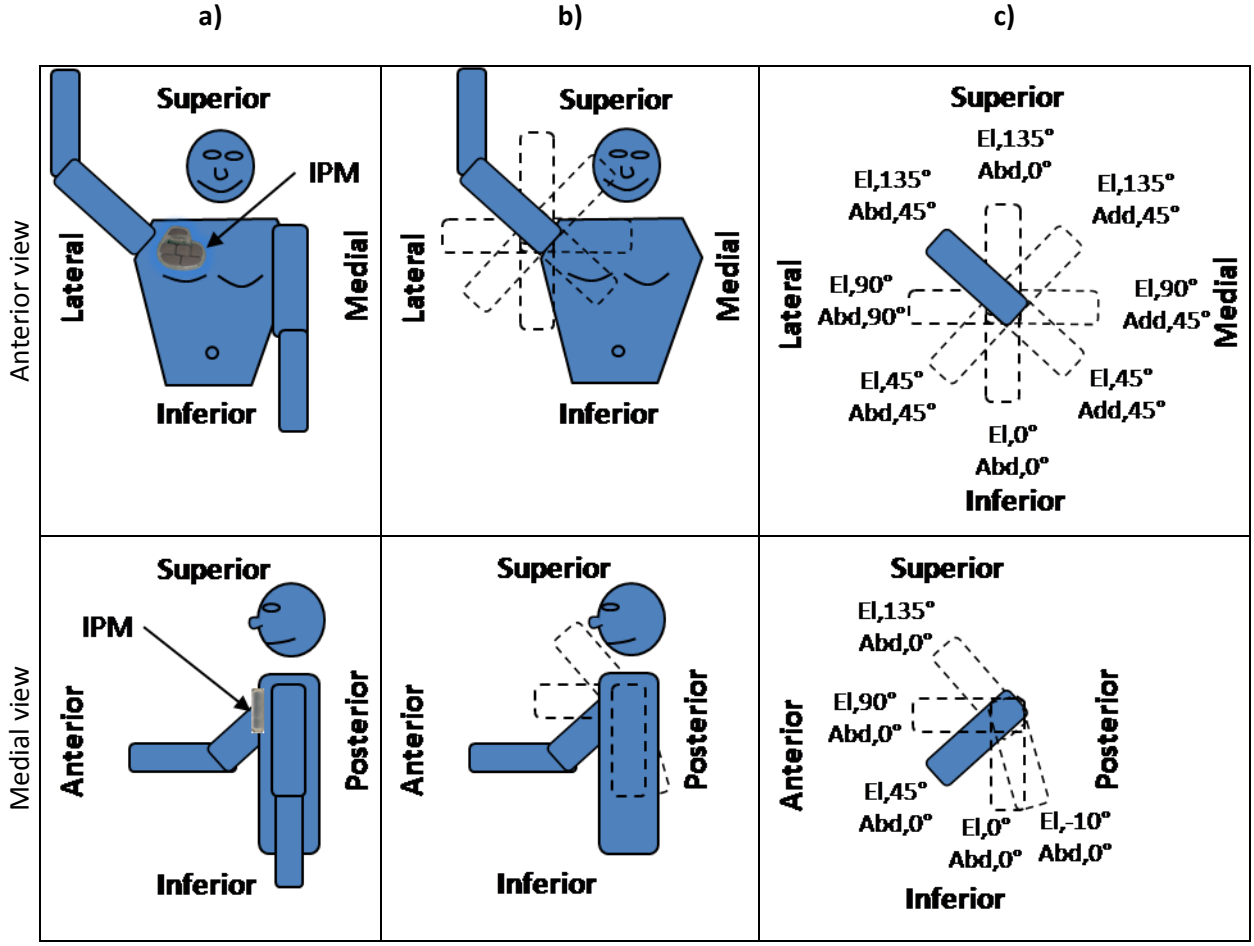

Figure 17: Convention of key upper arm positions used in the ROM experiments, illustrated on an IPM implanted on the right side, showing both anterior and medial veiws of these positions: a) the position of an IPM implanted relative to the arm, b) the different physiological ranges of motion positions of the upper arm and c) definitions of the different upper arm postions.

3.3.4.2. Manual external compression experiments

Relating the manual externally applied compressions to the *in vivo* responsiveness and accuracy of the IPMs was performed during these experiments. This was achieved by applying a series of known compressive forces with a Chatillon digital force gauge (AMETEK, Inc., Largo, FL.) over the implanted IPM, whilst recording Chatillon, IPM and synchronous video data. This Chatillon digital force gauge was received pre-calibrated from research collaborators.

Two series of these experiments were performed using the Chatillon. The first with a 76 mm and the second with 12 mm endplate connected to the Chatillon. These series of experiments will henceforth be referred to as the 76 mm Chatillon and the 12 mm Chatillon experiments respectively, and be abbreviated as chat76 and chat12, respectively. The endplates used were circular, flat, rigid disks, which were rigidly connected to the Chatillon. The size and shape of the IPM and its sensors compared to the different endplates used are illustrated in Figure 18.

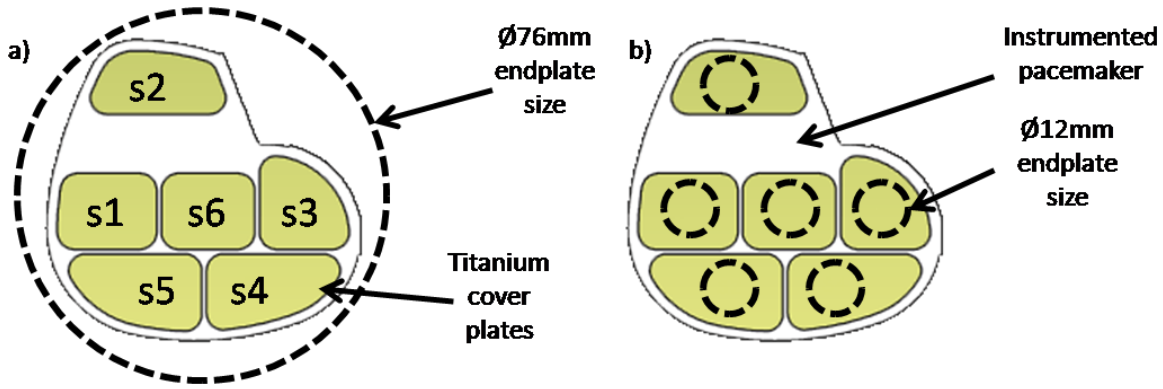

Figure 18: Size and shape comparison of instrumented pacemaker to Chatillon digital force gauge endplate: a) 76 mm endplate and b) 12 mm endplate

3.3.4.3. Electrical stimulation experiments

These experiments involved the measurement of the total force on the IPM (F_{NT}) and corresponding in-line forces developed by the portion of the *pectoralis major* muscle overlying the IPM (F_{IL}) at different levels of electrical stimulation (eStim) of the muscle. Since these experiments only considered subM IPMs, the subQ IPMs were explanted, while acute, previously unused, pre-calibrated IPMs were implanted in the newly available subM positions. Therefore, for the eStim experiments, each baboon had two IPMs implanted bilaterally in the subM position – one chronically used and encapsulated IPM and the other acutely used and unencapsulated IPM.

The normal force measurement, electrical stimulation and in-line force measurement systems were combined in this experimental procedure, as illustrated in Figure 19. The portion of the *pectoralis major* muscle overlying the IPM was exposed and isolated for electrical stimulation.

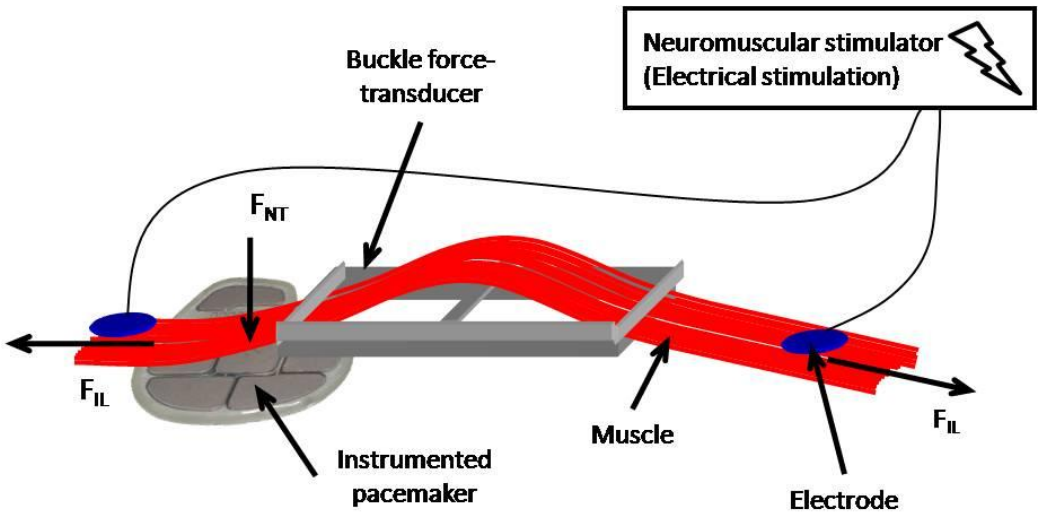

Figure 19: Representation of experimental setup of anaesthetized eStim monitor sets

Each exposed and isolated muscle received one of two predetermined series of eStim events. An eStim event consisted of a train of 2000 pulses, with a 53 µsec pulse duration and a 203 µsec interval between pulses (train interval), while the current amplitude level was held constant at the specified discrete amplitude. This type of electrical stimulation is also referred to as constant frequency trains (CFT) (Section 2.3.2) and was followed since it was a simple way of mimicking normal physiological neuromuscular stimulation patterns. A series of these eStim events consisted of 13 discrete unsorted

levels of electrical current amplitudes between 3 mA and 35 mA. This amplitude range was chosen in an attempt to cover minimal through maximal muscle activation, while the sequence was unsorted in an attempt to minimize muscle fatigue.

During each experiment, the arm of the anaesthetized baboon was constrained to the theatre table in the anatomical position, while the shoulder complex was left to move freely during contraction of the muscle. This setup was conducive to produce the concentric (non-isometric) contraction of the stimulated muscle. The force developed in the stimulated muscle was measured by the buckle strain transducer. The actual setup of these experiments is shown in Figure 20. No synchronous video data were recorded for these experiments. After the eStim experiments, the IPMs were explanted.

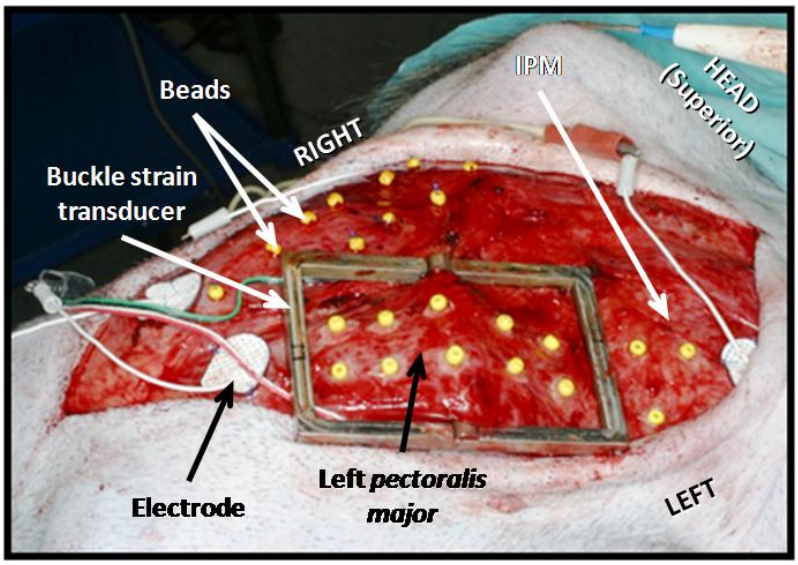

Figure 20: Experimental setup of the electrical stimulation (eStim) experiments. Beads glued to the surface of the muscle assisted the analysis of dimensional changes due to muscle contraction with a two camera orthogonal setup (not part of this study).

3.4. Morphometric measurements

Morphometric measurements were performed post-mortem, which included measurements of musculoskeletal morphology surrounding the IPM and mass and volume of target muscles.

The portion of the *pectoralis major* muscle that was expected to cover the IPM was considered to be the portion connected to the sternum, relative to the reported location of these implants in humans (Section 2.2). This portion of the *pectoralis major* muscle will henceforth be referred to as the *pec major* (sternum).

The thickness of the *pec major* (sternum) at the IPM ($t_{m,cb}$), its width at the IPM ($w_{m,IPM}$) and its width at buckle crossbar ($w_{m,cb}$) was measured with a calliper. The muscle length (L_m^{meas}) was measured *in situ* with a ruler following the estimated line of action *pec major* (sternum). After these measurements, the IPMs were explanted and the whole *pectoralis major* muscle was excised and weighed (M_m). Thereafter, the excised muscle was placed in a measuring beaker filled with water to determine its volume (V_m) by measuring the rise in water level after total immersion of the muscle in the beaker.

Medical imaging data (MRI and CT) of the thoracic region of the test subjects were obtained to determine the *in vivo* position of the IPMs relative to the surrounding musculoskeletal structures. Non-functional IPMs, suited for imaging purposes, replaced the functional IPMs. This prevented potential electrical damage to the devices and medical imaging equipment during the imaging procedures. Human medical imaging data was obtained from the NIH Visible Human Project's male specimen, i.e. the Virtual Human Male (VHM) (Spitzer et al. 1996; Garner et al. 2000).

Imaging data were imported into MIMICS software (Materialise NV, Leuven, Belgium) where skeletal structures, together with the *in vivo* position of the IPM (only in baboons), were isolated using thresholding operations.

3.5. Histological analysis

Histological analysis was performed to determine the normality of the fibrotic capsule tissue by evaluating the presence and abundance of cells typically found during the inflammatory process of fibrotic capsule formation around an implanted foreign body. After obtaining M_m and V_m, tissue samples of the fibrotic capsule and overlying muscles were collected from the subM implant locations for histological analysis. This analysis included H & E staining to distinguish between cell nuclei and cell bodies, as well as CD68 fluorescent staining to identify cells associated with this inflammatory response.

3.6. Data Analysis

3.6.1. Pre-processing of raw instrumented pacemaker data

The pre-processing of IPM data was required for conversion of force and acceleration sensor data to the actual forces and accelerations measured. The raw-interlaced dataset was stripped from the synchronous video data and appropriate timestamps were added to corresponding data points. Thereafter, both datasets contained only raw IPM data and will henceforth only be referred to as raw IPM data.

The following pre-processing steps were performed on the raw IPM data prior to the conversion to force or acceleration:

1. A median filter (n = 7) was applied to the data to smoothen extreme local maximum signal spikes. This filter has an acceptably low influence on the sought after local maxima of the force sensor signals;
2. Thereafter, a Fourier transform was performed on the raw IPM data to establish the presence of distinct RF noise in the data. Distinct noise can be clearly observed in the frequency domain of the data and can be removed accordingly, after which an inverse Fourier transform yields IPM data having the noise removed.

Although these filtering techniques improved the signal quality, it did not guarantee the complete removal of noise from the recorded signals.

3.6.2. Conversion of force sensor data from voltage to force

The force sensor voltage measurements (V_N) must be converted to the force sensor force measurements (F_N) using the available post-explant calibration curves. However, the inability to obtain the actual calibration curve for a sensor *in vivo* necessitated the approximation of this

calibration curve *in vivo.* This approximation was complicated by the fact that the sensors were shown to change in sensitivity and drift (best reflected in ΔV_{Ncal} and V_{Noff}) due to changing experimental conditions (loading and temperature), as explained in Section 3.2.1.1. Furthermore, median filtering of the force sensor data only removed maximum noise spikes caused by RF noise (minimum noise spikes were still present).

The approximation quality of the calibration curve representing the *in vivo* conditions was important, since it determined the accuracy of resulting F_N. Therefore, a voltage-force conversion method was developed to accommodate for the observed sensor behaviour. It was achieved by adjusting the *in vivo* V_N data for use with the most suited post-explant calibration curves, in order to obtain F_N data. The V_N data was converted to F_N data using the following equation:

$$F_N = f_2\left(V_N - V_{Nvmin}\,{}^{series\,,d}_{exp\,,m}\right) \tag{4}$$

This equation yields a sensor force data point (F_N) and required the following inputs: the measured sensor voltage data point (V_N), the valid minimum sensor voltage over the whole series of experiments, but specific to that particular experiment where V_N was measured ($V_{Nvmin}\,{}^{series\,,d}_{exp\,,m}$) and the 5th order polynomial function that described the most suited calibration curve of that particular sensor that was offset to the origin (f_2).

The formulation of a custom high-pass filter to exclude unwanted minimum noise spikes, as well as the derivation of Eq. (4) is expanded upon in Appendix A.2.

3.6.3. Conversion of accelerometer data from voltage to acceleration

The calibration of the accelerometers described in Section 3.2.2 yielded the following conversion algorithms for each accelerometer axis,

$$a_{Nx} = 8.33(V_{ax} - 0.75);\ a_{Ny} = 8.33(V_{ay} - 1.21);\ a_{Nz} = 8.33(V_{az} - 1.35) \tag{5}$$

3.6.4. Conversion of buckle strain transducer from voltage to force

The calibration of the buckle strain transducer referred to in Section 3.2.3 yielded the following conversion algorithm with the combined strain gauge voltage, V_{IL}, minus the combined resting strain gauge voltage, V_{ILrest}, as input,

$$F_{IL} = 462.62(V_{IL} - V_{ILrest}) \tag{6}$$

The value of V_{ILrest} was subtracted from V_{IL}, since the passive force component of the portion of *pectoralis major* muscle considered, was assumed to be zero – i.e. $F_{ILrest} \cong 0$.

3.6.5. Extracting resting sensor voltages

Obtaining the correct resting sensor voltage was required for calculations concerning the voltage-force conversion of force sensors data (Section 3.6.2), as well as for voltage-force conversion of the buckle strain transducer data (Section 3.6.4). Obtaining these resting sensor voltages from single data points was considered to be ineffective, since the sensor voltage signal either slightly varied or

it had low signal resolution. Therefore, a period of rest was identified in the signal, and this "resting" signal was averaged over this period of rest to obtain the resting sensor voltage, i.e. V_{Nrest} for force sensors and V_{ILrest}.for the buckle strain transducer.

For the force sensors, the resting period was identified by observing the activity of the embedded accelerometer signal together with the force signals. Relative inactivity of all of these sensors was deemed sufficient as a period of rest. For the buckle strain transducer, the resting period was easily identified as the period prior to the application of the eStim amplitude.

3.6.6. Post-processing of force data from force sensors

3.6.6.1. Calculation of total force experienced by instrumented pacemaker

The principal surface of the IPM consisted of an area covered with sensors and an area not covered in sensors. The force exerted on the area not covered with sensors was calculated by assuming a uniform force distribution over this area, which was equal to the mean of the force measured by all sensors. Therefore, knowing the force measured per sensor (F_{Nx}) and the area of each sensor (A_{Nx}), the force distribution on the surface not covered by sensors was expressed as,

$$D_D = \frac{\sum_{x=1}^{n} F_{Nx}}{\sum_{x=1}^{n} A_{Nx}} \qquad \text{(with } n = 6\text{)} \tag{7}$$

Considering this area of the principal surface not covered by sensors (A_D), the total (normal) force measured by the entire principal surface of the IPM (F_{NT}) was expressed as,

$$F_{NT} = A_D D_D + \sum_{x=1}^{n} F_{Nx} \qquad \text{(with } n = 6\text{)} \tag{8}$$

This calculation of total force measured by the IPM was applied to all data, irrespective of which series of experiments the data originated from.

3.6.6.2. Classification of movements from conscious baboons responsible for maximum forces on IPM

Classifying different movements associated with the highest force amplitudes was difficult to obtain due to the high sampling rate of the data acquisition system and the large amount of data acquired. To facilitate the classification of movements, a peak detection filter was applied to the F_{NT} data which substantially reduced the F_{NT} data to local F_{NT} peak data.

For an explanation of the peak detection filter algorithm, consider three adjacent data points (data points 1, 2 and 3): If data point 1 was greater than data point 2 by more than the predefined threshold value, then data point 2 was positively identified as a peak. Thereafter data point 2 becomes the new data point 1, and data point 3 becomes the new data point 2, and so forth. A threshold value of 0.25 N was found to be suitably low to positively identify all peaks of interest. This peak detection filter automatically evaluated and identified peaks from the F_{NT} data.

By applying the peak detection filter to the F_{NT} data of the experiments on conscious baboons, the individual movements associated with the thirty highest extracted peak F_{NT} data points were

identified for each IPM. The peak detection filter excluded most peak data points caused by the same movement, thereby yielding separate movement events for classification. The availability of the synchronous video data made it possible to interactively classify these extracted F_{NT} peaks with associated movements. Due to the large variety of movements that the conscious baboon performed, the movements identified were classified into groups of movements.

The application of the peak detection filter for classification of movements was only performed on data obtained from the experiments on conscious baboons.

3.7. Interspecific transfer function concept for predicting *in vivo* forces on implanted pacemaker in humans

3.7.1. Proposed concept

To evaluate the total normal force on an implanted pacemaker (F_{NT}) in humans, a concept for an interspecific transfer function was proposed to enable estimation of the F_{NT} in humans by using the F_{NT} measured in baboons, as part of this feasibility study. The formulation of this concept involved using experimental data acquired from the baboons along with published information to relate the in F_{NT} experienced by the IPM implanted in baboons (input) to the F_{NT} experienced by a similar sized device implanted in humans (output). An indirect route was proposed to achieve this aim, which consisted of the following steps: Firstly, it was attempted to relate the different in-line muscle forces (F_{IL}) and morphometric parameters of the musculoskeletal structures surrounding the IPM to the F_{NT} in baboons. Secondly, it was assumed that this relationship was suitable for use in humans, i.e. the relationship between F_{IL} and morphometric parameters, and F_{NT} was assumed to be scale-invariant. The latter step implied that if this relationship for baboons indeed existed and shown to be suitable for use with human data, then it was possible to estimate the F_{NT} in humans. This proposed interspecific transfer function concept is presented in Figure 21.

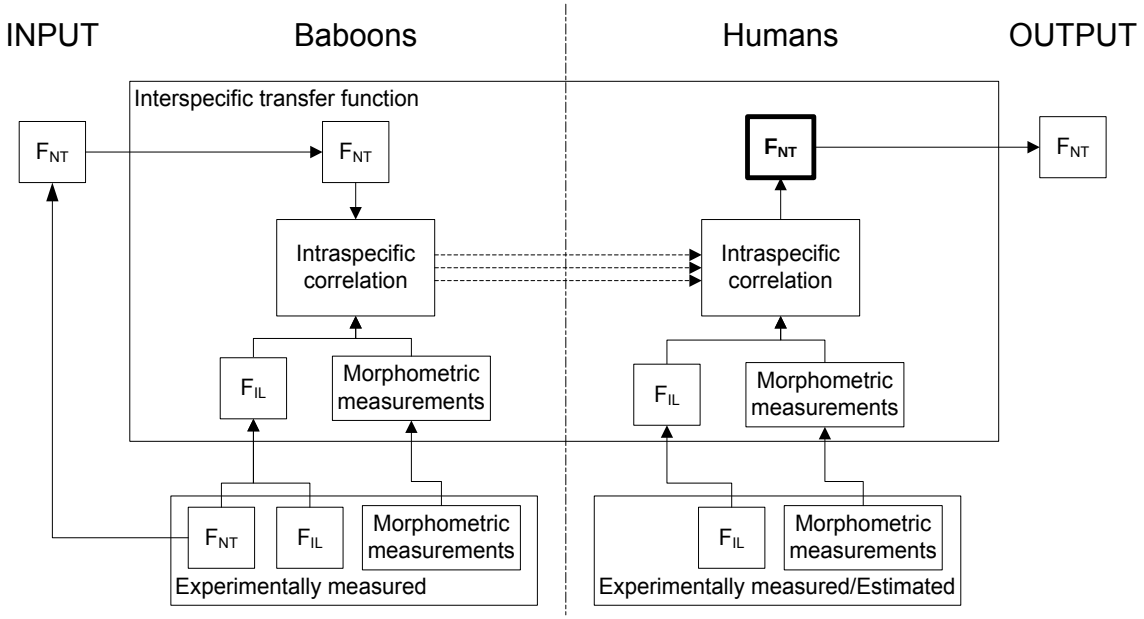

Figure 21: The proposed concept of the interspecific transfer function. This concept proposes using of the total force experienced by the IPM (F_{NT}) in baboons (input) to predict the F_{NT} in humans (output). It followed an indirect route involving relating the relevant muscle in-line force (F_{IL}) and morphometric parameters to the F_{NT}, as was measured in baboons. This relationship was then proposed to be suitable for use in humans.

Potential advantages of this approach were that if the F_{IL} and morphometric parameters for humans could be non-invasively measured or estimated, then this concept implied that similar tests (similar to those presented in this study) did not have to be performed on humans. Furthermore, if this relationship between F_{IL} and morphometric parameters, and F_{NT} was found to indeed be suitable and robust for humans, then there would be no need for any further animal experimentation.

This concept transfer function was formulated by utilizing the following:

- Experimental data obtained from baboon experiments;
    - Electrical stimulation (eStim) experiments (Section 3.3.4.3);
    - Morphometric measurements (Section 3.4)
- Analysis of data from baboon experiments;
    - Correlation of experimental parameters (Section 3.7.2);
- Relevant published information on intraspecific and interspecific differences (Section 2.5 and 2.6);
- Human data from the Visible Human Project's male specimen – i.e. the Virtual Human Male (VHM) (Spitzer et al. 1996; Garner et al. 2000).

The proposed analysis used to assist in formulating this concept of an interspecific transfer function is presented below.

3.7.2. Correlation of experimental parameters

The relationship (or correlation) that was expected to exist between the F_{NT} and F_{IL} and morphometric parameters was evaluated by means of linear regression analysis. The reason for using linear regression was due to its strength and accessibility in empirically evaluating the influence of multiple independent variables on a dependent variable. The analyses were performed by defining the F_{NT} as the output (response) and all other relevant parameters as input parameters (regressors). Since investigation of the correlation between these input and output parameters has not been done before, as far as the author is aware, different combinations of regressors were included in different analyses, with F_{NT} and ΔF_{NT} as responses, respectively. The regressors used in these analyses included the following morphometric measurements (Section 3.4): $t_{m,cb}$, $w_{m,IPM}$, $w_{m,cb}$, $\mathrm{L_m^{meas}}$, V_m, M_m.

Two additional parameters were also included as regressors, namely the physiological cross-sectional area of the muscle (PCSA) and the muscle stress (σ_m). These parameters were not directly measured during these experiments, but were derived from measured parameters and reported muscle data. The following simplified definitions of PCSA (Holzbaur et al. 2007) and σ_m were used:

$$PCSA = (Vol_m / L_m^{meas})(L_m / L_m^0) \tag{9}$$

$$\sigma_m = \frac{F_{IL}}{PCSA} \tag{10}$$

This definition of the PCSA differed from the one presented in Eq. (1), since it did not include the pennation angle (θ). The effect of the pennation angle on the PCSA, i.e. $\cos(\theta)$, was assumed to be equal to 1 and comparable for the same muscle of all the baboons considered. The ratio of muscle fibre length and the optimal muscle fibre length ($\mathrm{L_m / L_m^0}$) was assumed to be equal to one and also similar for the same muscle of all the baboons considered.

The reason for including the PCSA in the abovementioned regression analyses was due to the fact that it scaled proportionately with the peak isometric force that a muscle can produce ($\mathrm{F_m^0}$) (Section 2.6.3). The σ_m was included since it was a unique interpretable parameter that consisted of a muscle force as well as a morphometric parameter of the considered muscle.

4. *In vivo* mechanical loading conditions of instrumented pacemaker

4.1. Performance of data acquisition system

Activation (or "waking up") of the implanted IPMs was found to be successful and repeatable for all IPMs considered. It was possible to "wake-up" the implanted IPMs from transceiver distances of up to 3 m, with the baboon being in a metal cage, which was considered to be sub-optimal conditions for RF communication. The graphical user interface of the software developed for the data acquisition system also provided real-time visual feedback of signal quality. This made it possible to change the position of the transceiver to obtain optimal signal quality.

Performing a Fourier analysis on the IPM signal revealed that no distinct external sources of RF noise were present in the IPM data. The signal was of such a good quality that it was considered that most remnant noise present in the IPM data was sufficiently filtered out by applying the median filter (n = 7).

The interlacing of video data with the IPM data by the data acquisition software provided excellent synchronization these two data sets and enabled the identification of forces corresponding to movements.

4.2. Evaluation of the acquired force sensor data

4.2.1. Effect of preconditioning and experimental conditions on calibration curves

Immediately prior to implant, the IPMs were "woken up" and it was found that the zero-load offset sensor voltage, V_{Noff}, of all IPM sensors had significantly decreased compared to V_{Noff} measured during pre-implant preconditioning. Implantation was continued despite this presumed lost effect of the pre-implant preconditioning, since the sensors also underwent extended conditioning to experimental condition (loading and temperature) during the planned healing period. Furthermore, post-explant calibrations were planned to be performed immediately after explantation, which were much closer in terms of time to experimental data acquisition compared to the pre-implant calibrations.

A comparison of pre-implant and post-explant calibrations of the sensors of SN068 and SN069 yielded similar calibration curves for all sensors, as shown in Figure 22a. The calibrations of the sensors of SN074 and SN076 yielded the same similarities between different pre-implant and post-explant calibration curves, respectively. However, pre-implant calibration curves were dissimilar compared to corresponding post-explant calibration curves, as shown in Figure 22b. It is clear from this figure that these sensors yielded calibration curves with significantly smaller calibrated voltage ranges (ΔV_{Ncal}) during the post-explant calibrations.

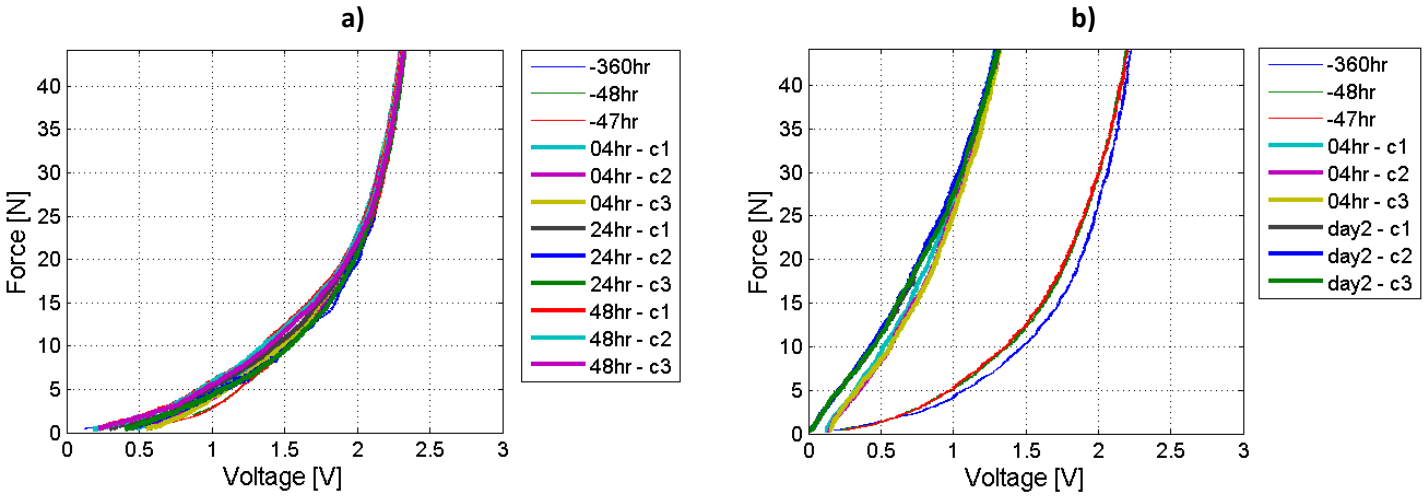

Figure 22: All pre-implant and post-explant calibration curves for two selected sensors illustrating, a) the comparable calibration curves for both pre-implant and post-explant (sensors of SN068 and SN069) b) comparable calibration curves for pre-implant and post-explant respectively, but not between pre-implant and post-explant calibration curves (sensors of SN074 and SN076).

From Figure 22a and Figure 22b it was observed that the characteristic drift due to changing experimental conditions, described by the assumptions of Section 3.2.1.1, occurred for all sensors during pre-implant and post-explant calibrations. This same characteristic drift also occurred for the sensors of SN074 and SN076, despite the difference between its pre-implant and post-explant calibration curves.

4.2.2. Choice of suitable calibration curves

The most suited post-explant calibration curves for each sensor of four IPMs used during the *in vivo* experiments, offset by V_{Noff} to start from the origin, are shown in Figure 23. This figure indicates the time point at which the calibration was performed relative to explantation (e.g. 04hr) and the calibration event (c1, c2 or c3). As previously explained, these calibration curves were chosen to best represent *in vivo* sensor behaviour during experiments. The choice was based on the calibration curve which had the smallest ΔV_{Ncal} throughout all post-explant calibration events (per sensor). Sensor specific calibration curves were evident, although a general non-linear trend was a characteristic trait of these sensors.

Evaluating 3rd, 4th and 5th degree polynomials to best approximate these most suited post-explant calibration curves, the 5th degree polynomial was found to yield the best approximation. Using the 5th degree polynomial, the "goodness of fit" for each calibration curve resulted in an average coefficient of determination (R^2) > 0.995, and an RMS error < 0.85, for n > 5900.

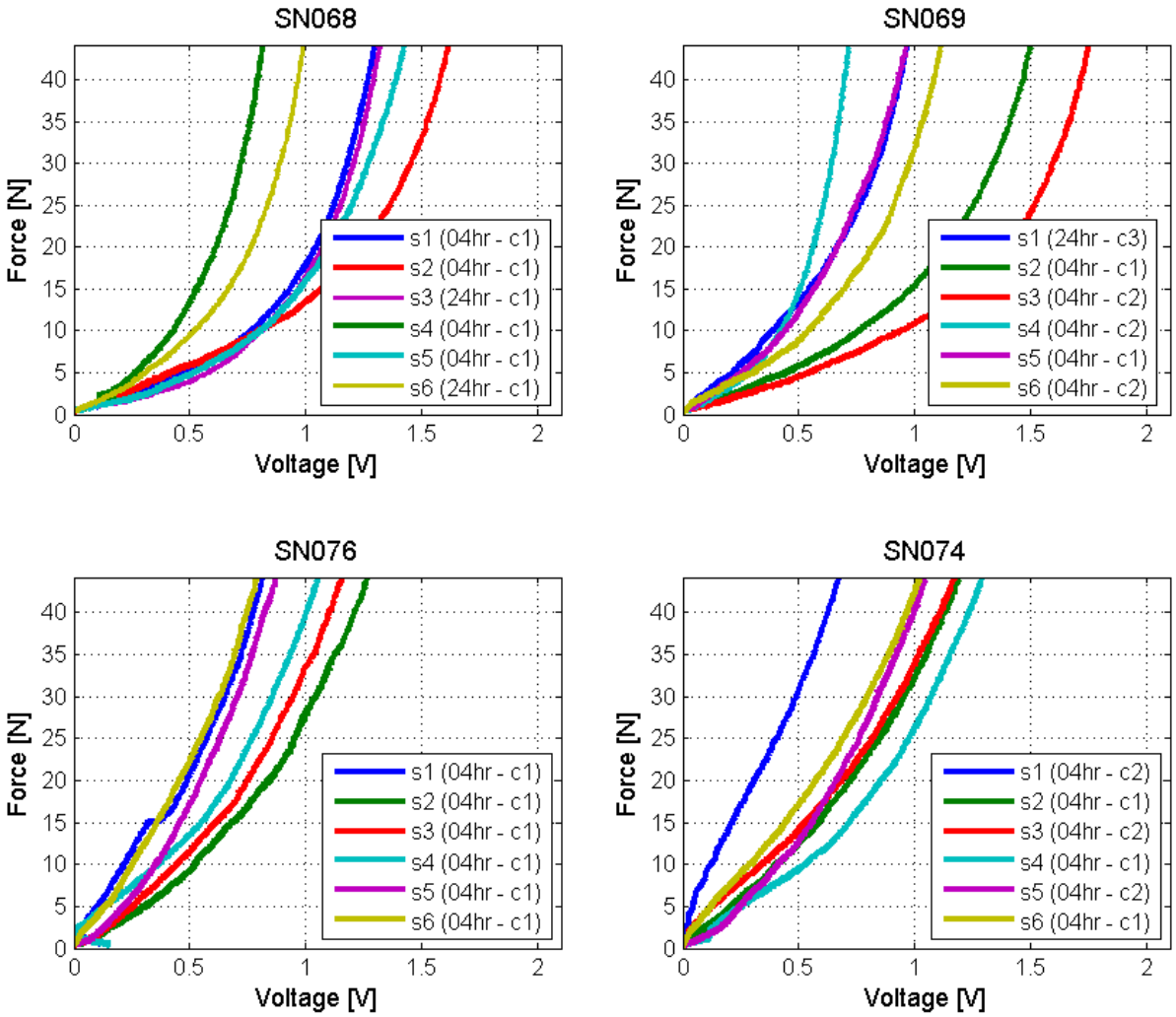

Figure 23: The most suited post-explant calibration curves chosen for each sensor of these four IPMs, i.e. SN068, SN069, SN076 and SN074, showing the sensor specificity of the calibration curves.

4.2.3. Ranges and observed trends of the force sensor data for evaluating conversion of sensor voltage to sensor force

Typical examples of the sensor voltage (V_N) ranges acquired for all sensors per series of experiments are shown in Figure 24, which also shows the corresponding calibrated voltage range of the most suited post-explant calibration curve (PE ΔV_{Ncal}). These plots revealed that sensors mostly experienced forces within their calibrated voltage range per series of experiments. The few exceptions that did occur were during the experiments on conscious baboons (a single sensor of both SN069 and SN076), during the 76 mm Chatillon experiments (a single sensor of SN068) and during the 12 mm Chatillon experiments (a single sensor of both SN068 and SN074, and four sensors of SN069). The percentile values indicated in this figure also revealed the range in which 95% of all sensor data was located (for experiments on conscious baboons, n > 720 000; for each set of experiments on anaesthetized baboons, n > 41 000).

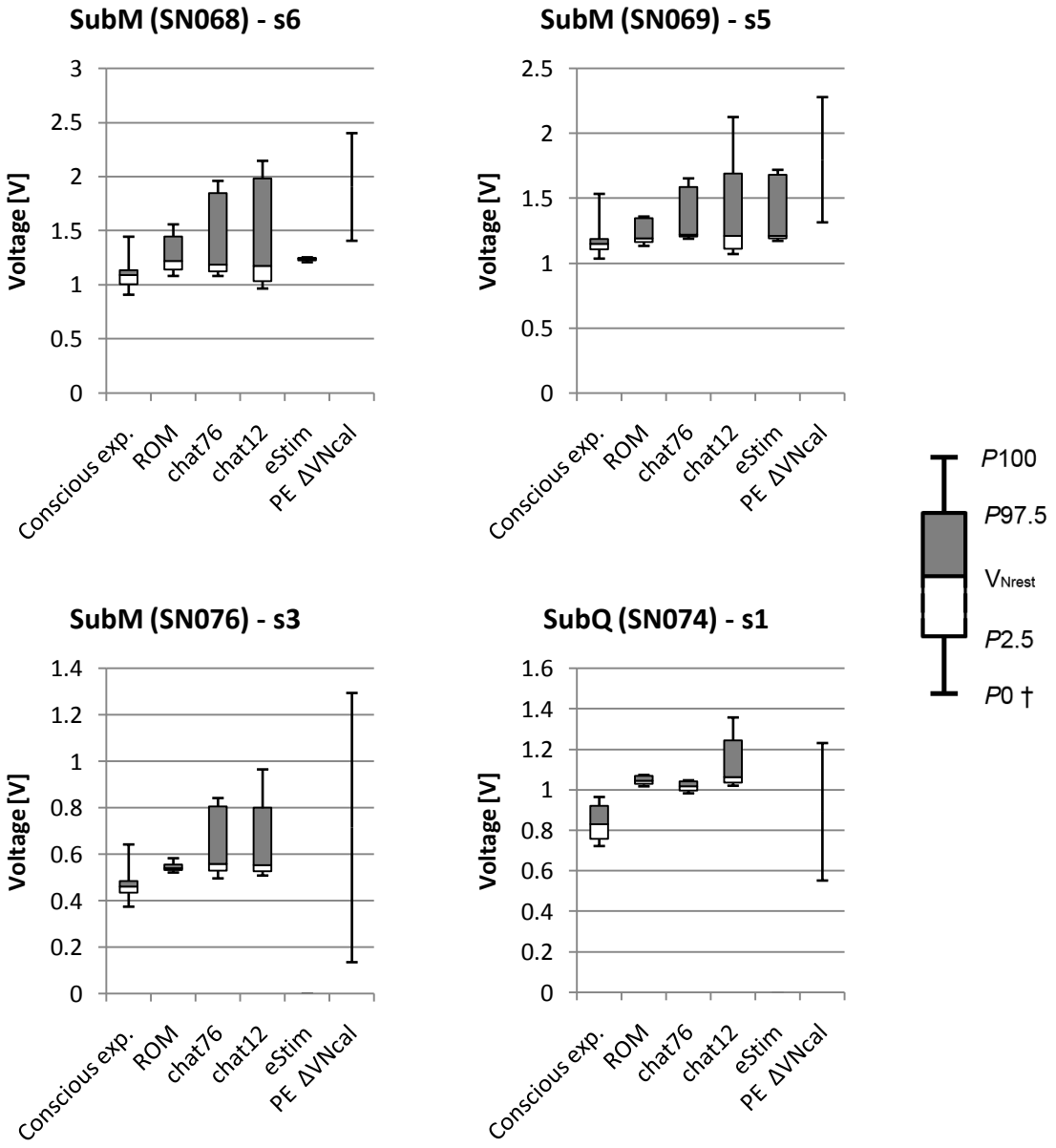

† For all *in vivo* experiments, *P*0 = V_{Nvmin}; For post-explant calibrations, *P*0 = V_{Noff}

Figure 24: Box plots of selected sensors showing the typical force sensor voltage (V_N) ranges acquired from the most suited post-explant calibration curves (PE ΔV_{Ncal}) and different series of in vivo experiments. The box plots indicate percentile values of sensor data combined for a complete series of experiments. The resting voltage indicated (V_{Nrest}) was averaged per series of experiments. No eStim experiments were performed for SN074 and SN076 (Section 4.8).

Another observation from this figure was the decrease in resting sensor voltage measured by each sensor for SN074 and SN076 from being implanted to being explanted (i.e. comparing values between chat12 and PE ΔV_{Ncal}). This resting sensor voltage was V_{Nrest} for the *in vivo* experiments and V_{Noff} for the post-explant calibrations. Although the V_{Noff} of the sensors of SN068 and SN069 progressively decreased over time during post-explant calibrations (Figure 22b), V_{Noff} for the sensors of SN074 and SN076 were observed to have decreased comparatively more over time during post-explant calibrations (Figure 22a).

Despite the comparatively greater decrease from V_{Nrest} to V_{Noff} for the sensors of SN074 and SN076, a similar trend and magnitude in the change of ΔV_{Ncal} was observed for the calibration curves of all sensors in the subsequent post-explant calibration curves, as shown in Figure 25. Considering all 6 sensors of each IPM, the normalized standard variation of ΔV_{Ncal} per time point was 1.4 ± 1%, 3.1 ± 2.1%, 2.7 ± 6% and 0.8 ± 0.3% (mean ± std) for SN068, SN069, SN076 and SN074, respectively.

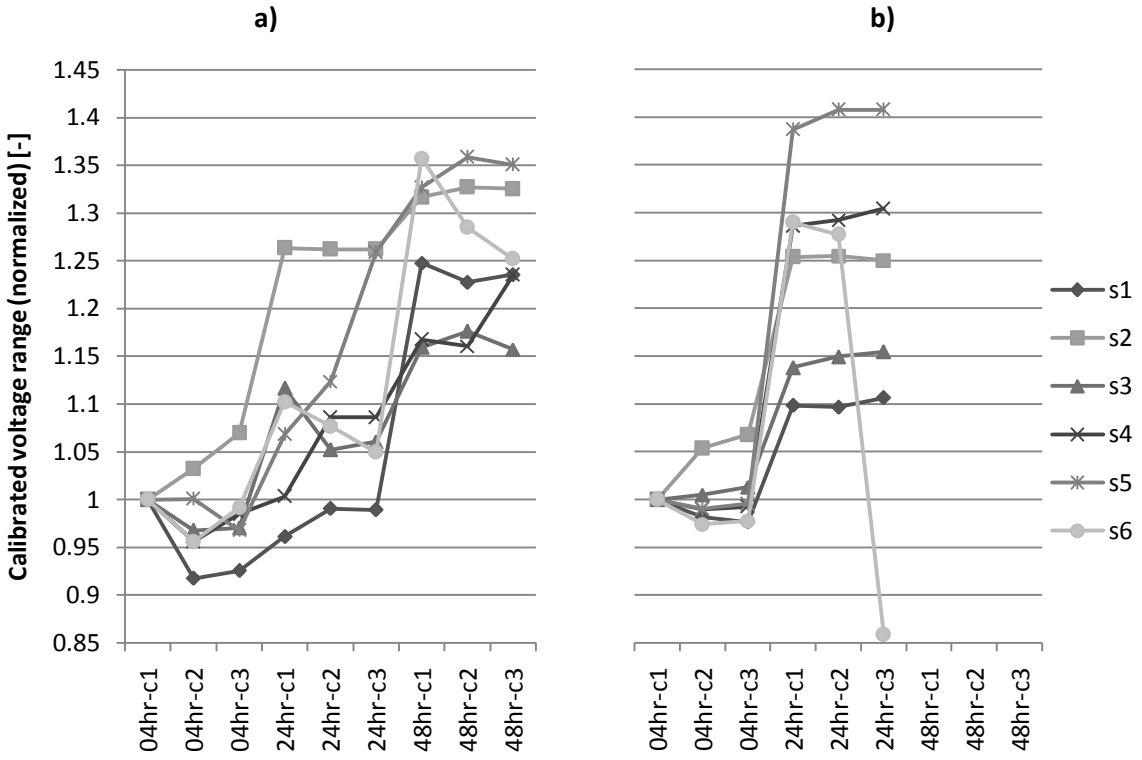

Figure 25: Change in calibrated voltage range (ΔV_{Ncal}) of each sensor during subsequent post-explant calibrations, normalized to the first calibration event. Examples are shown of sensors assembled on the IPM according to different methods a) SN069 (standard sensor assembly) and b) SN076 (non-standard sensor assembly).

The variation of V_{Nrest} within a series of experiments was found to be low, as revealed in the standard deviation shown Figure 26a and Figure 26b for from each series of experiments. The variation of V_{Nvmin} observed in these figures was a direct result of the variation of V_{Nrest}, since V_{Nrest} was used to determine V_{Nvmin} (Eq. (23)). These graphs also show the typical distinct and consistent trend with which V_{Nrest} increased over subsequent series of experiments. Furthermore, the V_{Nvmin} displayed a comparatively steeper and less consistent upward trend compared to the V_{Nrest} as also shown in this figure. The trend of V_{Nvmin} was typically to rise from the experiments on conscious baboons to ROM, vary between ROM, 76 mm and 12 mm Chatillon experiments, and finally rise to eStim experiments to a higher level than was recorded for the ROM experiments.

Since V_{Nrest} was used as the reference measurement parameter for the voltage-force conversion method, its variation was of particular interest. Consider that the only expected permanent change in resting force on the IPMs was when the "state" of the *pectoralis major* muscle changed. These different "states" of the *pectoralis major* were defined as: the muscle of the conscious baboon (experiments on conscious baboon), the muscle of the anaesthetized baboon (ROM, 76 mm and 12

mm Chatillon experiments) and the exposed muscle (eStim experiments). Therefore, the V_{Nrest} data from each experiment was further combined according to the expected "state" of the *pectoralis major*, in order to observe the variability of V_{Nrest} for each expected permanent change in resting force. The normalized V_{Nrest} and its variability during each of these "states" are shown in Figure 26c and Figure 26d.

The normalized standard deviation per "state" of the baboon, for all sensors of each IPMs, is shown below in Table 4. When considering these measurements, also note the time that elapsed for each series of experiment and the time between the different series of experiments (Section 3.3.1).

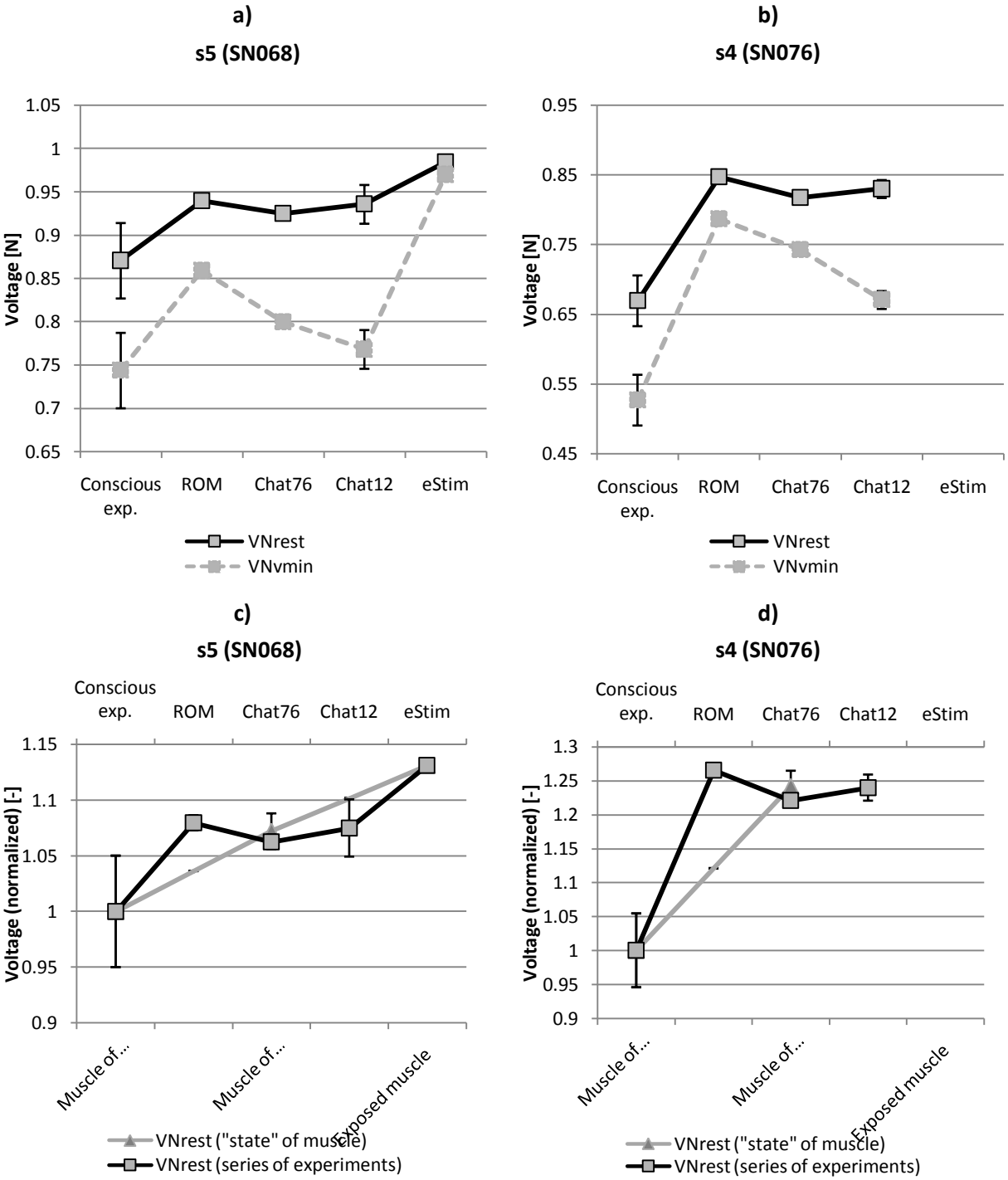

Figure 26: Typical examples of the mean and standard deviation of the resting sensor voltage (V_{Nrest}) and the valid minimum sensor voltage (V_{Nvmin}) for a sensor over all the in vivo experiments, showing a) & b) the V_{Nrest} and V_{Nvmin} per series of experiment for sensor 5 of SN068 and sensor 4 of SN076; and c) & d) the normalized V_{Nrest} for each series of experiment, as well as for each "state" of the muscle. It can be seen that the muscle of the anaesthetized baboon is the same for ROM, chat76 and chat12 experiments. All series of experiments displayed in the time order in which it occurred. Error bars not visible were too small to show up on this graph. Normalization to the mean value obtained from the experiments on conscious baboons. No eStim experiments performed for SN076 (and SN074).

Table 4: Normalized values of the resting sensor voltage (V_{Nrest}) (mean ± std) of all 6 sensors per IPM, for different "states" of the muscle overlying the IPM (pectoralis major). No eStim experiments performed for SN076 (and SN074).

"State" of *pectoralis major*	**SN068**	**SN069**	**SN076**	**SN074**
Muscle of conscious baboon	4.1 ± 2.9%	3.8 ± 4%	3.9 ± 1.6%	4.7 ± 2.1%
Muscle of anaesthetized baboons	1.8 ± 0.8%	3.5 ± 3.5%	2.7 ± 1%	4.3 ± 2.7%
Exposed muscle	0.7 ± 1.2%	2 ± 2.8%	-	-

4.3. Healing of implants and histology of device encapsulation

Two of the IPMs implanted in the subQ position, SN064 and SN071, had to be prematurely explanted in week 3 and week 6 post-implantation, respectively, due to insufficient wound healing. The insufficient wound healing was ascribed to one or more of the following factors, i.e. the incision directly overlying the implanted IPM, increased skin tension due to the foreign body causing vasoconstriction (impairing the healing process) and a mattress type suture used to close the incisions which did not facilitate proper anastomosis of opposing ends of the incised skin. Both baboons that had the IPMs prematurely explanted, healed without any further complications. After sufficient healing of the implants, the baboons were transferred to a common animal holding facility of the South African Medical Research Council at Delft.

Upon explantation of the IPMs, the subM IPMs (SN068, SN069 and SN076) were found to have been completely encapsulated by a distinct fibrotic capsule, which completely covered the IPM. These capsules were found to fit over the IPMs like gloves, and had to be removed by incising the capsule. Upon making the first incision in the fibrotic capsule to retrieve the IPM, the capsule did not split open as would be observed for a pre-tensed capsule wall, i.e. negligible pocket-wall tension. Easy removal of the IPM from its capsule was attributed to a smooth and moist inner surface of the fibrotic capsule. The subQ IPM (SN074) was found not to have been enveloped by a distinct fibrotic capsule, although upon explantation, the device was also tightly enveloped by the surrounding tissue, i.e. partial encapsulation. No parts of the fibrotic capsule or other surrounding tissue bonded to the medical grade epoxy or the titanium sensor cover plates which made up the outer surface of the IPMs.

Histological analysis of the tissue samples containing fibrotic capsule and adjacent muscle tissue were performed and yielded similar results for all three subM IPMs: The H & E stained samples displayed the proliferation of cells of the fibrotic capsule adjacent to the muscle tissue. The CD68 stained samples displayed the immunoglobulins present on the outer edge of the fibrotic capsule. Although no further histological analyses were performed, these findings were considered to be typical of a fibrous capsule that formed as result of the normal physiological immune response to an implanted foreign body.

4.4. Morphometric measurements

The morphometric measurements shown in Table 5 were obtained following the eStim experiments (Section 4.8), hence the reference to the buckle crossbar of the buckle strain transducer. An expanded version of this table and additional force data from the *in vivo* experiment are attached in Appendix B. Furthermore, all pectoral measurements were performed with the IPM still *in situ*, except for the mass and volume of the *pectoralis major* muscle (M_m and V_m).

Table 5: Morphometric measurements of test subjects are shown, together with relevant implant and explant information. Muscle parameters presented are for the pectoralis major muscle specifically.

Baboon #	447		449		575	
Explant mass [kg]	24.7		23		20.7	
Implant position	SubM	SubQ	SubQ	SubM	SubM	SubQ
IPM device #	SN068	SN064*	SN071*	SN069	SN076†	SN074†
M_m [g]$	82.0	154.0	166.0	125.0	149.0	164.0
V_m [cm3]$	70.0	135.0	150.0	120.0	135.0	140.0
ρ_m [g/cm^3]‡	1.171	1.141	1.107	1.042	1.104	1.171
L_m^{meas} **[mm]**	150.0	150.0	180.0	170.0	195.0	170.0
$w_{m,IPM}$ [mm]	92.5	95.0	80.0	90.0	85.0	95.0
$w_{m,cb}$ [mm]	42.5	60.0	50.0	47.5	5.0	52.5
$t_{m,cb}$ [mm]	5.0	4.0	6.5	4.0	4.5	3.5
PCSA [cm^2]**	7.7	14.8	13.7	11.6	11.4	13.5

*Prematurely explanted
†No data obtained due to equipment malfunction
$For whole *pectoralis major* muscle (combined clavicular, sternal and ribs portions)
‡ For $\rho_m = M_m/V_m$
**For $L_m/L_m^0 = 1$ (see Eq. (9))

The pectoral musculature of post-mortem test subjects (Chacma baboons) from a previous study performed at the Cardiovascular Research Unit was evaluated. A superficial investigation revealed similar structures of the *pectoralis major* and *pectoralis minor* muscles to humans. The *pectoralis minor* muscle, however, appeared to be relatively more developed in baboons than in humans.

The muscle overlying and underlying the IPM was identified as the *pectoralis major* muscle and the *pectoralis minor* muscle respectively. It was found that the portion of the *pectoralis major* muscle overlying the IPM, which was isolated for electrical stimulation, was indeed the sternal portion of the *pectoralis major* muscle (*pec major* (sternum)) – similar to what was reported for humans (Section 3.4). The *pec major* (sternum) was also found to have completely covered all subM IPMs *in situ,* i.e. wide enough to completely cover the IPM. Furthermore, each of the three subM IPMs rested completely on the well developed *pectoralis minor* of the baboons.

Differences in the M_m and V_m were clearly observed between implant sites that had an IPM in the subM or in the subQ position. The M_m and V_m associated with the subM IPM had smaller values compared to the M_m and V_m associated with the subQ IPM.

Previously used IPMs were explanted and replaced with non-functional IPMs for capturing thoracic MRI and CT images. These images were obtained for only two of the three baboons, i.e. 447 and 575. Corresponding images for humans were obtained from the visible human male VHM data set. Selected cross-sectional views were extracted from the baboon and the VHM data, as shown in Figure 27. Both axial and sagittal cross-sections were extracted to indicate the location of the IPM relative to the musculoskeletal structures. As a rough indication of the differences in pectoral geometry between a baboon and a human, anterior-posterior and lateral measurements were obtained in the axial view, as indicated. The position of an IPM in the VHM was estimated and

indicated in this figure according to previously defined descriptions of subM implant locations in humans (Brinker et al. 2005).

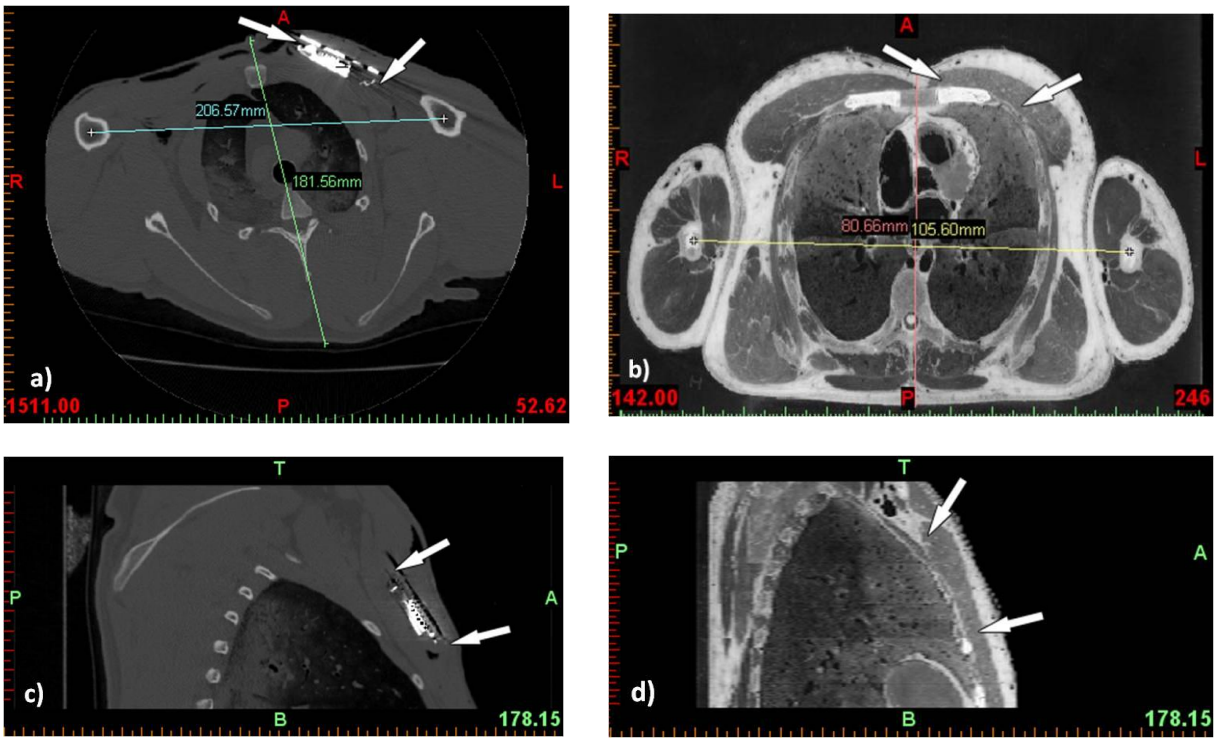

Figure 27: Cross sectional views of the pectoral region of the baboon and human (Virtual Human Male data set - (Spitzer et al. 1996)), showing the axial section at the middle of the sternum, indicating anterior-posterior (front-to-back) and lateral (femur-to-femur) distances of a) baboon and b) human. The corresponding sagittal section at medial third of the clavicle is also shown for c) baboon and d) human. Note that axial distances between humans and baboons were not according to same scale, however only the ratio of measurements were needed. The position of the non-functional IPM implanted for imaging purposes is indicated with the white arrows. Although the human data did not include an implanted pacemaker, the location of one was estimated and indicated accordingly.

Considering the axial cross sectional distances, shown in Figure 27, the ratio of the lateral to the anterior-posterior distance was found to be 15% greater for the baboon compared to the human. This rough measurement indicated that the chest curvature on the level of a pectoral implanted cardiac pacemaker was smaller for humans than for baboons, i.e. humans have flatter chests.

A 3D segmented representation of where the subM IPM was located relative to surrounding skeletal structures was also obtained from the CT data, as shown in Figure 28.

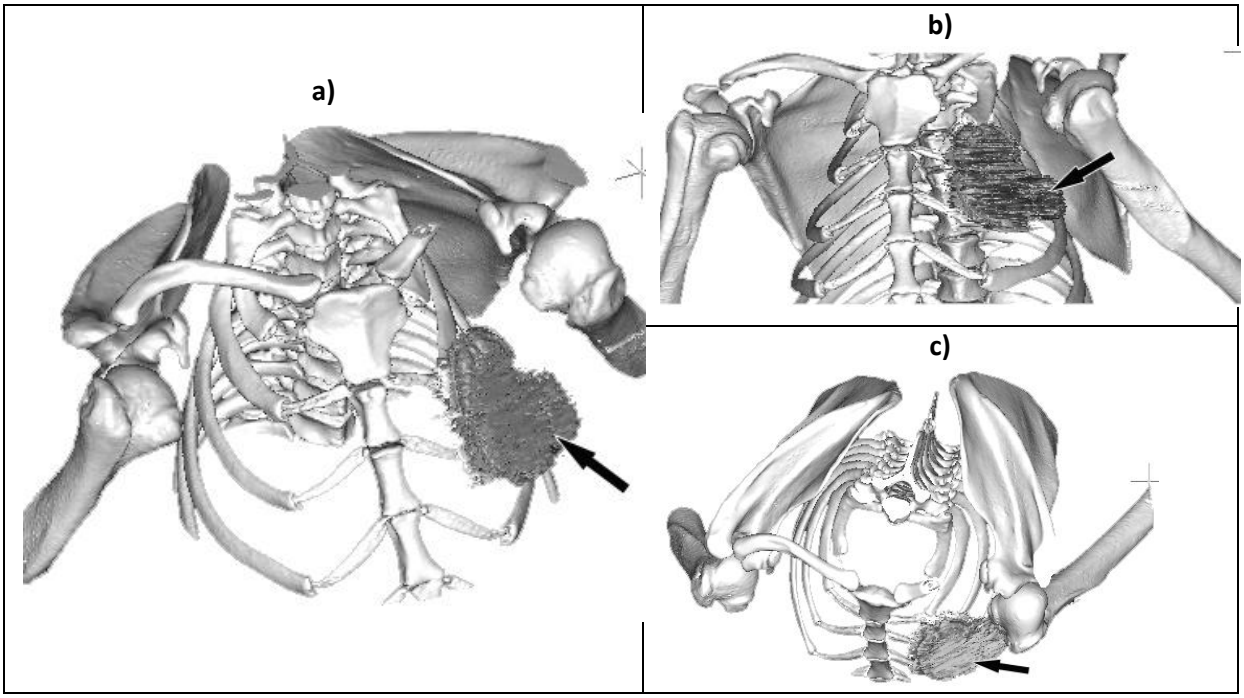

Figure 28: Position of IPM relative to surrounding skeletal structures for the baboon, indicated by a black arrow. Different views are presented and included a) an isometric view, b) a frontal view and c) a top view. Imaging artefacts present in the CT data were responsible for the bad resolution of the IPM compared to the skeletal structures.

4.5. *In vivo* loading during conscious activities of baboons

Typical total normal force (F_{NT}) data obtained from an IPM during an experiment on a conscious baboon are shown in Figure 29.

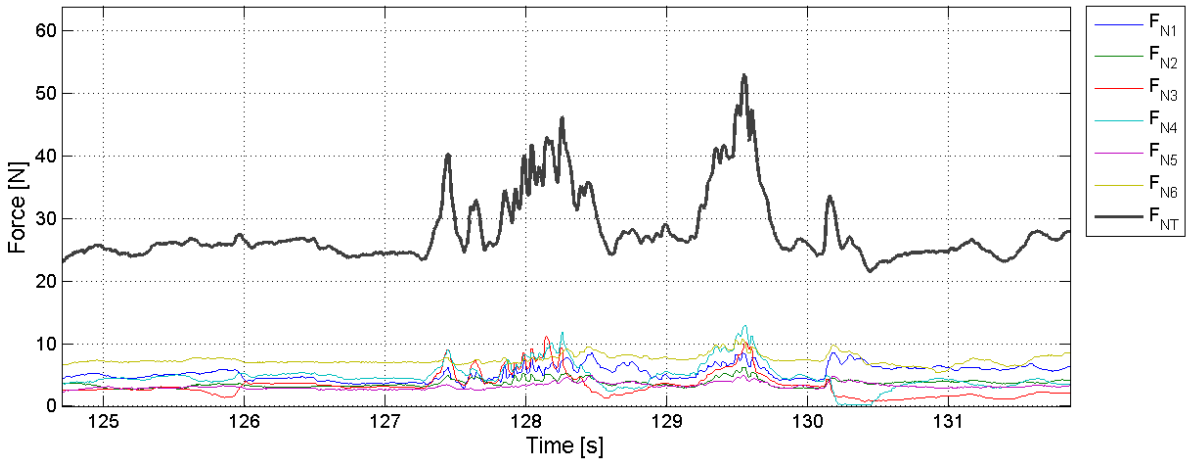

Figure 29: A typical example of the total normal force (F_{NT}) over time plot from the experiments on conscious baboons. This plot shows both the individual force sensor measurements (F_{Nx}) and the total force exerted on the IPM (F_{NT}).

The combination of the F_{NT} data from all experiments within the series, for each IPM, is presented in Figure 30. The normalized histograms revealed that the distribution of the F_{NT} data points of the subM IPMs displayed a more gradual decreasing tail to the right, when compared to the subQ IPM. The maximum F_{NT} data points indicated in this box plot were confirmed by synchronous video recording to have been caused by a physical movement.

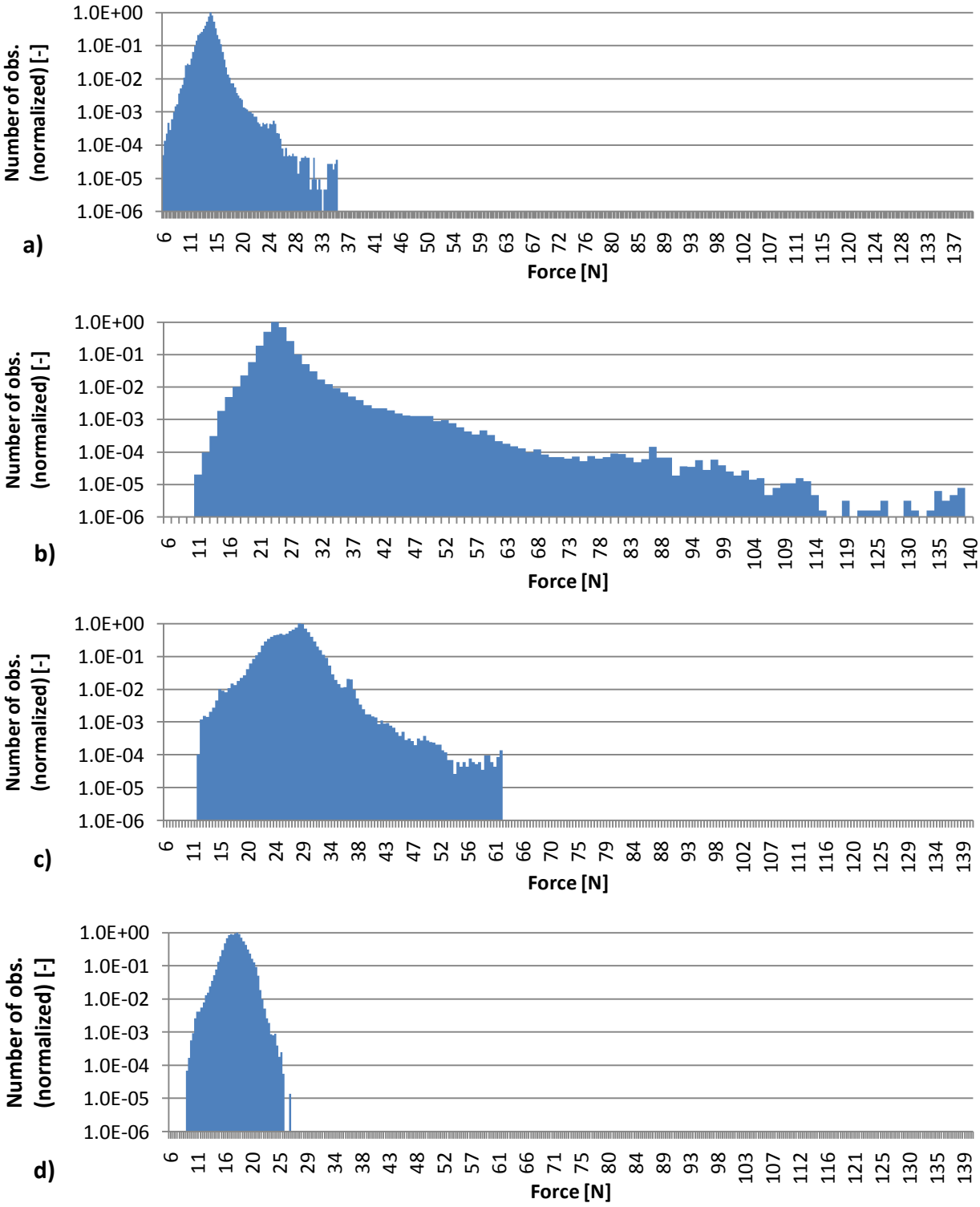

Figure 30: Histograms of the total normal force (F_{NT}) data points measured by IPMs during the experiments on conscious baboons, with normalized number of observations shown in a logarithmic scale. Data is shown for a) SN068 (subM), b) SN069 (subM), c) SN076 (subM) and d) SN074 (subQ). The maximum total normal force (F_{NTmax}) shown for each IPM was confirmed by synchronous video recordings.

A comparison of the total force events measured by each IPM is presented in the box plot of Figure 31. Similar to Figure 30, it confirmed the maximum F_{NT} values displayed for each IPM. Both Figure 30

and Figure 31 shows that no clear distinction was observed between the F_{NT} magnitudes measured by the subM IPMs compared to that of the subQ IPM.

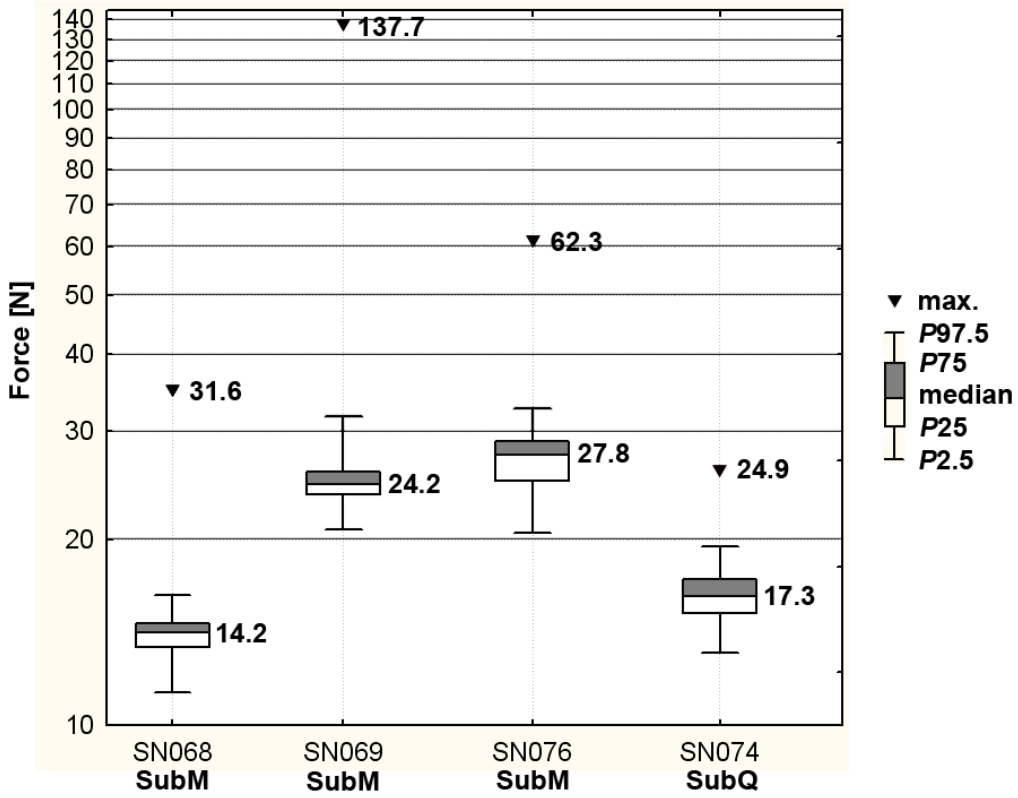

Figure 31: Box plot comparing all F_{NT} data points amongst different IPMs (with n > 720 000 for each IPM)

Information about the experiments performed and a summary of force data obtained during these experiments are attached in Appendix B. Data from this table showed that F_{NTmax} did not follow the same trend as the F_{NTrest}, which was ascribed to the fact that the values of F_{NTmax} were obtained from uncontrolled (though confirmed through synchronous video footage) physical activities. The ratio between the F_{NTmax} and the F_{NTrest} for the subM IPMs was 2.2, 5.8 and 2.2, compared to 1.4 for the subQ IPM.

The individual movements, associated with the thirty highest peak values of F_{NT}, were classified into the following groups of movements:

- Pushing – including pulling the cage walls, weight bearing and landing directly on the arms when jumping down from its perched surface in the cage;
- Pulling – including pulling the cage walls and pulling the chain of a foraging log;
- Stretching – including movements such as adduction, abduction and raising of the arm whilst not holding onto any surrounding structures;
- Striking – consisted of fast strikes of the arm (not necessarily hitting the cage walls);
- Unknown – judging by response of the sensors and visible part of baboon's body, definitely the result of an action performed by the baboon, although unclassifiable.

Averaging the ratio of the maximum forces (F_{NT} peaks) and the resting force (F_{NTrest}) within each group of movements is shown in Figure 32. This figure indicated that the maximum F_{NT} peaks for

different types of movements were comparable per IPM, i.e. different movements produced similar forces on the IPM relative to its resting force. Furthermore, Figure 32 also indicated that the maximum force experienced by the subQ IPM relative to its resting force was smaller when compared to the subM devices. This result was similar to that reflected in the bar plot of Figure 31 above.

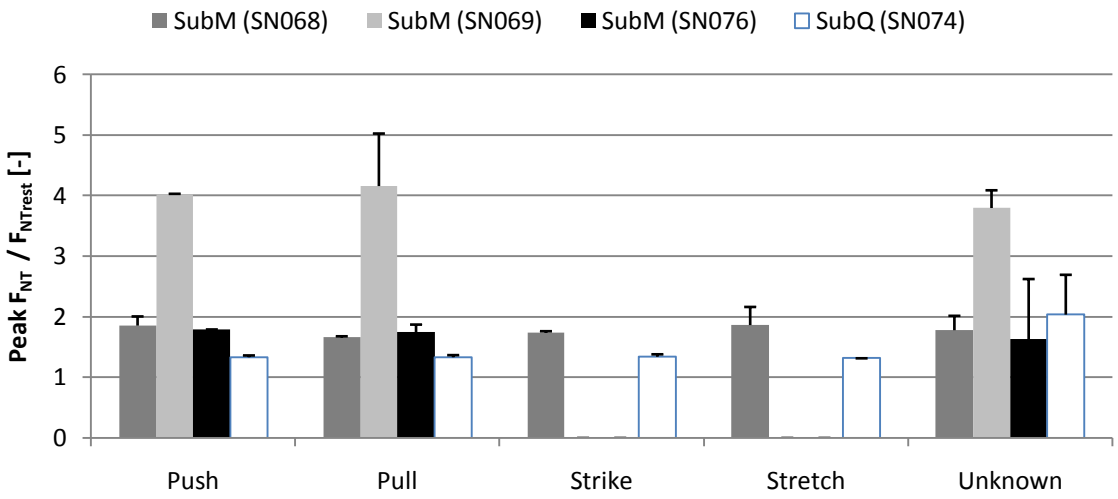

Figure 32: The peak force (F_{NT}) relative to the resting force (F_{NTrest}) of physical actions associated with the 30 maximum force peaks measured during experiments on conscious baboons. Certain movements in certain of the baboons did not yield F_{NT} peaks which fell into the top 30 peaks, which is clear from the data shown.

4.6. Range of motion experiments on anaesthetized baboons

The F_{NT} data obtained from force measurement ROM were evaluated for observable local peaks caused by different induced movements of the upper arm and extracted accordingly, as shown in Figure 33. These peaks were interactively classified only according to upper arm position from the synchronous video data. The peak data was the only information extracted from the IPM data during the ROM experiments, because the maximum loading of the IPM was of interest. The F_{NT} signal acquired clearly showed that the movement of the baboon arm by the operator was not always consistent, which was also confirmed by the synchronous video recordings.

The F_{NT} data for all peaks extracted from the ROM series of experiments for different positions of the upper arm are presented in Figure 34.

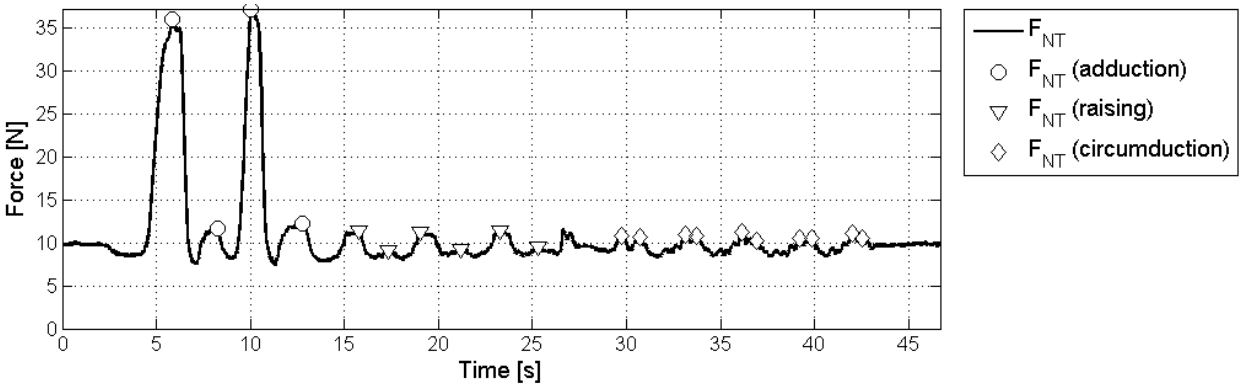

Figure 33: A typical example of the total normal force (F_{NT}) versus time plot from the force measurement ROM experiments, showing the extracted peaks of F_{NT} data. This figure shows the peaks classified for the adduction and abduction (circles), elevation and lowering (triangles) and circumduction (diamonds) movements.

a)

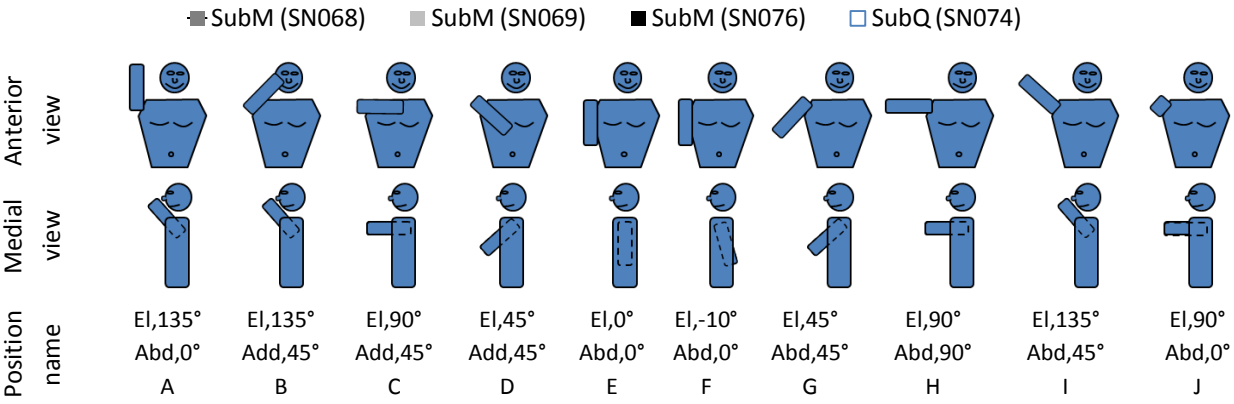

b)

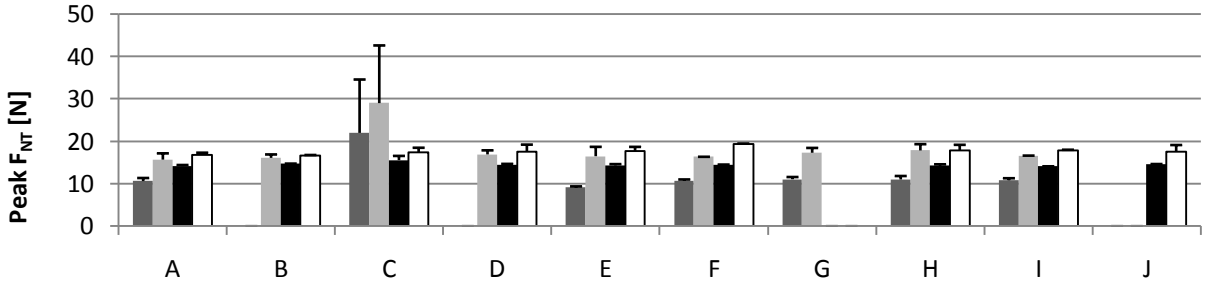

c)

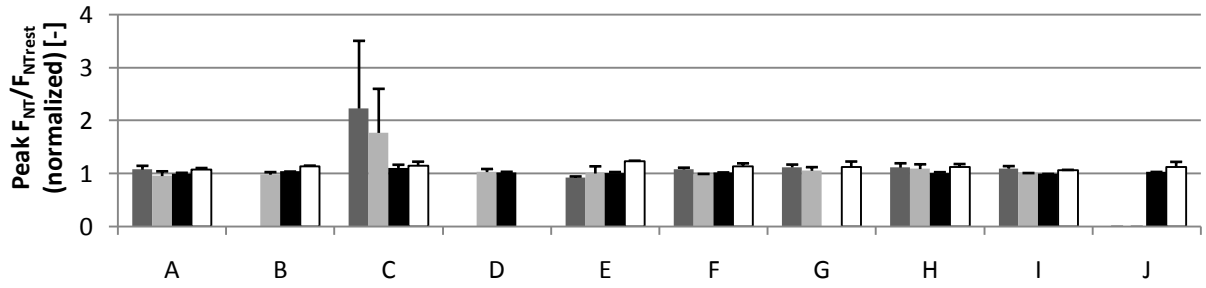

Figure 34: Total normal force (F_{NT}) produced by different positions of the upper arm during force measurement ROM experiments showing a) the identified positions of the upper arm for the anterior and medial views (A-J), b) the extracted peak total normal forces (Peak F_{NT}) (mean ± std) and c) the normalized peak force (F_{NT}) relative to the resting force (F_{NTrest}) (mean ± std).

Except for the F_{NT} peaks produced by the adducted upper arm (position C), no distinct difference was observed between the IPMs implanted in the subM or the subQ positions. Normalizing the F_{NT} peaks to F_{NTrest} in each position revealed values for each IPM (whether subM or subQ) which were similar and did not considerably exceed 1, as indicated in Figure 34.

Comparatively higher F_{NT} peaks were recorded when the upper arm was adducted (position C), as shown in Figure 34. The F_{NT} peak measured with the upper arm in this position included a component of force exerted by the overlying arm. This component of force was not exerted on the IPMs with the arm in any other position. This greater variation between the F_{NT} peaks for different IPMs was ascribed to experimental variation due to the arm being physically pressed onto the chest by an operator, who was not controlling the compression caused by the arm to the chest.

The F_{NTrest} was recorded with the upper arm in position F, since this was the resting position during the experiments on the anaesthetized baboon. This position of the arm was the result of the considerable thickness (anterior-posterior) of the chest of a Chacma baboon (Figure 27). From Figure 34 it can be seen that the arm in this position actually yielded F_{NT} peaks similar to other arm positions considered.

A summary of force data obtained during these experiments are attached in Appendix B. Data from this table also showed how close F_{NTmax} was to F_{NTrest} for different positions of the arm for each IPM individually. The ratio between the F_{NTmax} and F_{NTrest} for the subM IPMs was 4.0, 2.9 and 1.2, compared to 1.3 for the subQ IPM. Keeping in mind that the forces on the IPM were uncontrolled, these ratios did not correspond at all to the ratios obtained in the experiments on conscious baboons.

The most evident finding from visual inspection of the fluoroscopy ROM recordings was that the movement of the IPM was confined by surrounding structures, which therefore caused it to move along with its surrounding structures. This finding was in agreement with the fibrotic capsule found around the subM IPM upon explantation. This capsule fitted tightly over the IPM and was fused (attached) to the overlying and underlying structures, i.e. removal of the capsule required it to be excised. Although no complete fibrotic capsule was found around the subQ IPM, it was also tightly enveloped by the overlying skin and underlying muscle. Therefore the orientation and position of the IPM relative to the ribcage changed during movement of the arm.

An observation pertaining to the peak forces measured during adduction (position C of Figure 34) was that the IPM was in one of two different positions relative to surrounding musculoskeletal structures. The IPM was either compressed by the overlying upper arm, or the IPM was displaced medially (i.e. rolled out) as seen in Figure 35. This difference of IPM position during adduction was not identified in the abovementioned force measurement ROM experiments.

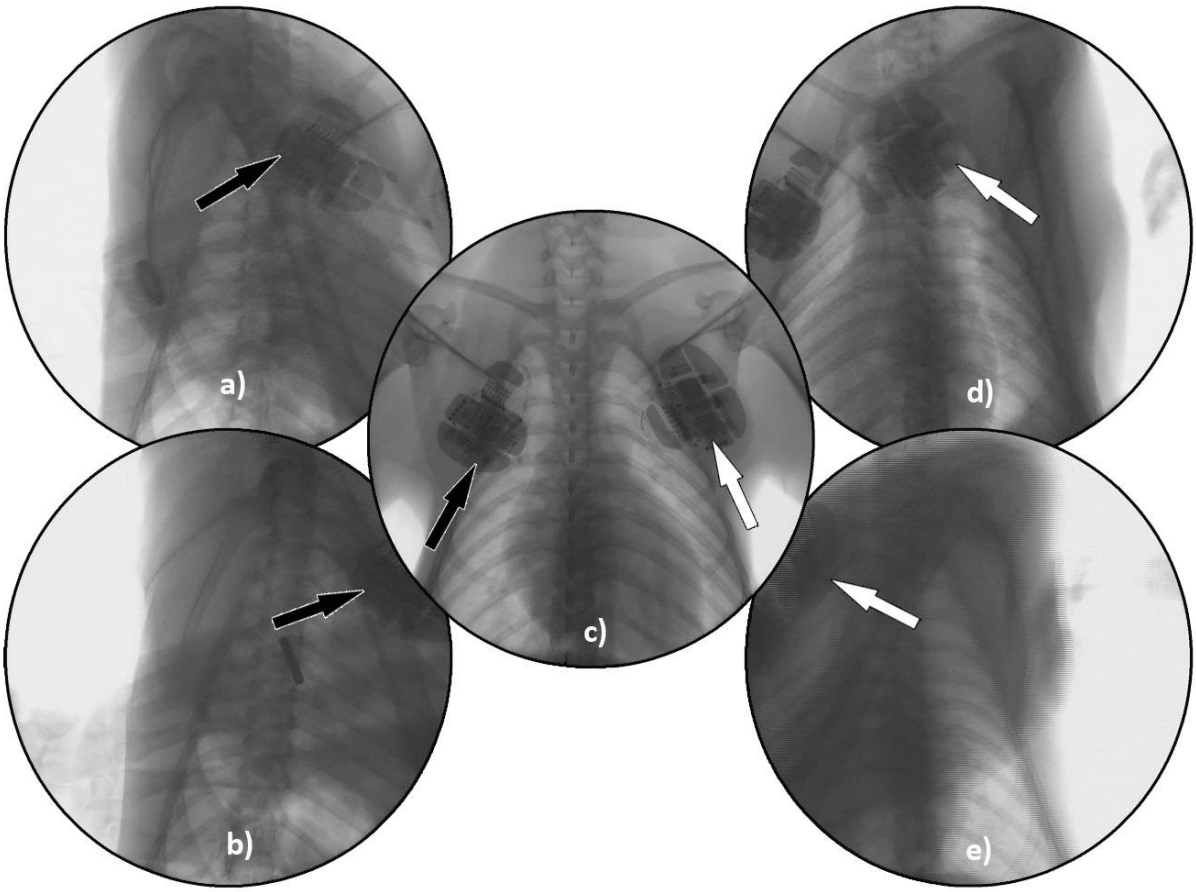

Figure 35: Different positions of the IPM relative to surrounding musculoskeletal structures during adduction as observed in the fluoroscopy ROM experiments. These images show anterior-posterior fluoroscopy taken of the chest of baboon #575. The position of the femur and the considered IPM are shown for a) & b) adduction causing "sandwich" compressive force on (subM – black arrow) IPM, c) the baboon at rest and d) & e) adduction causing "rolled out" compressive force on (subQ – white arrow) IPM.

4.7. Manual external compression experiments on anaesthetized baboons

The repeated forces applied by the Chatillon digital force gauge with a Ø76 mm endplate over the implanted IPM produced the 76 mm Chatillon force data (F_{chat76}) and IPM total force data (F_{NT}) of the 76 mm Chatillon series of experiments. From this data, corresponding peaks were extracted interactively for each IPM, as shown in Figure 36a. Similarly, the repeated forces applied by the Chatillon digital force gauge with a Ø12 mm endplate over a specific sensor of the implanted IPM, produced the 12 mm Chatillon force data F_{chat12} and F_{Nx} data (x = 1, 2, 3, 4, 5 and 6) of the 12 mm Chatillon series of experiments. From this data, corresponding local peaks were also interactively extracted as shown in Figure 36b. These figures show the excellent responsiveness of the IPM force sensors *in vivo.*

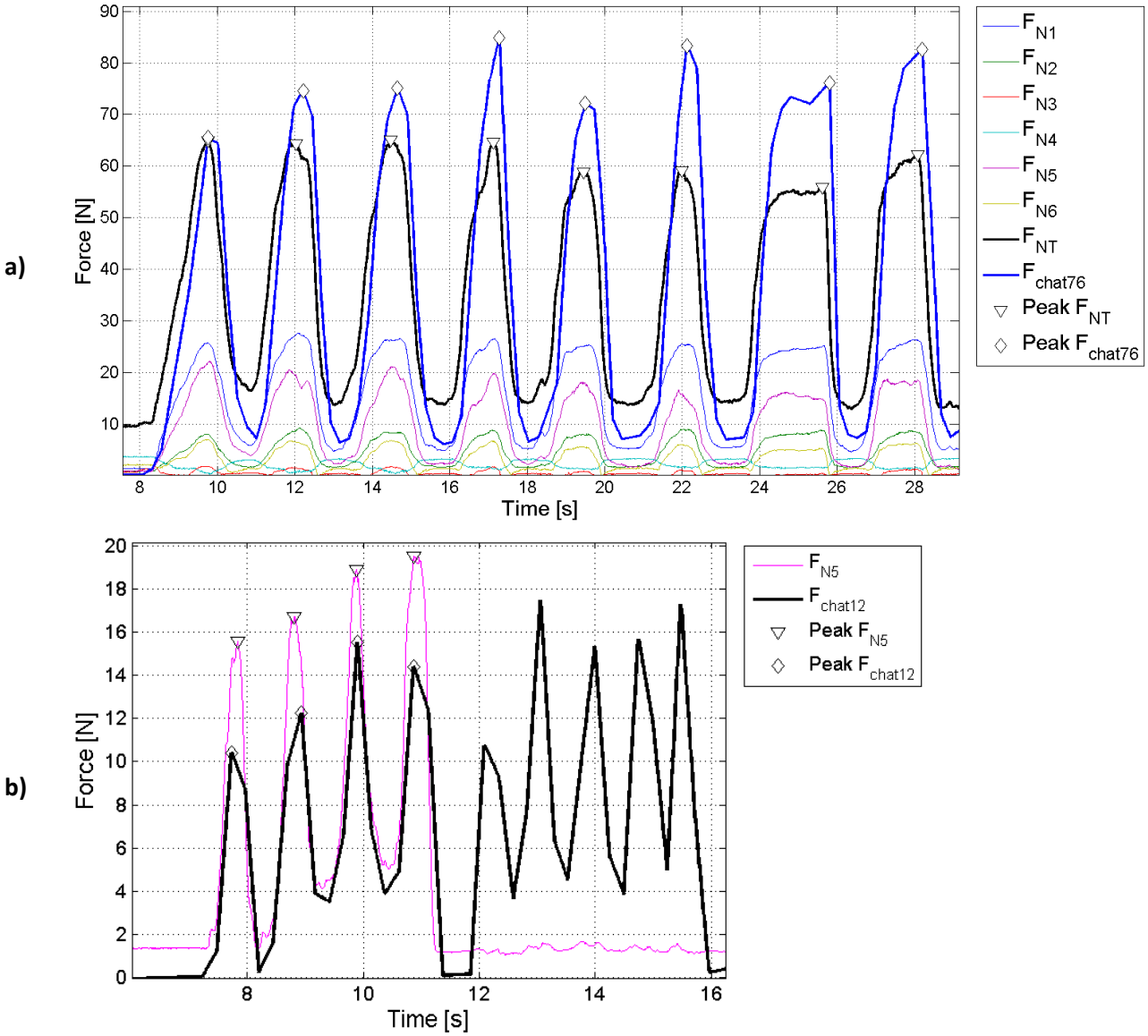

Figure 36: Typical examples of manual external compression experiments (76 mm Chatillon and 12 mm Chatillon) showing: a) the force applied by the Chatillon digital force gauge with a 76 mm endplate (F_{chat76}) and the measured total normal force (ΔF_{NT}) plotted against time; and b) the force applied by the Chatillon digital force gauge with a 12 mm endplate (Fchat12) and the measured sensor normal force (ΔF_{Nx}) plotted against time. Both these graphs show peaks extracted from the Chatillon force data and corresponding IPM data.

Although both the F_{chat76} and F_{chat12} was measured during experiments, the force amplitude was not controlled (compressions with the Chatillon was performed by an operator). The magnitude of F_{chat76} varied between 25 and 90 N, while the magnitude of F_{chat12} varied between 5 and 40 N for different repetitions of force application.

The comparative force measurements of the 76 mm Chatillon experiments for each IPM are shown in Figure 37. This figure shows the ratio of the ΔF_{NT} and the F_{chat76} of corresponding peaks that were extracted.

Due to the unknown dissipation of F_{chat76} by the overlying and underlying tissue and the inability to confirm the position of the endplate relative to the sensors, the expectation was to obtain $0 < (\Delta F_{NT}/F_{chat76}) < 1$. This was however not the case for two of the IPMs: Firstly, the negative ratio values

shown for SN074 meant that negative ΔF_{NT} values measured for positive values of F_{chat76}. Secondly, the ratio values shown for SN068 that were larger than one meant that measured values of ΔF_{NT} that were larger than the applied values of F_{chat76}. Both of these occurrences were obviously not physically possible with the measurement system described.

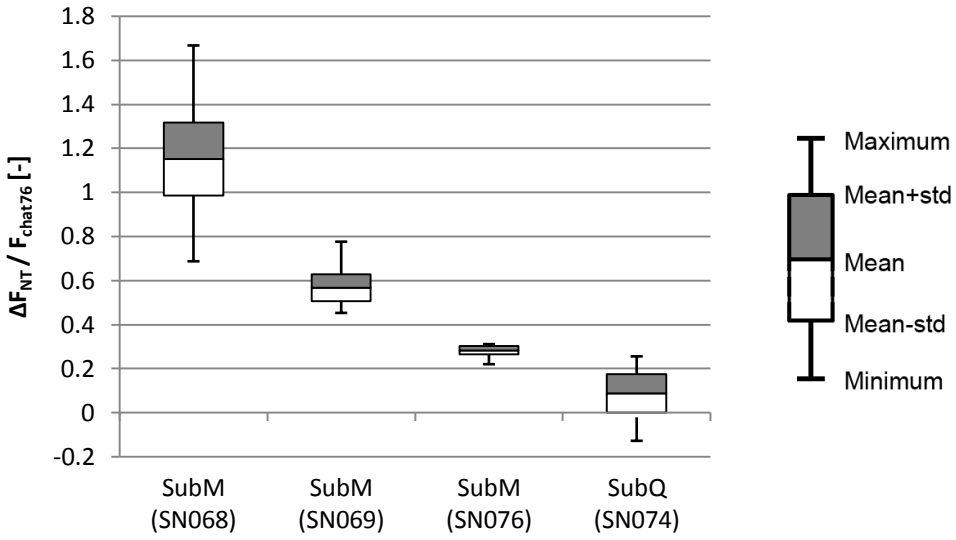

Figure 37: Box plots showing the ratio of the change of total normal force measured by the IPM (ΔF_{NT}) and the force applied by the Chatillon with the 76 mm endplate (F_{chat76}) for each IPM. Each data point used for these box plots was the ratio between corresponding ΔF_{NT} and F_{chat76} extracted during the 76 mm Chatillon experiments.

Due to the difficulties of estimating the exact location of the sensor *in vivo* with a 12 mm applicator (i.e. IPM located underneath a layer of tissue), not all applications F_{chat12} resulted in a clear F_{NT} response signal. These force peak amplitudes in the F_{chat12} data that clearly caused a positive change in force measurement on two or more of the sensors were excluded from the analysis, i.e. when a force was applied on two or more sensors simultaneously. Furthermore, if less than two corresponding pairs of peaks ($n < 2$) were extractable from the all available F_{Nx} data, the data from the particular sensor were also excluded from the analysis. Meeting these two conditions meant that some sensors were excluded from this analysis.

The comparative force measurements of the 12 mm Chatillon experiments for each sensor of each IPM are shown in Figure 38. This figure shows the ratio of the ΔF_{Nx} and the F_{chat12} of corresponding peaks that were extracted (with x representing the sensor number, i.e. x = 1, 2, 3, 4, 5 or 6).

Due to the unknown dissipation of F_{chat12} by the overlying and underlying tissue and the inability to confirm the position of the endplate relative to the sensors, the expectation was to obtain $0 < (\Delta F_{Nx}/F_{chat12}) < 1$, for x = 1, 2, 3, 4, 5 and 6. This was however not the case for a number of sensors: The ratio values that were larger than one meant that measured values of ΔF_{NT} that were larger than the applied values of F_{chat76}. These occurrences were obviously not physically possible with the measurement system described.

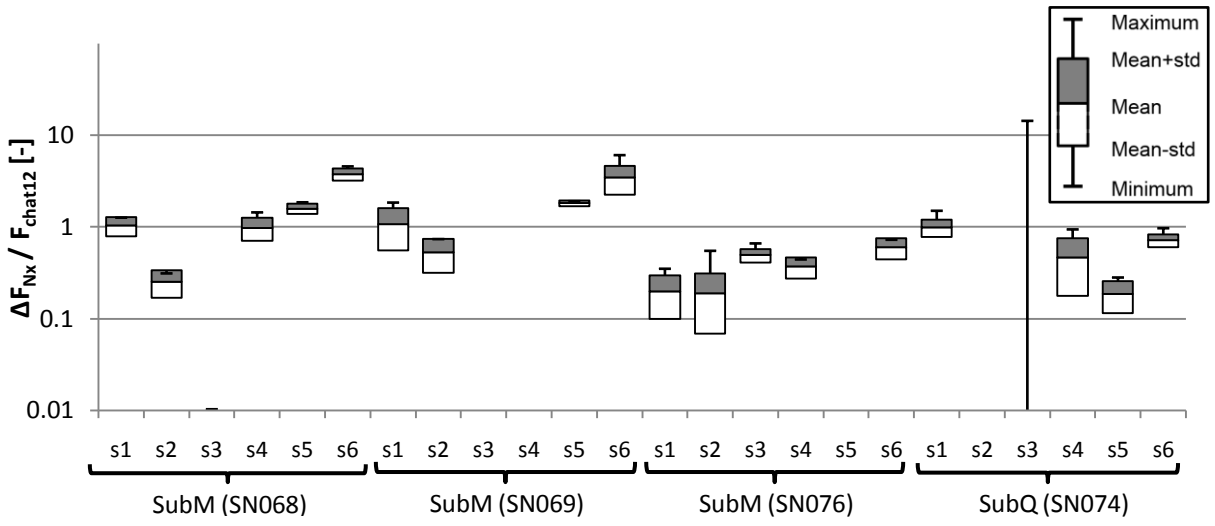

Figure 38: Box plots showing the ratio of the change of total normal force measured by the IPM (ΔF_{NT}) and the force applied by the Chatillon with the 12 mm endplate (F_{chat12}) for each IPM. Each data point used for these box plots was the ratio between corresponding ΔF_{NT} and F_{chat12} extracted during the 12 mm Chatillon experiments. No sufficient extractable data was available for certain sensors and hence the corresponding box plots were omitted. Data from s3 of SN074 yielded negative values over a wide range – only the upper range fell within the specified scale.

A summary of forces measured during these 76 mm Chatillon and 12 mm Chatillon experiments are attached in Appendix B.

4.8. Electrical stimulation experiments on anaesthetized baboons

The eStim experiments were performed bilaterally on the *pec major* (sternum) of baboons 447 and 449. Each of these baboons had one chronically implanted subM IPM, i.e. SN068 and SN069 respectively. Each baboon also received a temporarily implanted subM IPM on the alternative side of the chronically implanted IPM, which used to contain the subQ IPM that was prematurely explanted. The same IPM, SN066, was implanted in both baboons, as explained previously. The IPM implanted in baboon 449 was referred to as SN066.1, and implanted in baboon 447, as SN066.2. The muscle overlying the IPM, *pec major* (sternum), completely covered the principal surface of each of the IPMs considered in these experiments.

The eStim signal, applied to the *pec major* (sternum) yielded the typical in-line muscle force (F_{IL}) and total force on the IPM (F_{NT}) measurements shown in Figure 39. The highest peak F_{IL} and corresponding F_{NT} were extracted for each experiment. The F_{IL} and F_{NT} measurements were not synchronized, which caused the observed time lag of ±0.5 s between these two signals. The combination of the low resolution (≅0.01 V) and the high calibration conversion factor (Eq. **(6)**) of the buckle strain transducer yielded a force measurement resolution of 4.7 N.

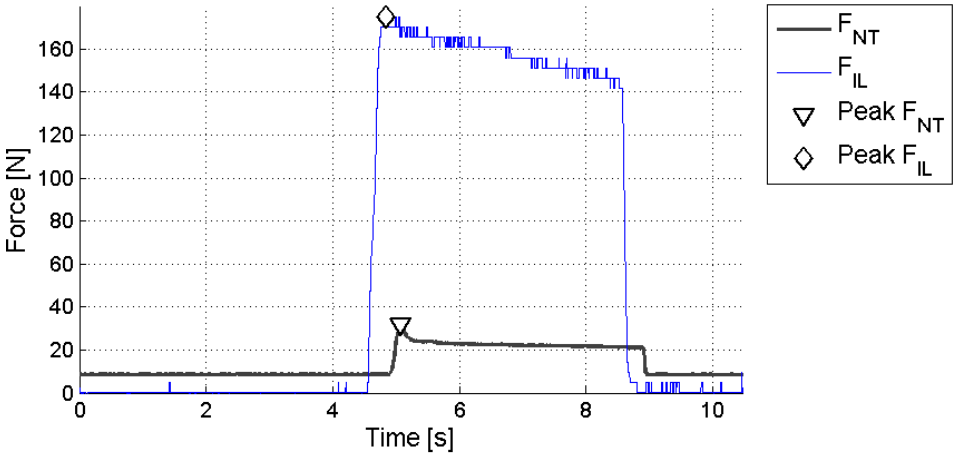

Figure 39: A typical example of a response from an electrically stimulated muscle, showing the peaks extracted from the in-line muscle force (F_{IL}) and total force on the IPM (F_{NT}) data.

The order in which the different amplitudes of eStim current were applied, plotted against the peak F_{IL} produced, yielded the results shown in Figure 40. This figure clearly showed that the maximum eStim amplitude did not necessarily result in the maximum F_{IL}.

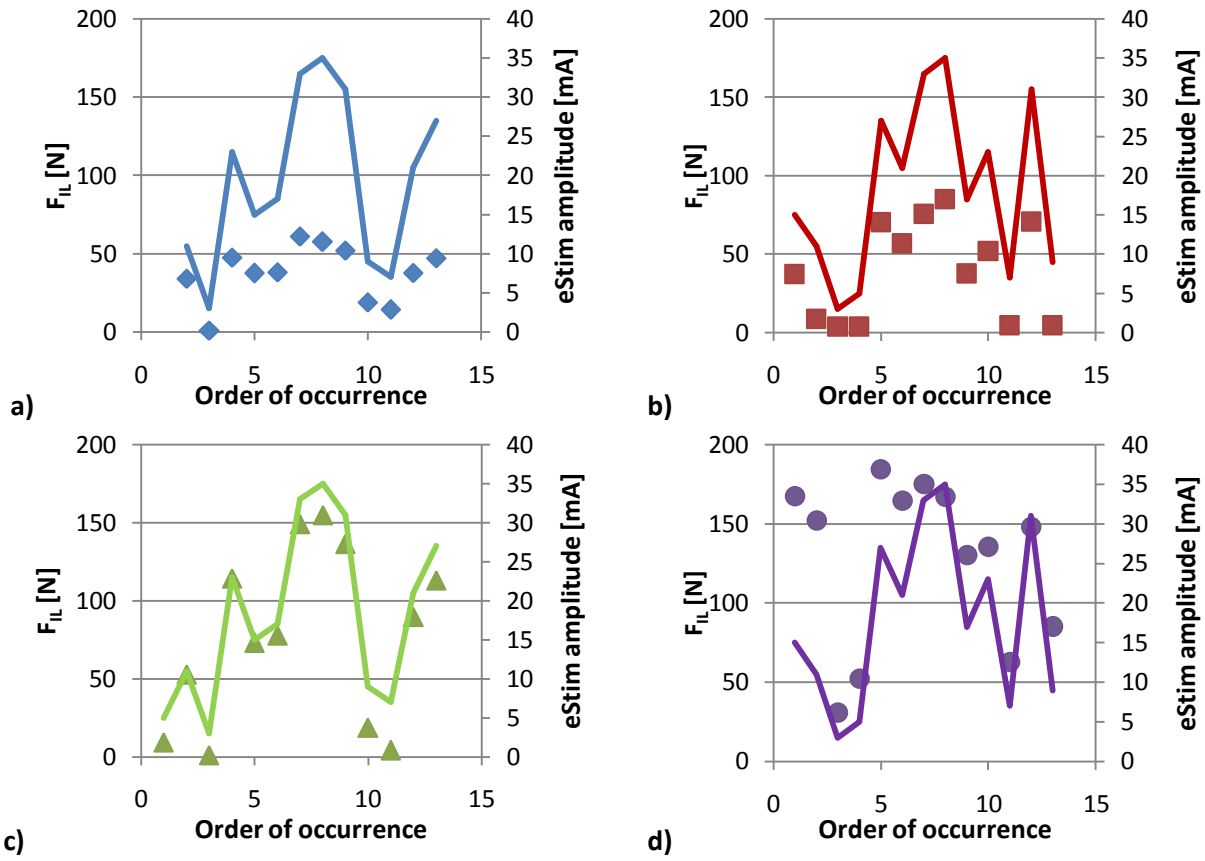

Figure 40: The in-line muscle force (F_{IL}) produced by corresponding eStim current amplitude, in the order as they occurred experimentally, showing results of: a) SN068 (chronic implant), b) SN069 (chronic implant), c) SN066.1 (acute implant) and d) SN066.2 (acute implant). The scattered data points indicate maximum F_{IL} developed for the corresponding discrete eStim amplitude levels, indicated by the solid line.

The corresponding peak values of F_{IL} and F_{NT} extracted from these experiments for each IPM are shown in Figure 41.

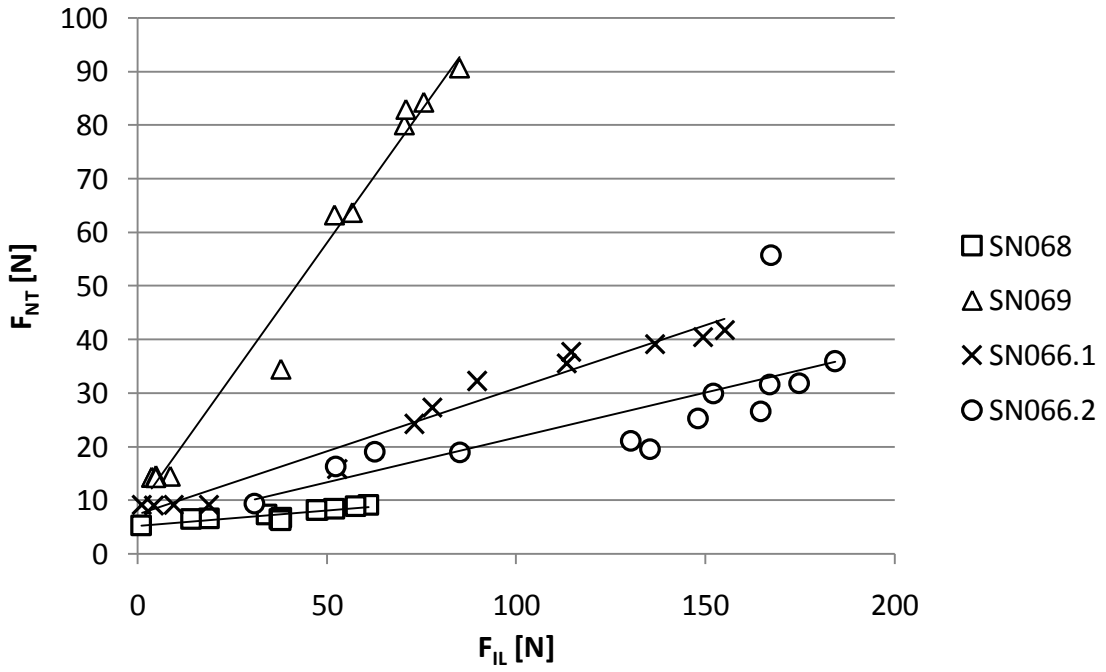

Figure 41: Force responses of in-line muscle force (F_{IL}) and corresponding total force on the IPM (F_{NT}), caused by electrical stimulation of the pec major (sternum) muscle overlying the IPM. Simple linear regression yielded the trendlines plotted for each IPM.

Performing simple linear regression (SLR) analyses on the extracted F_{IL} and corresponding F_{NT} peaks of each IPM resulted in R^2 values of 0.80, 0.96, 0.97 and 0.56 for SN068, SN069, SN066.1 and SN066.2, respectively. All of these correlations were shown to be significant ($p < 0.05$). The difference in the slope of the linear trend lines fitted through the data points of each IPM showed that the correlation between F_{NT} and F_{IL} was specific to each test subject – i.e. subject-specific.

4.9. Sensor interaction and transient response

Irregularities in force measurements obtained from the chat12 experiments prompted investigation into the cause of these irregularities, i.e. $F_N > F_{chat12}$ of Figure 38. Upon closer inspection of the data from the chat12 experiments, the possibility of interaction between sensors of the same IPM was first identified. Sensor interaction was defined as the change in sensor voltage response (V_N) because of force exerted on a different sensor on the same principal surface of the IPM. This change in V_N therefore caused V_N data of a sensor that were unrepresentative of the actual forces exerted upon it. This presumed sensor interaction was clearly observed in the V_N response during the chat12 experiments and also during calibration events, as shown in Figure 42.

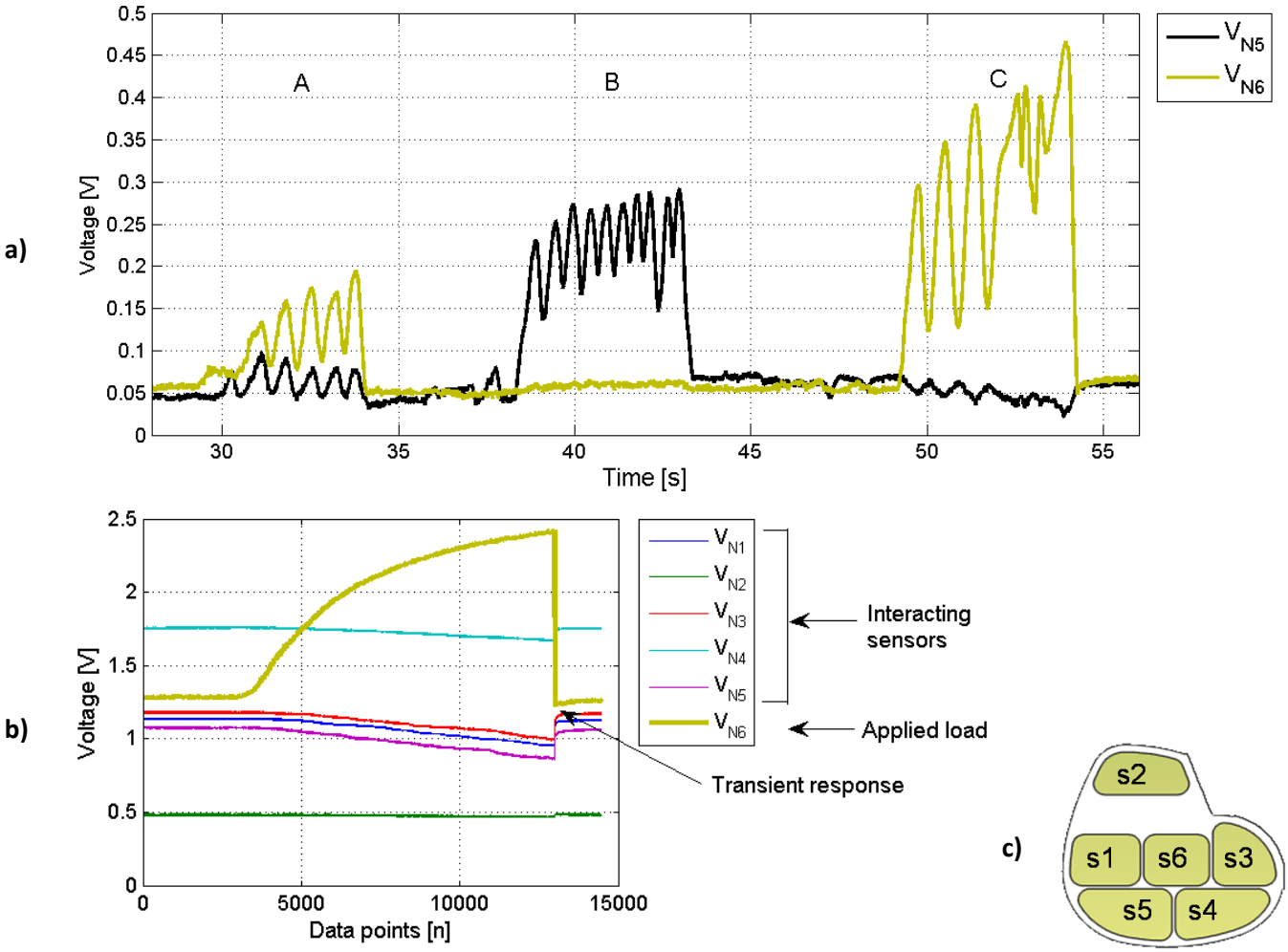

Figure 42: Examples of sensor interaction and transient response showing, a) chat12 experiments: sensor voltage (V_N) response of sensors 5 and 6 showing simultaneous measurement of force (A) and sensor interaction (C) respectively and b) post-explant calibration event: sensor voltage (V_N) response of all sensors clearly showing the sensor being calibrated and the measurements induced by sensor interaction. The transient response of sensor voltage was also clearly observed when the calibration load was released. c) Diagram indicating location of the sensors on the IPM.

Both of these examples of figure clearly show a sensor response that ideally should not have occurred. The chat12 experiment of Figure 42a depicted two different occurrences: Firstly, the repeated applications of compressive force (F_{chat12}) with both sensors responding with corresponding increases of V_{N5} and V_{N6}. This was interpreted as F_{chat12} applied to both sensors simultaneously (A, indicated in the figure). Secondly, the repeated applications of compressive force (F_{chat12}) with the sensors responding differently, i.e. V_{N5} yielded an inverse response compared to the response of V_{N6} (C, indicated in the figure). This was interpreted as Fchat12 applied to sensor 5 causing the assumed sensor interaction effect on sensor 6.

The calibration event of Figure 42b depicted the effect of force applied only to a single sensor, as well as the resulting effect on sensors not being calibrated, i.e. sensor interaction. This interaction either caused a direct or an inverse response in V_N of the sensors not being calibrated, i.e. the interacting sensors. Whether the sensor interaction was direct or inverse, the change of V_N of interacting sensors was considerably less compared to the sensor being compressed. From this

figure it was also clear that the greater the force applied to a sensor, the greater the effect of sensor interaction.

The calibration events responsible for the most-suited post-explant calibration curves for each sensor, revealed the presence of sensor interaction not only between adjacent sensors, but amongst all sensors. The type of sensor interaction (i.e. direct and inverse) that occurred during the most suited post-explant calibration events is shown in Table 6. From this table it is evident that the type of influence that sensor interaction will have on sensor measurements depends on its position on the IPM.

Table 6: The type of sensor interaction caused by sensor calibration events (compression of a single sensor), indicating direct interaction (+), inverse interaction (-) and no interaction (0).

		Interacting sensor response																							
		SN068	SN069	SN074	SN076	SN068	SN069	SN074	SN076	SN068	SN069	SN074	SN076	SN068	SN069	SN074	SN076	SN068	SN069	SN074	SN076	SN068	SN069	SN074	SN076
		s1				s2				s3				s4				s5				s6			
Loaded sensor	s1					+	+	+	+	-	-	-	-	-	-	-	-	-	-	-	-	-	-	-	-
	s2	+	0	-	-					+	+	+	+	0	0	-	-	0	0	-	-	-	-	-	-
	s3	-	-	-	-	-	0	-	-					-	+	+	-	-	-	-	-	0	+	-	-
	s4	+	0	+	0	0	0	-	0	+	+	-	-					+	+	+	+	0	+	-	-
	s5	-	-	-	-	-	-	-	-	-	-	-	-	-	-	-	-					0	-	-	-
	s6	-	-	-	-	-	-	-	-	-	-	-	-	-	-	-	-	-	-	-	-				

-	Inverse response
+	Concurrent response
0	No response

Another phenomenon observed in these calibration events was the transient response of the sensor being calibrated upon the release of maximum calibration load (44 N), as also observed in Figure 42c. This produced a slight dip below the zero-load voltage (V_{Noff}) and immediately returned to the V_{Noff} level without the occurrence of extra significant oscillations.

4.10. Correlation of total force on IPM with morphometric data

The correlation between total normal forces measured by the IPM (F_{NT}) and relevant morphometric measurements were investigated for the experiments on conscious baboons and the ROM experiments, since they were performed in direct succession.

Considering the subM IPMs during experiments on conscious baboons, the $F_{NTmedian}$ measured by SN076 relative to SN068 and SN069 was 51.3% and 88.2%, respectively. The corresponding relative V_m was 51.9% and 88.9%, respectively and the corresponding relative M_m was 55.0% and 83.9%, respectively. A simple linear regression (SLR) analysis between $F_{NTmedian}$ and corresponding V_m resulted in a significant correlation with an $R^2 = 0.99$ and $p = 0.008$ ($n = 3$). Performing a SLR between the $F_{NTmedian}$ and corresponding M_m resulted in a correlation with an $R^2 = 0.98$ and $p = 0.08$ ($n = 3$). This correlation therefore only held for V_m ($p < 0.05$) and not for M_m ($p > 0.05$).

This correlation of a morphometric measurement with the $F_{NTmedian}$ considerably worsened when data from the subQ IPM was included – For M_m: R^2 = 0.23 with p = 0.53 (n =4); and for V_m: R^2 = 0.38 with p = 0.38 (n =4).

During the experiments on conscious baboons, the values of $F_{NTmedian}$ and F_{NTrest} were found to be very close to each other. The values of $F_{Nrest}/F_{NTmedian}$ obtained were 0.8, -2.0 and 3.3% for the subM IPMs (SN068, SN069 and SN076, respectively) and 1.6% for the subQ IPM. Nevertheless, $F_{NTmedian}$ was considered to be the better indicator of F_{NTrest} during these experiments. This was because observation of baboon behaviour during data acquisition periods revealed relatively low activity, as reported by technicians acquiring data. This was also evident from the data acquired: The $F_{NTmedian}$ was closer overall to F_{NTmean} than to F_{NTrest} over a very large dataset (n > 70 000). Furthermore, a SLR between F_{NTmean} and V_m and M_m, respectively, revealed similar results to $F_{NTmedian}$.

Considering only the subM IPMs during the ROM experiments, the $F_{NTmedian}$ measured in SN076 relative to SN068 and SN069 was 61.8% and 100.7%, respectively. A SLR analysis between the $F_{NTmedian}$ and corresponding V_m resulted in a correlation with an R^2 = 0.94 and p = 0.15 (n=3). Performing a SLR between the $F_{NTmedian}$ and M_m resulted in a correlation with an R^2 = 0.86 and p = 0.24 (n=3). These results did not reveal a significant correlation between the $F_{NTmedian}$ and either of these morphometric measurements, contrary to the experiments on conscious baboons. Inclusion of the data of the subQ IPM yielded considerably poorer correlations, similar to findings from the experiments on conscious baboons.

A simple linear regression (SLR) was also performed on data from the eStim experiments (all subM IPMs). This regression was performed between the $F_{NTmedian}$ and corresponding V_m resulted in a correlation with an R^2 = 0.23 with p = 0.52. Performing a SLR between the $F_{NTmedian}$ and corresponding M_m resulted in a correlation with an R^2 = 0.12 with p = 0.64. This analysis revealed that no correlation existed between the $F_{NTmedian}$ forces measured and these morphometric parameters. These parameters correlated even worse than equivalent correlations performed for both the experiments on conscious baboons and the ROM experiments.

4.11. Discussion

4.11.1. Feasibility of *in vivo* normal force measurement system

Feasibility of this system was demonstrated by its overall adequate design that delivered reliable results for evaluating the *in vivo* mechanical loading of pectoral implanted cardiac pacemakers. The adequate system design was confirmed in terms of its data acquisition capabilities, force measurement capabilities and versatility of the instrumented pacemakers (IPMs).

Adequate system design in terms of data acquisition capabilities was evident from the reliable wireless activation of the instrumented pacemakers (IPMs) *in vivo*, sufficient data transmission and sampling rates, and proper synchronization of video data with IPM data. The radio-frequency (RF) activation and transmission of *in vivo* IPM data (force and acceleration) were reliable and repeatable in the indoor cage environment with transceiver distances up to 3m. The measurement system facilitated sufficient sampling rates to capture dynamic *in vivo* loading conditions (up to 1000 Hz, signal quality dependent). Signal quality was generally very good and most remnant noise was sufficiently removed with a median filter (Section 3.6.1) and a custom high-pass filter (Section Appendix A.2).

The force sensor technology used (piezo-resistive from Tekscan) was found to yield dynamically responsive, repeatable and accurate force measurement under *in vivo* experimental conditions, revealing adequate system design in terms of force measurement capabilities. Responsiveness of the sensors under *in vivo* loading conditions was found to be very good (Figure 36). The repeatability and accuracy of contact force measurement with Tekscan sensors depended on certain experimental requirements that were all met during these experiments. These requirements included sufficient conditioning of sensors to experimental conditions, the repeated post-explant calibration data (yielding multiple points on the calibration curve) and a repeatable reference measurement.

Sufficient healing occurred for all four the IPMs that yielded the experimental data, indicating the adequacy of the system design in terms of biocompatibility. The premature explant of two of the three subQ IPMs was ascribed to surgical complications, not insufficient biocompatibility. Of the IPMs that remained implanted for the duration of the experiments, there was sufficient histological evidence to show that the fibrotic encapsulation of sub-muscular (subM) implanted IPMs was normal in terms of the normal physiological response to the *implantation* of a *foreign body* (Ratner et al. 2004).

The versatility of the IPM design was evident since it allowed proper functioning of all its components for varying experimental conditions, especially temperature and loading. Experimental temperatures ranged between room temperature (20°C), sterilization temperature (55°C) and *in vivo* temperature (37°C). This range of temperatures was within acceptable limits for all components of the IPM, which included force and acceleration sensors, power supply, data transmission/reception system, medical grade cast epoxy and protective cover plates. Experimental loading conditions on the force sensors were the only aspects of the IPMs that required further discussion. Force ranges of the sensors were evaluated based on the calibrated force range (0-44 N), since only the optimal force measurement range for these custom manufactured sensors was specified (18-36 N). The resting forces (F_{Nrest}) measured by the sensors ranged between 0 and 4.4 N for the different experiments. Despite being outside the optimal range, high measurement accuracy using multipoint

calibration curves (as obtained in this study) were recently reported for this type of sensor at low force ranges (< 30% of full range) (Brimacombe et al. 2009). Considering the experiments when sensors experienced the highest force magnitudes (experiments on conscious baboons), 95% of force data of all 24 sensors occurred between a lower limit (*P*2.5) of 1.3 ± 0.7 N and a higher limit (*P*97.5) 2.6 ± 1.5 N, while the maximum forces measured per sensor was 10.8 ± 10.2 N. From the distribution of total force measurement showing the infrequent occurrence of high force magnitudes (Figure 30) and the fact that only two (of 24) sensors exceeded the calibrated force range (F_N > 44 N, excluding manual external compression experiments), sensors were considered to have been operating at acceptable force levels. The acceptable limits of experimental temperature and loading were conducive to very good repeatability, low hysteresis and low drift of the force sensors (Tekscan 2005).

Although the IPMs functioned under experimental conditions within acceptable limits, the sensor technology utilized for measuring contact force (piezo-resistive sensors by Tekscan) displayed unique behaviour. This behaviour was characterized by the change in its sensitivity and drift, as reflected in the calibrated voltage range (ΔV_{Ncal}) and the change in zero-load offset voltage (V_{Noff}), respectively. Accommodating for sensor behaviour was an important consideration in the formulation of the voltage-force conversion method. The main aspects required to ensure stable sensor behaviour (good sensor performance) and aspects concerning the voltage-force conversion method are discussed below.

Recommendations to asses and ensure good force sensor performance were adhered to. These recommendations were obtained from the manufacturer and supplemented by independent studies evaluating the performance of these sensors under various experimental conditions. A recent report, published after performing the experiments of this study, confirmed that the necessary procedures were followed to minimize the possible loss of sensitivity over time, thereby yielding good repeatability and accuracy (Brimacombe et al. 2009), i.e. accommodating for change in V_{Noff} and minimizing the change of ΔV_{Ncal} due to changing experimental conditions. These procedures included conditioning of the sensors at experimental conditions (*in vivo* conditioning during the healing period), performing multiple experiments under identical experimental conditions to test for signal changes (multiple experiments within a series), combining data from different experiments of a series of experiments to avoid a constant bias over time (data from a series of experiments were processed as a single batch), minimizing shear loadings on the sensors (protective cover plates that also distributed the load over the whole sensing area of a sensor) and performing repeated calibrations before and after experiments. The procedures performed were supported by many other studies on this topic of obtaining good sensor performance (Luo et al. 1998; Otto et al. 1999; Bachus et al. 2006; Martinelli et al. 2006; Wilson et al. 2006). Recommendations for optimal sensor performance by the manufacturer coincided with these abovementioned procedures (Tekscan 2005; Tekscan 2008).

The resting sensor voltage (V_{Nrest}) was used as reference sensor measurement per series of experiments, despite having no confirmed zero value *in vivo.* This measurement was found to be stable and repeatable under dynamic loading conditions. Repeatable sensor measurements required conditioning of sensors to their experimental conditions (Tekscan 2008). Specifically, approximately 10-20 minutes were required for sensors to stabilize in response to a long-term change in constant

load (Otto et al. 1999), i.e. a change in the overall resting force despite acute force changes. Accordingly, sensors in this study reached suitable levels of stabilization (conditioned effect) since experiments on conscious baboons were only commenced after the healing period (8 weeks post-implant), the ROM and manual external compression experiments were only commenced after anaesthetization and experimental setup (≅30 minutes) and the eStim experiments were only commenced after experimental setup (≅20 minutes). The good repeatability of the sensor measurements was most prominently reflected in the low standard deviation of the V_{Nrest} values over a number of experiments under constant resting force (Figure 26). The normalized standard deviations of V_{Nrest} of all 24 sensors of all IPMs (Figure 26), were 4.1 ± 2.6%, 3.1 ± 2.3% and 1.3 ± 2.2% (mean ± std) for the muscle of the conscious baboon, muscle of the anaesthetized baboon and the exposed muscle, respectively. Note: No experimental data was acquired for SN074 and SN076 of the exposed muscle (eStim experiments). This stable and repeatable measurement (V_{Nrest}) confirmed the measurement capability of the sensors, as facilitated by the abovementioned procedures performed to ensure good sensor performance.

The sensor calibration procedures performed were conducive to good sensor measurement accuracy. Using 10 discrete user-defined points across the experimental force range and approximating the calibration curve with a 3rd degree polynomial, yielded the most accurate force measurements, as claimed by a recent report (Brimacombe et al. 2009). This calibration procedure was modified in this study and considered an improvement, simply because additional calibration data were obtained. The calibration procedure consisted of performing repeated calibrations at different time points for each sensor with a universal testing machine, before and after experimental data acquisition. Each calibration event yielded multiple data points (>>10 discrete points, forming a near continuous line) representing the calibration curve of each sensor. Performing the calibration procedure at different time points for each sensor was important, because each sensor had its own unique calibration curve that changed according to conditioning of the sensor and experimental conditions. These changes had to be incorporated in the voltage-force conversion method. Approximation of the calibration curves using a 5th degree polynomial curve yielded sufficient results that outperformed approximation using a 3rd degree polynomial curve.

All sensors responded similarly to a change in experimental conditions for the loading and temperature ranges previously discussed. These similar responses were observed for all sensors of all IPMs (24 sensors in total). It was reflected in the similar change of the zero-load offset voltage (V_{Noff}) and calibrated voltage range (ΔV_{Ncal}) of each sensor during calibrations performed at different time points, pre-implant and post-explant, respectively (Figure 22). Furthermore, it was reflected in the increase of V_{Nrest} between different series of experiments upon an expected decrease in F_{Nrest} during the *in vivo* experiments (Figure 26). This consistent behaviour was an important feature of the sensors that enabled the development of a reliable voltage-force conversion method applicable to all sensors during all experiments. Such a conversion method was necessary and therefore developed to accommodate for voltage signals of the sensors that changed as experimental conditions changed.

Assuming that there was a constant resting force (F_{Nrest}) experienced by a sensor throughout a series of experiments, was found to be reasonable. Even without accommodating for sensor drift between experiments of the same series, the low standard deviation of V_{Nrest} (discussed above) justified this

assumption, as was also expected. The assumption was utilized in the formulation of the voltage-force conversion method.

To obtain accurate *in vivo* force measurements, the *in vivo* sensor behaviour needed to be known. Findings of this study supported the use of a post-explant calibration curve (for each sensor), identified as the most suited calibration curve, to represent the sensor behaviour under *in vivo* experimental conditions. To approximate the calibration curve valid for *in vivo* loading conditions that was not obtained *in vivo*, knowledge about the sensor drift and change in sensitivity was required. These were reflected in the change of V_{Noff} and the change of ΔV_{Ncal}, respectively. Sensor drift (change of V_{Noff}), due to dynamic and static loading conditions, had been reported (Otto et al. 1999; Martinelli et al. 2006) and had to be accommodated for. This was incorporated in the formulation of the voltage-force conversion method. With regards to sensitivity, various experimental findings supported the stability of ΔV_{Ncal} during changes in experimental conditions (change in loading only, as was the case for the *in vivo* experiments). These included firstly, different post-explant calibration events at the same time point yielded negligible change in ΔV_{Ncal} (Figure 25). This pointed towards a constant ΔV_{Ncal} for similar experimental conditions (loading and temperatures). Secondly, very good repeatable measurements for all sensors over all experiments were obtained, as discussed above. The repeatable measurements were an indication of stable ΔV_{Ncal} for changing experimental loading conditions only. Thirdly, it was reported that temperatures higher than 30°C influenced sensor measurements, although its influence on sensitivity (ΔV_{Ncal}) was not specified (Luo et al. 1998). It was, however, recommended that calibrations be performed at experimentally similar conditions to accommodate for this occurrence. Despite post-explant calibrations not performed under exactly the same *in vivo* experimental conditions, sensitivity was found to be reasonably stable over different post-explant calibrations (Figure 22). Furthermore, although a change of ΔV_{Ncal} over subsequent post-explant calibration at different time points was observed, it was ascribed to sensors slowly becoming conditioned to being unloaded at room temperature (from being loaded at the *in vivo* temperature). The opposite of this was witnessed during the pre-implant calibrations during preconditioning of sensors (Figure 22). Accordingly, the most suited post-explant calibration curves were chosen mostly from the first time point post-explant (4 hours), since the sensitivity tended to decrease over time (Figure 22). This was true for 21 of the 24 sensors (Figure 23), while the most-suited calibration curves of the remaining 3 sensors chosen from the second time point. The change to the calibration curves of these 3 sensors at the second time point (24 hours) was minimal. Considering the slow change of ΔV_{Ncal} observed over large increments of subsequent time points ($\cong$24 hours) and the adequacy of the previously mentioned procedures followed to minimize the change in sensitivity, ΔV_{Ncal} was therefore reasonably deemed stable for all *in vivo* data acquisition. For the same reasons, it was considered reasonable to assume that the most suited post-explant calibration curve was valid for the sensor *in vivo* (having the same ΔV_{Ncal} and slope, but not V_{Noff}). Consequently, the most suited post-explant calibration curve was utilized by the voltage-force conversion method.

Accommodating for the drift of V_{Noff} was the most important prerequisite for obtaining accurate force measurements from Tekscan sensors, as previously reported (Otto et al. 1999). Accordingly, the voltage-force conversion method was formulated to accommodate for this drift (change of V_{Noff}) during each experiment using a reference measurement from each experiment, i.e. V_{Nrest}. The formulation was robust in the sense that a near zero-load ($F_N \cong F_{N0} = 0$) on a sensor only had to be

reached once during the whole series of experiments to sufficiently approximate V_{Noff} per experiment. Furthermore, as part of the conversion method, a custom high-pass filter was developed to accommodate for negative peaks in the sensor signal caused by RF noise or transient response of a sensor to unloading of the sensor.

A robust and general voltage-force conversion method was formulated by utilizing certain experimental findings as well as aspects about sensor behaviour published in literature. These findings included the consistent behaviour of all sensors observed under changing experimental conditions (loading and temperatures). It also included the following three assumptions: (1) stable sensor sensitivity (ΔV_{Ncal}) for all the *in vivo* experiments obtained from the most suited post-explant calibration curves, (2) constant F_{Nrest} per sensor per series of experiments, which was unique to a sensor but of unknown magnitude and (3) F_{N0} was reached at least once during a series of experiments. The first two assumptions were shown to be reasonable as discussed above. The last assumption was considered reasonable due to negligible pocket-wall tension, the wide variety of movements performed per series of experiment and the large amount of data obtained per series of experiment ($n > 720\,000$ for experiments on conscious baboons and $n > 41\,000$ for each of the other series of experiments). In addition, the repeatable V_{Nrest} obtained from each experiment was utilized as a reference measurement to accommodate for the possible occurrence of drift per experiment. Furthermore, the occurrence of unwanted minimum force peaks due to good signal quality and force magnitude-dependent transient response was infrequent. This finding was utilized to develop the custom high-pass filter to exclude the influence of these unwanted peaks on the resulting force measurements.

The force measurement accuracy resulting from the voltage-force conversion method could not be directly verified due to the inability to confirm the sensor load *in vivo*, which revealed scope for future work. However, two indirect methods of evaluation indicated good accuracy of the acquired force measurements. The first method consisted of comparing force measurements from different IPMs during different series of experiments. Results from the eStim experiments showed very good correlation between the F_{IL} and F_{NT} ($p < 0.05$), which was subject-specific (Figure 41), as expected. Similarly, the correlation between the resting force and the muscle volume for subM IPMs during the experiments on conscious baboons ($p < 0.05$, Section 4.10) also indicated that F_{NT} was dependent on F_{IL} and was subject-specific. This correlation was interpreted as follows: the muscle volume was the critical muscle property for evaluating the maximum F_{IL} that could be developed in different muscles with a similar pennation angle and optimal muscle fibre length (Eq. (9)). Therefore this finding supported the correlation between F_{IL} and F_{NT} in the experiments on conscious baboons, as found in the eStim experiments. It also confirmed that the force measurements between the different IPMs were comparable. The second method of indirectly evaluating force measurement accuracy was to investigate factors that would negatively influence the resulting accuracy. According to the conversion method algorithm, the accuracy will be negatively influenced when an offset error has occurred (Eq. (21)), i.e. an error in approximating the V_{Noff} per experiment. This offset error will occur if F_{N0} has not been reached over a whole series of experiments, which means that V_{Noff} has been overestimated. However, F_{N0} was considered to have been reached for each series of experiments, which was shown to be a reasonable assumption, as discussed above. Otherwise, this offset error would occur if the V_{Noff} identified by the voltage-force conversion method was unrepresentative of the actual force exerted on the sensor. The only way in which unrepresentative

sensor measurements could occur was if the custom high-pass filter threshold (λ) was chosen too low or if inverse sensor interaction caused minimum peaks lower than the valid minimum sensor voltage (V_{Nvmin}). The choice of λ was considered to be reasonable, based on experimental findings of filtered data (Appendix A.2). Inverse sensor interaction responsible for these unrepresentative minimum peaks was considered to have only significantly influenced the manual external compression experiments results, as explained below.

Sensor interaction was observed in the calibration procedures, showing that a load applied to a single sensor had an effect on the voltage signal of a neighbouring sensor, i.e. either an increase or decrease (Figure 42). The sensor interaction was expected to be complex under the distributed loads found *in vivo.* Experimental observations pointed towards sensor interaction during manual external compression experiments to such an extent that it caused erroneous force measurements. These erroneous measurements were evident from discrepancies in the results from the manual external compression experiments (chat76 and chat12 experiments, Figure 37 and Figure 38). Certain extracted peak force events measured by an IPM were larger than the actual applied forces, i.e. $\Delta F_{NT} > F_{chat76}$ and $\Delta F_{Nx} > F_{chat12}$. For an explanation of these results, consider that experimental conditions (loading and temperature) remained similar at resting levels for the ROM, chat76 and chat12 series of experiments and therefore a constant resting force on each IPM was expected. Sensor voltage measurements reflected this expectation, since the V_{Nrest} (per sensor) essentially remained constant for all three of these series of experiments (Figure 26). However, the resulting F_{Nrest} (and therefore also F_{NTrest}) substantially differed for each of these three series of experiments, as shown in Figure 43.

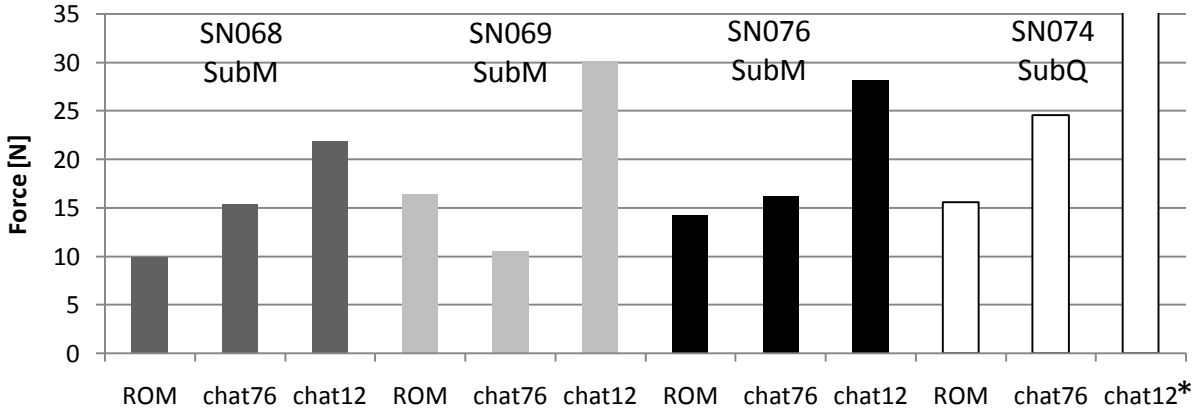

Figure 43: The total resting force (F_{NTrest}) measured by the IPMs for different series of experiments, although the "state" of the pectoralis major muscle for each series was the same, i.e. anaesthetized muscle. The asterisk (*) indicates the F_{NTrest} for the chat12 experiments of SN074 was 514.11 N, but for reasons of scale, the y-axis was limited.

According to the voltage-force conversion algorithm, the increase in ΔV_{Nbr} (difference between V_{Nrest} and valid minimum sensor voltage (V_{Nvmin})) between these three series of experiments (Figure 26) resulted in an increased F_{NTrest}. Since the V_{Nrest} essentially remained constant over these three series of experiments, the unexpected increase in F_{NTrest} was attributed to the acquired value of V_{Nvmin} (Eq. (11)). This increase in F_{NTrest} and the abovementioned discrepancy in comparative force measurement results were therefore attributed to very low values of the V_{Nvmin} obtained. These very

low values of V_{Nvmin} were considered to have been caused by inverse sensor interaction (applied force causing decrease in voltage of neighbouring sensor). These values of V_{Nvmin} were therefore unrepresentative of the actual zero-load sensor voltage (V_{Noff}), which it had to approximate. As a result, the forces obtained from the voltage-force conversion method for the whole series of experiments were overestimated. No comparative force measurements were available to evaluate the influence of sensor interaction on the force measurement accuracy during the series of experiments other than the manual external compression experiments. However, forces exerted during these experiments were all physiologically distributed over the IPMs, as opposed to the concentrated loads on certain sensors during the manual external compression experiments (rigid applicator). Furthermore, due to the relatively low levels of experimental loading during the ROM and eStim experiments (Figure 34 and Figure 41), the influence on force measurement accuracy was considered to be dismissible. This influence was also considered dismissible for the experiments on conscious baboons, due to the comparative force measurements obtained between different IPMs (discussed above) under relatively high experimental loading (Figure 24). By excluding the F_{NTrest} results from the chat76 and chat12 experiments due to inaccurate force results, the F_{NTrest} measured for the three different "states" of the muscle were found to represent the *in vivo* "state" of the muscle more adequately. This was evident when considering F_{NTrest} of the three remaining series of experiments, as shown in Figure 44. Each series of experiments represented a different "state" of the muscle, i.e. muscle of conscious baboon during experiments on conscious baboons, muscle of anaesthetized baboon during ROM experiments and exposed muscle during eStim experiments. This figure also shows that the F_{NTrest} for the acutely implanted IPM (SN066) was comparable to the F_{NTrest} of the two chronically implanted IPMs (SN068 and SN069). Therefore, the effect of sensor interaction on the force measurement accuracy was deemed negligible for all series of experiments, except for the manual external compression experiments, which were consequently excluded from further discussion concerning force results. The interaction of neighbouring sensors should be investigated in future studies.

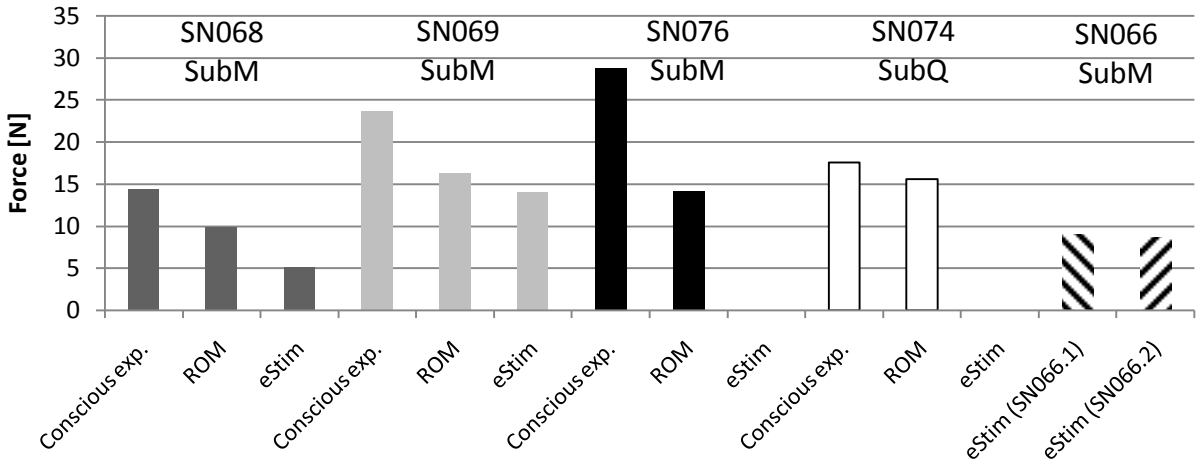

Figure 44: The total resting force (F_{Nrest}) measured by the IPMs for all series of experiments, except for the manual external compression experiments (chat76 and chat12). These results corresponded with the "state" of the muscle for each series of experiments, i.e. muscle of conscious baboon, muscle of anaesthetized baboon and exposed muscle. No eStim data were obtained from SN076 and SN074. The acute IPM used (SN068) in both animals yielded comparable results to the chronic IPMs (SN068 and SN069).

The sterilization process caused an increased sensitivity in all sensors in two of the four chronically implanted IPMs (SN074 and SN076). This change in sensitivity was clearly observed when comparing the pre-implant and post-explant calibration curves (Figure 22). However, the measurement accuracy of these sensors was proposed to not have been influenced by this change in sensitivity. The rationale for this was that the sensors of all four chronically implanted IPMs that underwent similar experimental conditions (loading and temperatures, discussed above) yielded similar *in vivo* measurement trends (change of V_{Nrest} and V_{Nvmin} between different series of experiments, Figure 26) and similar changes in drift and sensitivity (reflected in V_{Noff} and ΔV_{Ncal}, respectively) during pre-implant and post-explant calibrations, respectively (Figure 22). These experimental findings supported the assumption that the change in sensitivity that occurred during sterilization was once-off and permanent. The fact that only the sensors from SN074 and SN076 were affected was ascribed to the additional polyolefin gasket inserted around the sensing area of each sensor upon assembly of these two IPMs. It is recommended that these polyolefin gaskets be excluded from IPM assembly in future studies.

4.11.2. Evaluation of *in vivo* experimental outcomes

Evaluating the acquired *in vivo* mechanical loading data of the IPMs in the two different pectoral implant positions considered, i.e. sub-muscular (subM) and sub-coetaneous (subQ), revealed some insightful findings regarding resting forces, maximum forces and distribution of force events. Findings concerning the comparison of results from IPMs implanted in different positions were also of note. However, statistically significant findings cannot be concluded from these results due to the small sample size of this feasibility study (n = 3 for subM IPMs and n = 1 for subQ IPMs).

The total force (F_{NT}) experienced by the different sub-muscular IPMs was found to be similar in terms of the distribution, but varied in terms of maximum and resting levels (Figure 24). Three findings concerning the loading on the subM IPMs during experiments on conscious baboons stood out: Firstly, the total load exerted on the IPM (excluding compressive forces exerted from the outside onto the *pectoralis major*) was found to be dependent on the overlying *pectoralis major* muscle, based on the correlation between resting force and muscle volume (Section 4.10) and the intraspecific correlation established for baboons (Section 5.1). Secondly, the maximum force exerted on the IPM was considerably larger than a non-zero resting force. The distribution of the total force exerted on the subM IPMs resembled a normal distribution with a gradual tail towards maximum forces. Maximum and resting forces varied in magnitude for different IPMs (Figure 31) and although it was not clear which type of movements (e.g. pushing or pulling) were responsible for the highest loadings (Figure 32). The maximum force exerted on the subM IPMs was found to be between two and five times the resting force during experiments on conscious baboons. However, the comparison of this measure between different IPMs was limited since maximum voluntary contraction cannot be confirmed during conscious animal studies (baboons cannot be instructed to perform this type of task). Thirdly, the largest number of force events experienced by the IPMs were close to the resting force, i.e. maximum force events occurred very infrequently (Figure 30): for all three subM IPMs, 95% of the F_{NT} data was found to lie between a lower limit (*P*2.5) of approximately $0.8F_{NTrest}$ and a higher limit (*P*97.5) of approximately $1.2F_{NTrest}$. Furthermore, for the experiments on conscious baboons, the resting force differed very little from the median force. Differences of 0.8, -2.0 and 3.3% were obtained for SN068, SN069 and SN076, respectively.

The availability of only one sub-coetaneous IPM limited the comparative interpretation of the total force data (F_{NT}) between subM and subQ IPMs. However, certain findings from the experiments on conscious baboons are worth mentioning. The distribution of the total force events measured by the subQ IPM displayed a distribution that was much closer in resemblance to a normal distribution compared with the subM IPMs (no gradual tail towards higher forces). The shape of the distribution reflected the fact that an activated *pectoralis major* muscle compressed the subM IPM against the (less compliant) ribcage, while it compressed the subQ IPM against the (more compliant) skin. This was also supported by the results showing that the effect of anaesthetization caused a lesser decrease in resting force measured by the subQ IPM, compared to the subM IPMs, i.e. a decrease of 45%, 45% and 103% for the subM IPMs (SN068, SN069, SN076), respectively, and 13% for the subQ IPM from the conscious to anaesthetized baboon. Furthermore, the ratio of maximum to resting force was lower for the subQ IPM than for the subM IPMs during experiments on conscious baboons. This ration (F_{NTmax}/F_{NTrest}) for the subQ IPM was 1.4, while for the subM IPMs it was 2.2, 5.8 and 2.2 for SN068, SN069 and SN076, respectively. The absolute maximum and resting force magnitude measured by the subQ IPM were comparable to those measured by the subM IPMs, although it was found that the forces measured by the IPMs were subject-specific (regarding muscle properties). Of note was the fact that the resting force measured for IPMs in the different implant positions were substantial during the experiments on conscious baboons (> 14 N) and decreased when the baboons were anaesthetized to a level that was still substantially larger than zero (> 9 N).

The force exerted on the implanted IPM was caused by a combination of tension in and compression by the surrounding anatomical structures. More specifically, the total force on the IPM was found to have been caused by a combination of the extreme position of the arm movement, the fibrous encapsulation of the chronically implanted IPM, implant position and the strength of *pectoralis major* contraction. The extreme positions of the arm movements determined the force on an IPM, as supported by results from the ROM experiments, which yielded peak forces caused by the muscle being stretched/compressed over the IPM by the extreme positions of arm movements (Figure 32 and Figure 34). However, all extreme positions of arm movements did not cause these peak forces, e.g. circumduction of the arm caused a fluctuating, rather than continuous F_{NT} response (Figure 33). This was interpreted as the fusion of the fibrotic encapsulation to the surrounding anatomical structures influencing the total force exerted on the IPM. This meant that the total force exerted on the IPM was dependent on the position of the upper arm. The influence of the strength of the *pectoralis major* contraction was supported by results from the eStim experiments, showing the correlation that existed between F_{NT} and F_{IL} for each baboon. Although no statistically significant results were reached due to small a sample size, the implant position (subM or subQ) seemed to determine the influence that the strength of *pectoralis major* contraction had on the IPM. This was explained in the preceding paragraph concerning the differences in distribution of force events between these two implant positions. Furthermore, from the conscious to the anaesthetized experiments, a larger relative decrease in F_{NTrest} of the subM IPMs compared to the subQ IPMs was observed (Figure 44). Although the intensity of movements determined loading on the device, no clear ranking of specific movements during experiments on conscious baboons (e.g. pushing or pulling, Figure 32) or of the specific position of the arm during experiments on anaesthetized baboons (excluding the adducted arm, Figure 34) was possible.

The experimental findings presented in this report can provide essential supplementation to findings from cadaver studies. These findings specifically include the effect of conscious muscle tone and the occurrence of fibrotic encapsulation of the IPMs on total force not present in cadaveric specimens. The effect of the conscious muscle tone was evident from the decrease of resting force that occurred from experiments on conscious baboons compared to the ROM experiments, i.e. from muscle of conscious baboon to muscle of anaesthetized baboon, as shown in Figure 44. Between these two series of experiments, the resting force decreased by 32%, 34% and 49% for the subM IPMs: SN068, SN069 and SN076 respectively, and by 10% for the subQ IPM. Furthermore, this effect was evident from the higher maximum total forces exerted on the IPMs during experiments on conscious baboons than was observed during ROM experiments (Figure 24 and Figure 34, excluding adduction during ROM experiments). The effect of the fibrotic encapsulation of the device on F_{NT} was observed when considering the decrease in resting force between the ROM and eStim experiments, i.e. from muscle of anaesthetized baboon to exposed muscle, as shown in Figure 44. Between these two series of experiments, the resting force decreased by 48% and 14% for the subM IPMs: SN068 and SN069, respectively. Incising and removing the anatomical structures surrounding the IPMs was considered to have released tension caused by encapsulation during the healing processes (fusion of the fibrotic capsule to the surrounding anatomical structures).

The electrical stimulation experiments revealed proportionality between the in-line force (F_{IL}) and total force on the IPM (F_{NT}) through graded contractions. Regardless of the type of contraction (concentric, isometric or eccentric), the force developed by the muscle (F_{IL}) was related to the force exerted on the IPM (F_{NT}). This finding was obtained from the eStim experiments, which also revealed that the proportionality was subject-specific (Figure 41). Certain experimental conditions and procedures made it unclear whether the maximum F_{IL} and/or maximum F_{NT} was reached. These included muscle fatigue due to electrical stimulation (maximum eStim amplitude did not always yield maximum F_{IL} – Figure 41), accelerated muscle fatigue due to the use of constant frequency trains of electrical stimulation signal (compared to variable frequency trains, (Binder-Macleod et al. 1998)) and possible differences between the maximum F_{IL} for concentric, isometric and eccentric contractions (Pasquet et al. 2000).

5. Concept of an interspecific transfer function

5.1. Correlation of experimental parameters

The IPM data used to evaluate the correlation between the experimental parameters described in Section 3.7.2 was collected from the eStim experiments, i.e. IPM data from SN068, SN069, SN066.1 and SN066.2. In-line muscle force (F_{IL}) data used included only data that corresponded to the IPM data that were used. Only the F_{IL} peaks and corresponding total force on the IPM (F_{NT}) peaks were used in the subsequent analysis.

As was reported in Section 4.8, correlations were shown to exist between the F_{NT} and F_{IL} that were specific to each test subject (i.e. subject-specific). The next step was to determine if a generalised correlation existed (not subject-specific) by performing analyses on the data set consisting of the F_{NT} and F_{IL} data of all four experiments (n=51), as well as the additional parameters mentioned in Section 3.7.2.

A summary of results obtained from analyses on this described data set, is shown in Table 7. Simple and multiple linear regression (SLR and MLR) analyses were performed by including different parameters in each analysis for each case indicated (case A through F). By following a forward-stepwise approach of an MLR, the strongest correlation between each response (F_{NT} and ΔF_{NT} respectively) and the regressors was obtained when all of the considered parameters were included in the analysis (cases C and F). The regressors that significantly correlated with the response were indicated in the table. In MLR analysis, the inclusion of an additional regressor necessarily improved the coefficient of determination (R^2). In order to assess if the correlation actually improved upon addition of an additional regressor, an adjusted coefficient of determination (R^2_{adj}) was also determined. The R^2_{adj} adjusted the R^2 for the added degree(s) of freedom (when including additional parameters) and subsequently gave an indication of real improvement of the correlation (Vining 1998).

Table 7: Linear regression analyses results between different combinations of experimentally measured parameters.

Case	Response		Regressors									Correlation results		
	F_{NT}	ΔF_{NT}	F_{IL}	$t_{m,cb}$	L_m^{meas}	$w_{m,IPM}$	$w_{m,cb}$	V_m	M_m	PCSA	σ_m	R^2	R^2_{adj}	p-value
A	x		s									0.17	0.15	0.002846
B	x		s	z	s	s	s	z	z			0.69	0.66	<0.001
C	x		ns	z	s	s	z	z	z	z	s	0.71	0.68	<0.001
D		x	s									0.21	0.19	0.000702
E		x	s	z	s	s	s	z	z			0.63	0.60	<0.001
F		x	z	s	s	s	z	z	z	z	s	0.65	0.62	<0.001

z	Regressor included in analysis, but zeroed by the analysis (i.e. no correlation)
ns	Regressor included in analysis, correlation not significant ($p > 0.05$)
s	Regressor included in analysis, correlation significant ($p < 0.05$)

The finding of subject-specific results relating F_{NT} (or ΔF_{NT}) with only F_{IL} (Section 4.8) was confirmed, as was evident from the very poor correlation results obtained from cases A and D. In other words, the correlation between F_{NT} and F_{IL} using data from all four muscles was very poor.

These results showed that a stronger correlation existed when using F_{NT} as response (case C), as opposed to using ΔF_{NT} as response (case F), based on the R^2 and R^2_{adj} values. The strongest correlation obtained from these linear regression analyses was therefore case C of Table 7. The correlation obtained from this analysis (henceforth: intraspecific correlation), yielded the following regression equation:

$$F_{NT} = -1055.78 + (-0.24)F_{IL} + 3.24\ L_m^{meas} + 5.95\ w_{m,IPM} + 434.62\ \sigma_m \qquad (11)$$

Although F_{IL} did not reach significance from the analysis, it was included in the equation due to its borderline significance ($p = 0.054$) and since it was an experimentally measured parameter (unlike σ_m, which was derived from F_{IL}, Eq. (10)). Furthermore, the weights of these parameters for this analysis were not of importance, as explained below.

This correlation, only accounted for 71% of the total variability of F_{NT} ($R^2 = 0.71$). The predicted values of F_{NT} were plotted against the corresponding observed values for this regression equation, as shown in Figure 45.

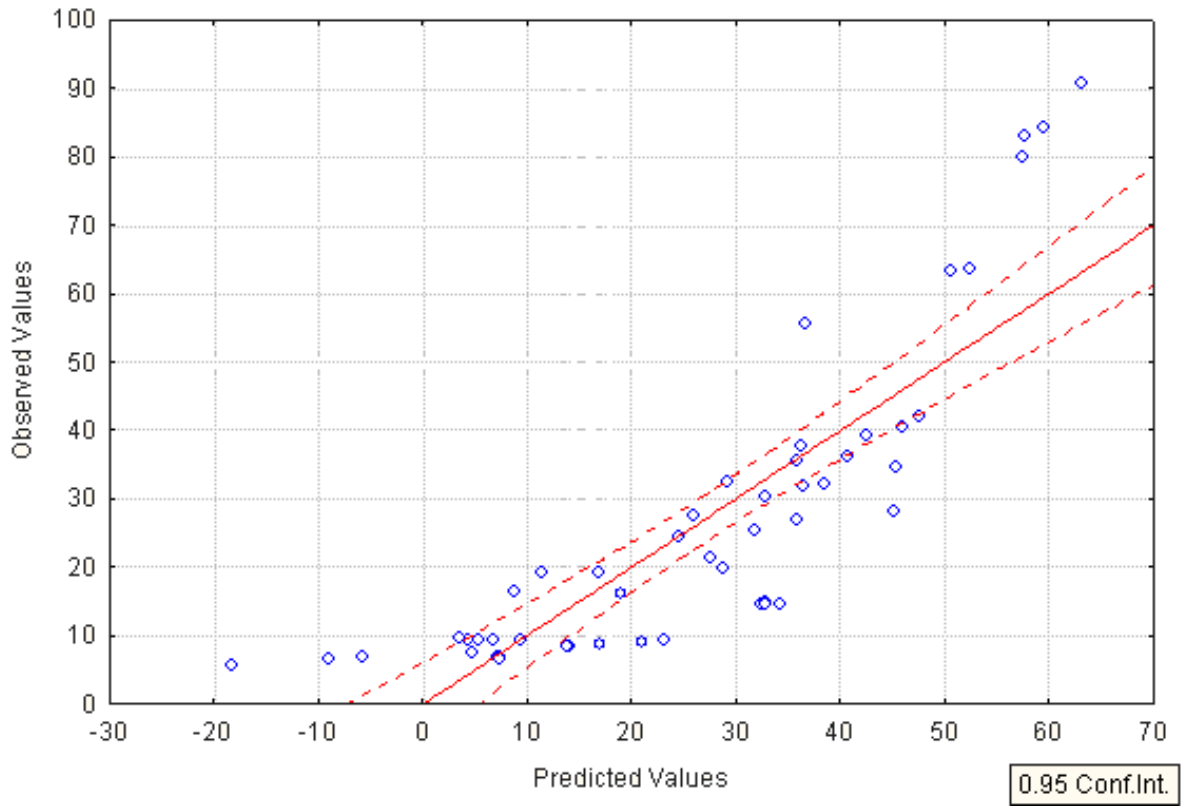

Figure 45: Predicted vs. observed values for the total force exerted on the IPM (F_{NT}) in the baboon. The predicted results were obtained from the intraspecific correlation equation that was established. The dashed line shows the 95% confidence interval.

The strength of the intraspecific correlation (reflected in $R^2 = 0.71$) was not affected by the unknown values of L_m/L_m^0 and $\cos(\theta)$ – both considered to be equal to 1. These values were reasonably assumed to be the same for all four muscles that made up the considered data set. This meant that the inaccuracy of these constants only influenced the value of the predicted F_{NT} – the correlation that was established between the response and the identified regressors remained unaffected. This was clear from the way that linear regression is formulated (Vining 1998). The values of L_m/L_m^0 and $\cos(\theta)$ were reasonably assumed to be equal, since baboons used were of the same species, gender and of similar body mass (*M*). This assumption was considered reasonable based on the small variation of the muscle fibre length and optimal fibre length (L_m/L_m^0) when these values are scaled to *M* for the same muscle, in different test subjects of the same species (Section 2.6.2). Furthermore, very small variation in the architectural properties of the same muscle, in different test subjects of the same species was reported for the rat muscles (Eng et al. 2008). Therefore, the weights of the regressors of Eq. (11) were meaningless, due to the guessed values of the constant L_m/L_m^0 and $\cos(\theta)$. Nevertheless, the emphasis of the resulting correlation (Eq. (11)) was that a linear relationship indeed existed between the response (F_{NT}) and each of these regressors individually, when all the other regressors were held constant ($p < 0.001$, $n = 51$).

The consistency of this result was investigated by redoing this MLR (case C), but using only the regressors identified in Eq. (11), which yielded similar results. Hence, the consistency of the results obtained by the forward stepwise MLR approach was confirmed when other possible influences were ignored. Accompanying statistical results of the MLR analysis of case C of Table 7 are attached in Appendix C, and did not yield any obvious irregularities.

5.2. Formulation of concept

5.2.1. Approach

A concept of an interspecific transfer function was proposed to relate the F_{NT} in baboons to the F_{NT} in humans (Section 3.7.1). The first step of this proposed interspecific concept was to investigate the correlation between F_{NT}, F_{IL} and morphometric parameters of baboons, as was done in the preceding section. This investigation revealed that a linear relationship indeed existed between F_{NT} and the parameters of the regression equation (Eq. (11)), although the regression equation only accounted for 71% of the variability of the predicted F_{NT} ($p < 0.001$). Usually, however, an $R^2 < 0.9$ for such an established correlation required a follow-up analysis or investigation to determine the cause(s) of the unexplained variance and thus yield a better prediction of F_{NT}. This correlation was not trivial and needed to be evaluated for soundness as part of the formulation of this concept.

Therefore, to formulate the concept of the interspecific transfer function, the following aspects were investigated:

- A theoretical based assessment was made of all parameters that possibly influenced F_{NT}, in order to evaluate the experimental findings of the established intraspecific correlation (Eq. (11)). This assessment enabled a greater understanding of the cause of the variance unaccounted for by this correlation. It was also used in subsequent steps to evaluate intraspecific and interspecific relationships of these parameters;

- The robustness of the established intraspecific correlation was evaluated for use with larger sample sizes of baboons (i.e. wider ranges of body mass), based on the findings from the first point of this list;
- The validity of using the established intraspecific correlation was evaluated for use with human parameters (a different species with a larger body mass), based on the findings from the first point of this list.

These steps are presented in the sections below.

5.2.2. Parameters that governed the normal force on the sub-muscular IPM

To better understand which parameters influenced F_{NT} in the subM position in the baboon and also to evaluate the experimental findings of the intraspecific correlation, a simplified representation of the *in vivo* IPM was proposed, as shown in Figure 46a. A block (IPM) resting on a surface (*pectoralis minor* supported by the ribcage), pressed downwards by an overlying rope in tension (*pec major* (sternum)). A mechanically equivalent model of this representation is presented in Figure 46b. The properties for the different components of this model were indicated in this figure and derived from theoretical considerations/published data. These properties were the following:

- The IPM was made from a rigid material;
- The *pec major* (sternum) had an axial stiffness (Hill muscle model (Hill 1938)) and assumed damping that was simplified as an axial elastic component (k_a) in parallel with an axial dampening component (c_a). The muscle was attached to its origin at an angle of ψ_1 and at its insertion at ψ_2 (angles of muscle attachment);
- The *pec major* (sternum) and *pectoralis minor* muscles both had transverse viscoelastic properties (Van Loocke et al. 2008), simplified as transverse stiffness components (k_{t1}, k_{t2} respectively) in parallel with transverse damping components (c_{t1}, c_{t2} respectively);
- The ribcage supporting the *pectoralis minor* had transverse stiffness and damping (Viano et al. 2000), simplified as a transverse stiffness component (k_r) in parallel to transverse damping component (c_r).

a)

b)

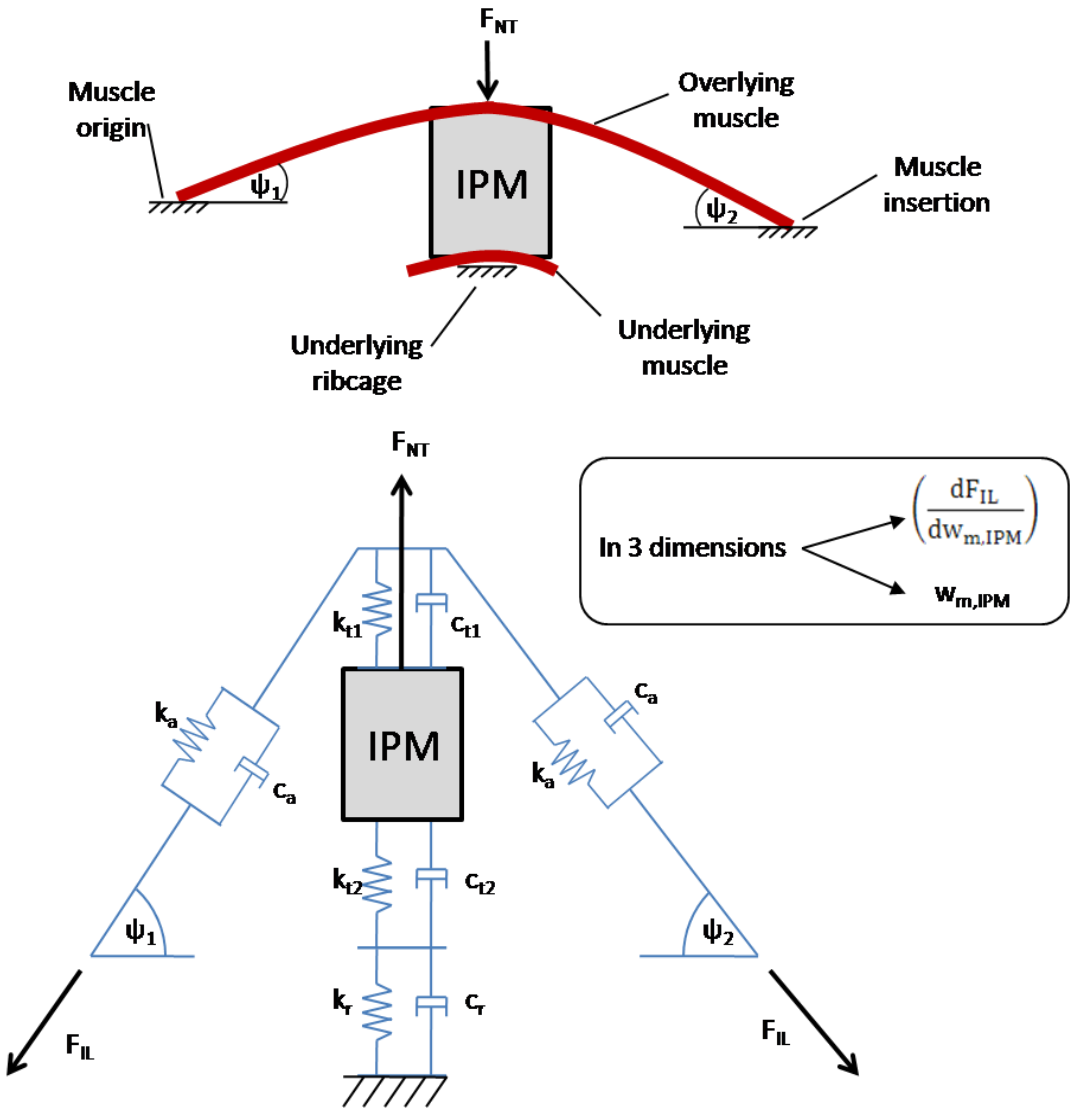

Figure 46: The total force (F_{NT}) experienced by the subM implanted IPM and the factors that influenced its magnitude showing, a) a simplified representation and b) an equivalent mechanical model displaying the model parameters.

The two-dimensional mechanical model (Figure 46b) showed the parameters considered to influence F_{NT}. These model parameters basically consisted of the in-line force generated in the overlying muscle (F_{IL}), the compressive material properties of the structures surrounding the IPM and the angles of muscle attachment (from the principal place of the IPM to the origin and insertion of the muscle, ψ_1 and ψ_2, respectively). In three dimensions, the width of the muscle ($w_{m,IPM}$) and the uniform distribution of F_{IL} throughout the width of the muscle $\left(\frac{dF_{IL}}{dw_{m,IPM}}\right)$ was considered to influence F_{NT}.

It was not obvious whether these model parameters were accounted for in the MLR analyses performed to establish the intraspecific correlation (Table 7). For this reason all model parameters were listed with F_{IL} and morphometric parameters that were proposed to have affected these model parameters (Eq. (11)), as shown in Table 8. It was evident from this table that not all morphometric parameters that affected the model parameters were included in the MLR analyses (Table 7). These excluded morphometric parameters were however not measured experimentally, which included

the thickness of and tension in the *pectoralis minor* (t_{mu} and σ_{mu} respectively), as well as the characteristic length of the ribcage (L_r). This characteristic length was proposed to have been determined by rib geometry and rib curvature responsible for the axial stiffness and damping of the ribcage.

The relative differences of all F_{IL} and morphometric parameters when considered intraspecifically and interspecifically, as well as the comparative influence of these parameters on F_{NT} when considered intraspecifically and interspecifically, were proposed in Table 8. Consider the following explanation of this table:

An intraspecific evaluation of parameters: Two baboons, baboon1 and baboon2, both had an implanted IPM and the model parameters for both were equal, except the parameter *A*. The relative difference of *A* between baboon1 and baboon2 was considered either large or small. This relative difference of *A* either had a strong or weak influence on the magnitude of F_{NT}, causing a significant (strong) or insignificant (weak) comparative influence of F_{NT} between baboon1 and baboon2.

An interspecific evaluation of parameters: Exactly the same as the abovementioned, but rather compare parameter *A* between baboon1 and human1.

Table 8: Model parameters that influenced the total normal force on the IPM (F_{NT}) were affected by the indicated morphometric parameters. The availability of morphometric data for baboons and humans are shown. In addition, the intraspecific and interspecific relative difference of the morphometric parameters is proposed. Finally, the intraspecific and interspecific influence of these morphometric parameters on F_{NT} is proposed.

Model	**Muscle force and morphometric data**						
Parameter	**Affected by muscle force/morphometric parameter**	**Availability of data**		**Relative difference**		**Comparative influence on F_{NT}**	
		Baboon	**Human†**	**Intra-specific**	**Inter-specific**	**Intra-specific**	**Inter-specific**
F_{IL}	F_{IL}	x		Large	Large	Strong	Strong
	PCSA	x	x	Large	Large	Strong	Strong
k_a	F_{IL}	x		Large	Large	Strong	Strong
	PCSA	x	x	Large	Large	Strong	Strong
c_a	F_{IL}	x		Large	Large	Strong	Strong
	PCSA	x	x	Large	Large	Strong	Strong
k_{t1}	$t_{m,cb}$	x		Small	Large	Weak	Weak
	σ_m	x		Large	Large	Strong	Strong
c_{t1}	$t_{m,cb}$	x		Small	Large	Weak	Weak
	σ_m	x		Large	Large	Strong	Strong
k_{t2}	t_{mu}			Small	Large	Weak	Weak
	σ_{mu}			Small	Large	Weak	Weak
c_{t2}	t_{mu}			Small	Large	Weak	Weak
	σ_{mu}			Small	Large	Weak	Weak
k_r	L_r			Small	Large	Weak	Weak
c_r	L_r			Small	Large	Weak	Weak
ψ_1, ψ_2	ψ_1, ψ_2			Small	Large	Weak	Strong
$w_{m,IPM}$	$w_{m,IPM}$	x		Small	Large	Strong	Strong
$\frac{dF_{IL}}{dw_{m,IPM}}$	eStim setup dependent*			Small	Small	Weak	Weak

*Electrode size, electrode placement, isolation of appropriate muscle etc.
†VHM (Garner et al. 2000). Obtaining additional morphometric measurements from the raw VHM data set was beyond the scope of this study.

The following characteristics were assumed for the test subject populations considered in Table 8:

- Baboons were considered to be adult, male Chacma baboons of approximately similar body mass to the ones used in these experiments;
- Humans were considered to be adult, human males of a body mass of approximately ≅90kg, i.e. similar to the Virtual Human Male (Spitzer et al. 1996);
- Musculoskeletal parameters were similar for both baboons and humans based on similarity of mammalian musculoskeletal tissue (Biewener 2000);

*Intra*specifically, it can be seen from this table that most of the F_{IL} and morphometric parameters identified in the intraspecific correlation (Eq. (11)) were related to the model parameters. The only exception was L_m^{meas} , although it had an indirect influence on F_{NT}, since it was used to obtain PCSA and in turn to obtain σ_m. As can be seen in this table, the proposed relative difference of the parameters did not necessarily dictate their influence on F_{NT} (e.g. $w_{m,IPM}$ having a small relative difference but a comparatively strong influence on F_{NT}). Furthermore, most model parameters proposed to have an influence on F_{NT}, were affected by the morphometric measurements found to

have a significant influence on F_{NT} (Table 7). The morphometric parameters listed in this table that were not considered in the MLR analysis of Table 7, were proposed to have a weak intraspecific comparative influence on F_{NT}. This statement is briefly qualified as follows:

- *Pectoralis minor* thickness (t_{mu}) and tension (σ_{mu}) – viscoelastic properties of passive muscle under compression (Section 2.3.1) and the compressive force present at rest prior to the onset of contraction ($F_{NTrest} > 0$) were assumed to cause relatively high values of k_{t2} and c_{t2} and therefore had a weak intraspecific influence on F_{NT}. Furthermore, since $t_{m,cb}$ was shown to not have an intraspecific influence on F_{NT} (Eq. (11)), then for $t_{mu} < t_{m,cb}$, the influence of t_{mu} on F_{NT} was reasonably assumed to be even less;
- The compliance of the ribcage, dependent on L_f – based on the relatively high values of stiffness and damping of the human chest (Viano et al. 2000), it was assumed that k_r and c_r had a weak intraspecific influence on F_{NT} Furthermore, under experimental conditions where the shoulder was left to move freely, which was responsible for less compression on the ribs compared to an isometric contraction, for example;
- The angles of muscle attachment (ψ_1, ψ_2) – since the F_{NT} and F_{IL} were recorded at the maximum levels and the shoulder complex of the baboons was free to move, the comparative change in ψ_1 and ψ_2 was assumed to be negligible and therefore assumed to have had a weak intraspecific influence on F_{NT};
- The uniform distribution of F_{IL} throughout $w_{m,IPM}$ $\left(\frac{dF_{IL}}{dw_{m,IPM}}\right)$ – although the distribution of motor units over the cross-sectional area of the muscle have been reported to be non-uniform for certain muscles (Navallas et al. 2007), it was deemed reasonable to assumed uniform distribution of motor units over the cross sectional area of the muscle, as have been done in previous studies, e.g. Hamilton-Wright (2005). The uniform distribution of F_{IL} was assumed to have had a weak intraspecific influence on F_{NT}.

The same parameters considered having strong and weak, respectively, *intra*specific comparative influence on F_{NT} were assumed to have a strong and weak, respectively, *inter*specific influence, except for ψ_1 and ψ_2. Agreement of the comparative influence on F_{NT} in humans and baboons was based on the similarities between humans and baboons described in Section 2.5. Despite these similarities, the torso of a baboon and a human differ geometrically (Section 3.4) and therefore ψ_1 and ψ_2 were considered to have a comparatively strong influence on F_{NT} between baboons and humans.

The F_{IL} and morphometric parameters proposed to have a strong intraspecific and interspecific influence on F_{NT}, needed to be measured (or estimated) to assess its actual influence on F_{NT}. This assessment was performed for the baboons considered in this study and resulted in the intraspecific correlation (Eq. (11)). This intraspecific evaluation needed to be evaluated for the robustness in a larger population of baboons. Furthermore, it had to be assessment whether this intraspecific correlation was suitable for humans, by considering the interspecific correlation of these parameters. These steps are performed below in Section 5.2.3 and Section 5.2.4, respectively, which completes the formulation of the interspecific transfer function.

5.2.3. Robustness of the established intraspecific correlation for baboons

The intraspecific correlation was considered to be robust for use with larger sample sizes of baboons (i.e. wider ranges of body mass (*M*)) if changes of the F_{IL} and morphometric parameters were linearly related with changes to the corresponding model parameters, i.e. proportionality between F_{IL} and morphometric parameters, and model parameters. This was based on the fact that a linear change in the F_{IL} or morphometric parameter had a linear influence on F_{NT}, since a linear regression equation has been established (Eq. (11)). Consequently, if a change in the model parameter caused a linear change to the muscle force or morphometric parameter, it also had a linear influence on F_{NT}. Due to the small sample size of this correlation, it was desirable to assess the robustness of these findings for larger sample sizes (in terms of body mass – *M*).

The specific F_{IL} and morphometric parameters evaluated for intraspecific robustness were those obtained from the intraspecific correlation (Eq. (11)), i.e. those that had a significant influence on F_{NT}. The existence of a linear relationship between each morphometric parameter with its corresponding model parameter was evaluated presuming all other parameters of an equivalent experimental setup remained constant. These results are shown in Table 9 and further discussed below.

Table 9: An assessment to determine the robustness of the intraspecific correlation established in baboons. This was done by investigating whether intraspecific linear relationships between the identified morphometric parameters and associated model parameters existed. This assessment was performed one parameter at a time, assuming all other parameters, of an equivalent experimental setup, remained constant.

Case	Morphometric parameter	Associated model parameter(s)	Relationship between model and morphometric parameters
A	F_{IL}	F_{IL}	Linear
B	L_m^{meas}	F_{IL}	Linear
C	$w_{m,IPM}$	$w_{m,IPM}$	Linear
D	σ_m	F_{IL}	Linear
E	σ_m	k_{t1}, c_{t1}	Negligible

The linear relationships for cases A and C were trivial. The relationship was linear for both cases B and D, since L_m^{meas} was proportional to PCSA (Eq. (9)). The PCSA in turn was proportional to the maximum isometric force of a muscle (F_m^0) (Section 2.6.3). The existence of a linear relationship between the σ_m and the k_{t1} and c_{t1}, respectively, was unknown. Nevertheless, the assumptions made about these parameters in Section 5.2.2 above revealed that the influence of σ_m (or F_{IL}) on F_{NT} (case D) was comparatively much larger that the influence of k_{t1} and c_{t1} on F_{NT}. Therefore a change to σ_m was reasonably assumed to have had a negligible effect on k_{t1} and c_{t1}, and therefore a negligible effect on F_{NT}.

From the assessment of linear relationships made in Table 9, the intraspecific correlation was deemed sufficiently robust to be used in larger sample sizes of baboons (i.e. wider ranges of body mass (*M*)) under similar experimental conditions.

5.2.4. Assessment of suitability of the intraspecific correlation for humans

The intraspecific correlation established for baboons was considered to be suitable for use with human parameters (a different species with larger *M*) if changes of the F_{IL} and morphometric

parameters from baboons to humans were linearly related with changes to corresponding model parameters. This was based on the same reasons considered when evaluating the robustness of the intraspecific correlation in larger sample sizes of baboons (preceding section).

The only difference between this assessment and the one of the preceding section was that additional morphometric parameters were added to ones evaluated and that the parameters were evaluated interspecifically (between baboons and humans). These additional morphometric parameters were those proposed in Table 8 and had unknown influences on F_{NT}. The existence of a linear relationship (proportionality) between each morphometric parameter with its corresponding model parameter was evaluated presuming all other parameters of an equivalent experimental setup remained constant. These results are shown in Table 10 and further discussed below.

Table 10: An assessment to determine the suitability of using the intraspecific correlation established in baboons for humans. This was done by investigating whether interspecific linear relationships between morphometric and associated model parameters existed. This assessment was performed one parameter at a time, assuming all other parameters, of an equivalent experimental setup, remained constant.

Case	Morphometric parameter	Included in intraspecific analysis	Associated model parameter(s)	Relationship between model and morphometric parameters
A	F_{IL}	Yes	F_{IL}	Linear
B	L_m^{meas}	Yes	F_{IL}	Linear
C	$w_{m,IPM}$	Yes	$w_{m,IPM}$	Linear
D	σ_m	Yes	F_{IL}	Linear
E	σ_m	Yes	k_{t1}, c_{t1}	Negligible
F	PCSA	Yes	k_a, c_a	Negligible
G	$t_{m,cb}$	Yes	k_{t1}, c_{t1}	Negligible
H	t_{mu}	No	k_{t2}, c_{t2}	Negligible
I	σ_{mu}	No	k_{t2}, c_{t2}	Negligible
J	ψ_1, ψ_2	No	ψ_1, ψ_2, F_{NT}	Nonlinear
K	eStim setup dependent	No	$\frac{dF_{IL}}{dw_{m,IPM}}$	Negligible

Since the musculoskeletal material properties were the same for baboons and humans (Biewener 2000), the same linear relationships identified for the intraspecific assessment in Table 9 (cases A to E) was considered suitable for this interspecific assessment. Two parameters that were included in the (intraspecific) MLR analysis of Table 7 were included in this table, i.e. PCSA and $t_{m,cb}$ (cases F and G). Since these parameters varied experimentally in the baboons, but were found not to have had a significant influence on F_{NT}, their interspecific influence was also assumed negligible. The relationships between the morphometric and associated model parameters of cases H, I and K were deemed negligible, based on the assumptions made in Section 5.2.2 regarding the negligible influence of the *pectoralis minor* on F_{NT}.

For case J, the relationship between the morphometric and model parameters was obviously linear (same parameters), but these parameters were not included in the intraspecific analysis of Table 7. Therefore, consider the relationship between ψ_1, ψ_2 and F_{NT}, as is evident from Figure 46:

$$F_{NT} = F_{IL}(\cos\psi_1 + \cos\psi_2) \quad (12)$$

This equation showed that the relationship of either ψ_1 or ψ_2 with F_{NT} was nonlinear while holding all other parameters constant. The ψ_1 and ψ_2 were not included in the intraspecific analyses (Table 7) and the relationship between ψ_1, ψ_2 and F_{NT} was indeed nonlinear. Therefore, based on the assumption at the beginning of this section, the intraspecific correlation was not suitable for use with human data under similar experimental conditions.

Nevertheless, consider the fact that ψ_1 and ψ_2 did not influence the magnitude of F_{IL} or σ_m – it only influenced F_{NT} and the morphometric parameters associated with the compliance of structures surrounding the IPM, i.e. k_{t1}, c_{t1}, k_{t2}, c_{t2}, k_r and c_r. Furthermore, consider that it was shown that the interspecific effect on F_{NT} of these compliance related parameters were reasonably deemed negligible (earlier in this section) and that $\psi_1 + \psi_2$ (baboons) > $\psi_1 + \psi_2$ (humans) (based on the axial torso measurements, Section 4.4). From this information it was deemed reasonable to propose that the intraspecific correlation was conditionally suitable for use with human data under similar experimental conditions. This suitability condition was that the final F_{NT} had to be corrected after its calculation, in order to accommodate for the difference in ψ_1 and ψ_2 between baboons and humans. Using these values, the F_{NT} can then be corrected for a specific human test subject according to the geometric relationship defined in Eq. (12).

Therefore, from the assessment of linear relationships made in Table 10 and the abovementioned considerations, the intraspecific correlation was deemed conditionally suitable to be used for humans under similar experimental conditions. It can also be said that the intraspecific correlation was considered to be conditionally scale-invariant between baboons and humans for the specified range of *M.*

5.2.5. Final concept

The final concept for an interspecific transfer function was formulated using the proposed indirect route (Section 3.7.1) and the assessments evaluating the soundness of its components (preceding sections). The final concept for an interspecific transfer function of relating the F_{NT} in baboons to the F_{NT} in humans is presented in Figure 47. The main steps of this interspecific transfer function were the following:

a. Experimentally obtain the relevant morphometric measurements, F_{IL} and corresponding F_{NT} from baboons;
b. Perform linear regression analysis in order to obtain an intraspecific correlation;
c. Obtain the F_{IL} and morphometric measurements of the particular human test subject, found to have intraspecifically influenced F_{NT};
d. Use the intraspecific correlation of baboons for humans by simply inserting the relevant human data to obtain an uncorrected value of F_{NT};
e. Correct the value of F_{NT} for the nonlinear influence of ψ_1 and ψ_2 on F_{NT}, by using the average ψ_1 and ψ_2 of the baboons and the ψ_1 and ψ_2 of the human test subject to obtain the F_{NT} for humans.

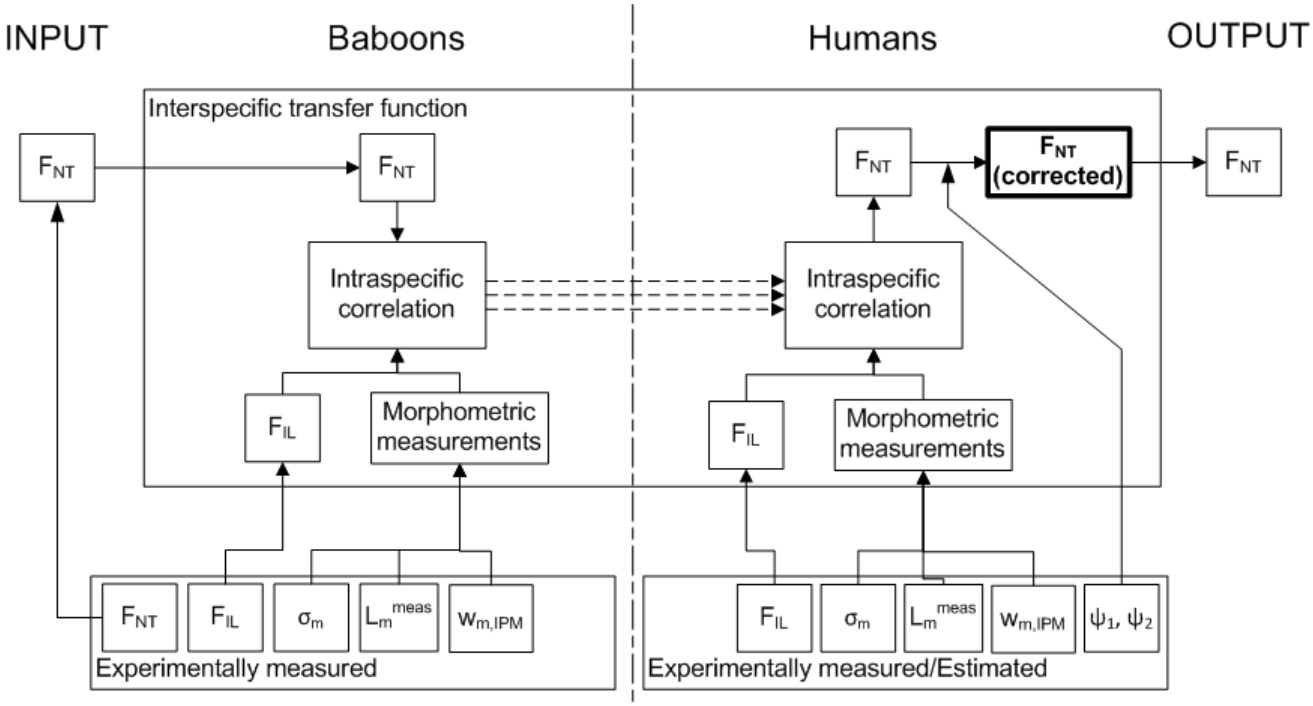

Figure 47: Concept of the interspecific transfer function used to relate the total force experienced by a subM IPM in vivo (F_{NT}) in baboons to the F_{NT} in humans. This concept utilized the influence of the in-line muscle force (F_{IL}) and morphometric parameters on F_{NT} in baboons, to find a similar relationship in humans and thereby yielding the F_{NT} in humans.

5.3. Discussion

A concept was formulated to relate the total force experienced by a pectorally implanted cardiac pacemaker (F_{NT}) in baboons to the equivalent force in humans, i.e. interspecific transfer function. The formulation of this concept was made possible by similarities between baboons and humans for this application, in terms of anatomy and morphology. Furthermore, the formulation of this concept utilized the correlation that was found to exist between the total normal force and in-line muscle force and associated morphometric parameters in the same species.

The baboon was the best available animal model found to be suitable for evaluating the *in vivo* mechanical loading on a pectorally implanted pacemaker in humans, based on reviewed literature and experimental findings from this study. For this type of interspecies comparison, essential similarities between baboons and humans included the presence of a clavicle that enabled similar movements of the upper limb (Voisin 2006). No other laboratory animal species has this feature. In addition, the pectoral implantation site of the IPMs in baboons compared very well to those of humans, relative to surrounding anatomical structures (Section 4.4). Furthermore, although muscle density of mammalian muscle tissue has been accepted as 1.0597 g/cm^3 (Ward et al. 2005), the actual measurement depended on the fixation method of the muscle upon explantation. Therefore, considering that no fixation of muscles were used in these exeriments, the density measurements of the *pectoralis major* muscles yielded 1.127 ± 0.050, which were comparable with muscle density reported as 1.112 ± 0.006 g/cm^3 of 4% formaldehyde-fixed muscle (Ward et al. 2005). However, due to certain specific differences between baboons and humans, a transfer function was needed for this type of comparison to accommodate for these differences. These included body mass and method of locomotion. Body mass varied between 15 and 31 kg for quadrupedal Chacma baboons (Fleagle 1999) and between 76 and 83 kg for bipedal human males (Anonymous 2006). In addition, a degree of positive allometry was found when comparing the upper limb of the baboon with the upper limb of the Virtual Human Male (VHM). Considering the *pectoralis major* muscle in particular, the muscle mass relative to the total body mass (at explant) was larger for the baboon than for the human. This ratio yielded 6.2 x 10^{-3} ± 1.6 x 10^{-3} for the baboons compared to a slightly smaller ratio of 7.9 x 10^{-3} for the VHM with a reported body mass of 90 kg (Spitzer et al. 1996), a *pectoralis major* volume of 676.4 cm^3 (Garner et al. 2000) and mammalian muscle density of 1.0597 g/cm^3 (Ward et al. 2005). Another difference was the angles of muscle attachment (ψ_1 and ψ_2). Although not directly measured, these angles were expected to be larger for the baboon than for the human due to chest curvature at the pectoral implantation site (Figure 27). These differences were considered to be adequately represented and accommodated for in the formulation of the concept of an interspecific transfer function.

A concept for an interspecific transfer function (baboon to human) was formulated by utilizing experimental data from baboons together with theoretical considerations. The basic building blocks of this concept were (1) intraspecific correlations, which revealed the parameters that influenced the magnitude of F_{NT} per species (intraspecifically) and (2) the relationships of these parameters between different species (interspecifically). The soundness of this concept was evaluated against a model describing the parameters that influence F_{NT} (Section 5.2.2). This model was built by using experimental findings and theoretical considerations. The resulting concept of an interspecific transfer function, when verified in experiments utilizing a larger sample size, and taking into consideration the recommendations from this report, may enable the prediction of force

magnitudes exerted on an IPM-sized pacemaker implanted sub-muscularly (subM) in humans by the surrounding anatomical structures.

Experimental data was used to establish an intraspecific correlation for baboons that revealed the parameters required to predict the subject-specific forces exerted on the IPM (F_{NT}). Experiments were accurately reproduced for each IPM considered. A multiple linear regression (MLR) analysis using experimentally measured and derived parameters yielded a significant correlation between F_{NT} as response and the different regressors ($R^2 = 0.71$ and $p < 0.001$). These regressors were the in-line muscle force (F_{IL}), the in-line muscle stress (σ_m), the measured muscle length (L_m^{meas}) and the width of the muscle over the IPM ($w_{m,IPM}$). This correlation was classified as the intraspecific correlation (Eq. (11)). Despite 29% of the variability that remained unaccounted for, the intraspecific correlation was deemed sufficient for use in formulating the concept for the interspecific transfer function. This was based on the robustness of the intraspecific correlation obtained from data from only four IPMs over a wide range of body mass ($15 < M < 31$ kg). The robustness, in turn, was based on the fact that the model parameters (mentioned above) showed proportionality to the corresponding experimentally obtained parameters of the intraspecific correlation (Eq. (11)). The comparison revealed information about parameters not accounted for by the intraspecific correlation. Assumptions, that were deemed reasonable, were made to demonstrate that these unaccounted parameters had a negligible effect on F_{NT}. The intraspecific correlation best explained the variability of F_{NT} compared to any of the other correlations performed, e.g. comparing the worst correlation from the eStim experiments that was only valid for that specific IPM ($R^2 = 0.56$, Figure 41) to the intraspecific correlation that used data from all four IPMs ($R^2 = 0.71$, Table 7).

The intraspecific correlation for baboons was found to be suitable for use as an intraspecific correlation for humans. This was based on the re-evaluation of the abovementioned comparison between model and corresponding experimentally obtained parameters, which was extended to evaluate the parameters between species (interspecifically). Except for the angles of muscle attachment (ψ_1 and ψ_2), all experimental parameters that had a significant effect on F_{NT} remained proportional to the corresponding model parameters when scaled interspecifically. It was shown to be suitable to determine F_{NT} in humans by inserting human parameters into the intraspecific correlation (obtained from baboons) and to only accommodate for ψ_1 and ψ_2 afterwards (Section 5.2.4). Therefore, the intraspecific correlation obtained using baboon parameters was considered to be scale-invariant between baboons and humans ($15 < M < 100$ kg), on the condition that the angles of muscle attachment are accommodated, as suggested.

The intraspecific correlation accounted for 71% of the variability measured experimentally ($R^2 = 0.71$). The remaining 29% was unaccounted for. Two factors provided some insight into the possible causes of this unaccounted variability. Firstly, according to the multiple linear regression (MLR) analysis performed, a parameter found to not have a significant influence on F_{NT} (Table 7) may have had a non-linear influence on F_{NT}. One example of an ambiguous result was the assumed influence on F_{NT} by the muscle thickness at the crossbar of the buckle strain transducer ($t_{m,cb}$). Although transverse force response of muscle under compression was nonlinear (Van Loocke et al. 2008), the linear regression analyses showed that $t_{m,cb}$ had a significant influence on ΔF_{NT} (case F of Table 7), but not on F_{NT} (case C of Table 7). This could be interpreted as $t_{m,cb}$ being linearly (or near linearly) correlated to ΔF_{NT}, but not to F_{NT}. Regardless, it seemed that $t_{m,cb}$ did have some influence on F_{NT}. However, this thickness and other parameters relating to the transverse compliance of the

structures surrounding the IPM (i.e. $t_{m,cb}$, t_{mu}, k_{t1}, k_{t2}, k_r, c_{t1}, c_{t2} and c_r) were reasonably assumed to have a negligible effect on F_{NT}. Thus, the accumulated influence of these parameters might have contributed to the unaccounted variability of the intraspecific correlation. Secondly, certain experimental aspects might have contributed to the variability and an improvement in these procedures could reduce the unaccounted variability, e.g. increasing the measurement precision of the in-line force measurement system (4.7 N resolution for range: $1.0 < F_{IL} < 185$ N) and the ruler measurements of morphometric parameters such as $t_{m,cb}$ (0.5 mm resolution for range: $3.5 < t_{m,cb} < 6.5$ mm).

The proposed concept of an interspecific transfer function benefited from scrutinizing the abovementioned comparison between model and corresponding experimentally obtained parameters. The latter parameters resulted from the multiple linear regression (MLR) analysis. The importance of this step stemmed from the fact that parameters excluded by the MLR analysis (as evident from the intraspecific correlation (Eq. (11)) might have been interpreted as either having no influence on F_{NT}, having a non-linear influence on F_{NT} (considered above) or not having a direct influence on F_{NT} on condition that the parameter was more or less equal throughout the dataset. To illustrate this latter point, consider the angles of muscle attachment (ψ_1 and ψ_2). Although not directly measured, they were reasonably assumed equal for the four muscles considered, based on similar sized animals. A parameter that is equal throughout the whole dataset will not be identified as having a significant influence on F_{NT} ($p < 0.05$) by the MLR analysis. Nevertheless, ψ_1 and ψ_2 directly influenced the F_{IL} (Eq. (12)), and therefore indirectly influenced F_{NT}. By comparing the parameters obtained experimentally with the corresponding model parameters, the limitation of using MLR analysis in this application was identified and was accordingly accommodated for during the interspecific evaluation (Section 5.2.4). It is therefore recommended that future studies utilizing MLR analyses on larger data sets account for this limitation of the MLR by measuring all required experimental parameters and re-evaluating all the model parameters to establish if any other parameters have a similar indirect influence on F_{NT}.

The resulting concept of the interspecific transfer function therefore used the relationship between the total normal force and in-line muscle force and associated morphometric parameters in baboons. To apply this relationship to humans, it was considered suitable to only correct for the difference in angles of muscle attachment between humans and baboons. By following this route to obtain the total normal force on an implanted pacemaker in humans, it was evident that the human parameters required to predict F_{NT} can be measured either non-invasively (medical imaging data) or approximated (muscle models for approximating F_{IL}). Furthermore, upon verification of this proposed concept in future studies, the way in which this concept was formulated enables it to predict subject-specific F_{NT} in humans, without the need to perform additional animal experiments.

6. Conclusions and recommendations

6.1. Conclusions

The measurement system presented in this study was found to be suitable for evaluating *in vivo* mechanical loading conditions on an implantable device, as well as for measuring loads applied from outside the body (externally). The use of this measurement system may be extended to evaluate forces exerted on other implantable devices, such as insulin pumps, pacemakers used for deep brain stimulations etc. Furthermore, as this measurement system enables the evaluation of mechanical loading during *in vivo* conditions, it may also prove feasible to be used during events such as implantation to assess surgical handling forces.

This measurement system featured a biocompatible implantable device that housed all the required electrical and mechanical components, i.e. the instrumented pacemaker (IPM). The IPMs can be reliably activated and transmit/receive data in sub-optimal RF environments, e.g. through steel bar cage-doors. The power capabilities of the batteries used in the IPMs proved to be sufficient with the described usage patterns over a ±15 week period. The prolonged period makes it viable to use the IPMs in studies that require sufficient healing of implants (±6 weeks) as well as a subsequent period of experimental data acquisition. Synchronization of the IPM force and acceleration data with video data facilitates the study of specific activity patterns of a test subject and makes it possible to determine the activity-related forces. The sensor technology utilized to measure contact forces on the IPM yields sufficiently repeatable and accurate results when its intrinsic sensor characteristics are accommodated for, i.e. accommodating for sensor-specific non-linear calibration curves, as well as the change in its sensitivity and drift. To accommodate for these characteristics, each sensor needs to be conditioned under experimentally equivalent loading and temperature levels and repeatedly calibrated at specific time points. In addition, a suitable voltage-force conversion method is required to utilize the acquired sensor voltage measurements to yield measured forces equal to actual sensor forces.

Generally, the force exerted on the implantable cardiac pacemaker depended on the extreme position of arm, intensity of the movement and subject-specific geometries of anatomical structures surrounding the pacemaker. The latter point was true especially for the large role that the contraction of the *pectoralis major* muscle played in exerting force on the implantable cardiac pacemaker, even when only considering the effect of conscious muscle tone – to a larger extent for subM than subQ implanted devices.

Although it was clear that no statistically significant conclusion could be drawn due to the small sample size, certain findings regarding the subM and subQ implant positions were of note. No clear differences were observed when comparing the resting force between the three subM and the one subQ device. The distribution of force events, however, were different between these implant positions. The subM IPMs displayed force events that were more frequent in occurrence and of higher forces relative to resting force compared to the subQ IPM. Despite these differences, the majority of force events obtained from the baboons (both subM and subQ data) were centred around the resting force on the IPM, and higher force events were generally much less frequent. Humans may have different activity patterns on any given day compared to baboons, i.e. ratio of rest periods to activity periods. These activity patterns of humans warrant further investigation, since

they determine the distribution of force events on the implantable device and will therefore also be invaluable to assess the fatigue resistance of pacemakers. Mechanical design for fatigue should take into consideration the complete acquired distribution pattern of force events to ensure reliable fatigue capabilities of implantable devices.

The investigation towards the proposed concept of an interspecific transfer function indicated the feasibility of relating experimentally acquired normal force data from baboons to humans. More specifically, baboons are considered a good model for these types of evaluations based on various similarities to humans. This has made it possible to utilize the *in vivo* mechanical loading data (as well as other relevant data) from baboons to predict the subject-specific *in vivo* mechanical loads that will be experienced by a pectorally implanted cardiac pacemaker in humans (in the sub-muscular implant position).

The concept of an interspecific transfer function serves as basis for further improvement and validation. In addition, upon verification in future studies, this interspecific transfer function can be used with human parameters obtained by either non-invasive methods or approximation. Furthermore, validation of the transfer function will eliminate the need for any additional animal experiments.

6.2. Recommendations

Improvement of the *in vivo* force measurement system

Suggested improvements to this system involve the assembly of sensors onto the IPM, with the aim of eliminating or minimizing the effect of sterilization and sensor interaction. This can be achieved by removing the additional polyolefin gaskets around the sensors and by changing the way sensors are assembled onto the IPM, i.e. sensors should not be assembled on a common surface.

Improving the voltage-force conversion method includes the elimination or at least the quantification of any possible change in the calibrated voltage range (ΔV_{Ncal}) during changing experimental conditions. Improvements in experimental design can also improve the accuracy of the voltage-force conversion method. This includes keeping sensors loaded, at *in vivo* load levels, under similar temperature and humidity conditions before and after post-explant calibration procedures. It also includes keeping the sensors loaded during the sterilization procedure. The accuracy of the voltage-force conversion method can be further improved by developing a method to obtain a true zero-load sensor measurement to be used as reference measurement (instead of using the resting measurement as reference and then estimating the zero-load measurement).

Measurement of *in vivo* mechanical loading on implanted pacemakers

To ensure adequate healing of sub-coetaneous implants, it is suggested that a pocket for the device is created acceptably far from the incision and that sutures to facilitate proper anastomosis of corresponding layers of skin be used.

In order to conclude on the findings presented in this report pertaining to differences in mechanical loading of IPMs implanted in sub-muscular and sub-coetaneous positions, larger sample sizes for both implant positions are needed to ensure statistical significance of experimental findings.

In order to further characterize the mechanical loading environment of a pectorally implanted pacemaker in humans, this study needs to be supplemented with an investigation of the loading

magnitude and cyclic rate on a pacemaker as a result of externally applied forces from typical daily activities of a human. The resulting data should give a good indication of the mechanical loading conditions caused by sources of loading from outside the body. By combining such results with *in vivo* mechanical loading data obtained from this study and data from subsequent larger animal studies, more comprehensive strength requirements of pectorally implanted pacemakers can be formulated. These comprehensive strength requirements will enable optimizing the design of pectorally implanted pacemakers and improved estimation of device reliability, which will improve the reliability of the pacemaker mechanical structure.

Refinement and validation of interspecific transfer function

The interspecific transfer function can be refined by measuring additional parameters, such as the thickness of the muscle over the IPM ($t_{m,IPM}$), thickness of the muscle under the IPM (t_{mu}), optimal muscle fibre length (L_m^0), the pennation angle of the muscle (θ) as well as parameters relating to the compliance of structures surrounding the IPM. In addition, based on the non-zero resting force measured by implanted IPMs during eStim experiments, it is also suggested that the resting in-line force be determined. Furthermore, extracting detailed information of humans and baboons from medical images using specialized software will allow accurate and repeatable measurements of various parameters, such as ψ_1 and ψ_2. Improvements in the correlations used in the concept can be made by (1) increasing the sample size, (2) including additional relevant parameters previously assumed to have a negligible effect on the total normal force on the IPM (F_{NT}), (3) transforming certain parameters known for their nonlinear influence on F_{NT} in order to make them detectable with linear regression analyses and (4) accommodating for factors shown to possibly have caused variability.

References

Anonymous.
2006
Human Weight
Retrieved 21 May, 2008, from http://www.articleworld.org/index.php/Human_weight.

Anonymous.
2007
Chacma Baboon (Papio ursinus)
Retrieved 21 May, 2008, from http://www.theprimata.com/papio_ursinus.html.

Antretter H, Colvin J, Schweigmann U, Hangler H, Hofer D, Dunst K, Margreiter J and Laufer G.
2003
Special Problems of Pacing in Children.
Indian Pacing and Electrophysiology Journal, 3(1): 23-33.

Bachus KN, DeMarco AL, Judd KT, Horwitz DS and Brodke DS.
2006
Measuring contact area, force, and pressure for bioengineering applications: Using Fuji Film and TekScan systems.
Medical Engineering & Physics, 28(5): 483-488.

Biewener A.
2000
Scaling of terrestrial support: Differing solutions to mechanical constraints of size. pp. 51-65 In: Brown, JH and West, GB. eds. Scaling in Biology. New York, Oxford University Press.

Binder-Macleod SA, Lee SCK, Russ DW and Kucharski LJ.
1998
Effects of activation pattern on human skeletal muscle fatigue.
Muscle & Nerve, 21(9): 1145-1152.

Bobet J and Stein RB.
1998
A simple model of force generation by skeletal muscle during dynamic isometric contractions.
Biomedical Engineering, IEEE Transactions on, 45(8): 1010-1016.

Brimacombe JM, Wilson DR, Hodgson AJ, Ho KCT and Anglin C.
2009
Effect of Calibration Method on Tekscan Sensor Accuracy.
Journal of Biomechanical Engineering, 131(3): 034503-4.

Brinker J and Midei MG.
2005
Techniques of pacemaker implantation and removal. pp. 196-264 In: Ellenbogen, K and Wood, M. eds. Cardiac pacing and ICDs. Malden, Mass., Blackwell.

Brown JH, West GB and Enquist BJ.
2000
Scaling in biology: Patterns and processes, causes and consequences. pp. 1-24 In: Brown, JH, West, GB and Enquist, BJ. eds. Scaling in biology. New York, Oxford University Press.

Cannom DS and Prystowsky EN.
2004
Evolution of the Implantable Cardioverter Defibrillator.
Journal of Cardiovascular Electrophysiology, 15(3): 375-385.

Cleland JGF, Daubert JC, Erdmann E, Freemantle N, Gras D, Kappenberger L and Tavazzi L.
2005
The Effect of Cardiac Resynchronization on Morbidity and Mortality in Heart Failure.
New England Journal of Medicine, 352(15): 1539-1549.

Costeas XF, Strembelas PG, Markou DX, Stefanadis CI and Toutouzas PK.
2000
Subpectoral Cardioverter-Defibrillator Implantation Using a Lateral Approach.
Journal of Interventional Cardiac Electrophysiology, 4: 611-619.

Dennerlein JT, Diao E, Mote CD and Rempel DM.
1998
Tensions of the flexor digitorum superficialis are higher than a current model predicts.
Journal of Biomechanics, 31(4): 295-301.

Eng CM, Smallwood LH, Rainiero MP, Lahey M, Ward SR and Lieber RL.
2008
Scaling of muscle architecture and fiber types in the rat hindlimb.
Journal of Experimental Biology, 211(14): 2336-2345.

Erdemir A, McLean S, Herzog W and van den Bogert AJ.
2007
Model-based estimation of muscle forces exerted during movements.
Clinical Biomechanics, 22(2): 131-154.

Finni T, Komi PV and Lukkariniemi J.
1998
Achilles tendon loading during walking: application of a novel optic fiber technique.
European Journal of Applied Physiology and Occupational Physiology, 77(3): 289-291.

Fleagle JG.
1999
Primate adaption and evolution.
2nd, San Diego, Academic Press.

Friedman R.
1992
Pacemakers in Children.
Texas Heart Institute Journal, 19(3): 178-184.

Furman S.
2002
The Future of the Pacemaker.
Pacing and Clinical Electrophysiology, 25(1): 1-2.

Furman S, Curtis AB and Conti JB.
2001
Recognition and Correction of Subcuticular Malposition of Pacemaker Pulse Generators.
Pacing and Clinical Electrophysiology, 24(8): 1224-1227.

Garner BA and Pandy MG.
2000
Musculoskeletal model of the upper limb based on the Visible Human Male dataset.
Computer Methods in Biomechanics and Biomedical Engineering, 4: 99-126.

Gold MR, Peters RW, Johnson JW and Shorofsky SR.
1996
Complications associated with pectoral cardioverter-defibrillator implantation: Comparison of subcutaneous and submuscular approaches.
Journal of the American College of Cardiology, 28(5): 1278-1282.

Hamilton-Wright A and Stashuk DW.
2005
Physiologically based simulations of clinical EMG signals.
IEEE Transactions on biomedical engineering, 52(2): 171-183.

Hill A.
1938
The heat of shortening and the dynamic constants of muscle.
Proceedings - Royal Society of London,(126): 136-195.

Holzbaur KRS, Murray WM and Delp SL.
2005
A Model of the Upper Extremity for Simulating Musculoskeletal Surgery and Analyzing Neuromuscular Control.
Annals of Biomedical Engineering, 33(6): 829-840.

Holzbaur KRS, Murray WM, Gold GE and Delp SL.
2007
Upper limb muscle volumes in adult subjects.
Journal of Biomechanics, 40(4): 742-749.

Huijing PA.
1995
Parameter interdependence and success of skeletal muscle modelling.
Human Movement Science, 14(4-5): 443-486.

Huxley AF.
1957
Muscle contraction and theories of contraction.
Progress in Biophysics and Biophysical Chemistry, 7: 225-318.

Jeffrey K and Parsonnet V.
1998
Cardiac Pacing, 1960–1985 : A Quarter Century of Medical and Industrial Innovation.
Circulation, 97(19): 1978-1991.

Kenny T.
2005
The nuts and bots of cardiac pacing. Malden, Mass., Blackwell Futura.

Kistler PM, Eizenberg N, Fynn SP and Mond HG.
2004
The Subpectoral Pacemaker Implant: It Isn't What It Seems.
Pacing and Clinical Electrophysiology, 27: 361-364.

Knudson D.
2007
Fundamentals of Biomechanics.
2nd, New York, Springer.

Kron J, Herre J, Renfroe EG, Rizo-Patron C, Raitt M, Halperin B, Gold M, Goldner B, Wathen M, Wilkoff B, Olarte A and Yao Q.
2001
Lead- and device-related complications in the Antiarrhythmics Versus Implantable Defibrillators Trial.
American Heart Journal, 141(1): 92-98.

Lieber R and Fridén J.
2000
Functional and clinical significance of skeletal muscle architecture.
Muscle & Nerve, 23(11): 1647-1666.

Llewellyn MJ, Bennett DH, Shearer KS and Slaven YM.
1989
The Impact of a Manufacturer's Revision of Pacemaker Service Life on the Workload of a Large Pacing Center.
Pacing and Clinical Electrophysiology, 12(7): 1014-1017.

Luo ZP, Berglund LJ and Kai-Nan A.
1998
Validation of F-Scan pressure sensor system: A technical note.
Journal of Rehabilitation Research and Development, 35(2): 186-191.

Maisel WH, Moynahan M, Zuckerman BD, Gross TP, Tovar OH, Tillman D-B and Schultz DB.
2006
Pacemaker and ICD Generator Malfunctions: Analysis of Food and Drug Administration Annual Reports.
Journal of the American Medical Association, 295(16): 1901-1906.

Maisel WH, Sweeney MO, Stevenson WG, Ellison KE and Epstein LM.
2001
Recalls and Safety Alerts Involving Pacemakers and Implantable Cardioverter-Defibrillator Generators.
Journal of the American Medical Association, 286(7): 793-799.

Marden JH and Allen LR.
2002
Molecules, muscles, and machines: Universal performance characteristics of motors.
Proceedings of the National Academy of Sciences of the United States of America, 99(7): 4161-4166.

Martinelli L, Hurschler C and Rosenbaum D.
2006
Comparison of capacitive versus resistive joint contact stress sensors.
Clinical Orthopaedics and related research, 447: 214-220.

Moses KP, Banks JC, Nava BN and Petersen D.
2005
Atlas of clinical gross anatomy. Spain, Elsevier.

Navallas J, Malanda A, Gila L, Rodriguez J and Rodriguez I.
2007
A new muscle architecture model with non-uniform distribution of muscle fibre types.
International Journal for Biomedical Sciences, 2(4): 244-248.

Otto J, Brown T and Callaghan J.
1999
Static and dynamic response of a multiplexed-array piezoresistive contact sensor.
Experimental Mechanics, 39(4): 317-323.

Pasquet B, Carpentier A, Duchateau J and Hainaut K.
2000
Muscle fatigue during concentric and eccentric contractions.
Muscle & Nerve, 23(11): 1727-1735.

Peterson OH.
2007
Human Physiology.
5th, Malden, Mass., Blackwell Publishing Inc.

Powell PL, Roy RR, Kanim P, Bello MA and Edgerton VR.
1984
Predictability of skeletal muscle tension from architectural determinations in guinea pig hindlimbs.
Journal of Applied Physiology, 57(6): 1715-1721.

Ratner B and Bryant S.
2004
Biomaterials: Where we have been and where we are going.
Annual Review of Biomedical Engineering, 6: 41-75.

Robinson V.
2005
Finding alternatives: an overview of the 3Rs and the use of animals in research.
School Science Review, 87(319): 111-114.

Sherwood L.
2004
Human physiology: From cells to systems.
5th, London, Brooks/Cole.

Shmulewitz A, Langer R and Patton J.
2006
Convergence in biomedical technology.
Nature Biotechnology, 24(3): 277-280.

Spitzer V, Ackerman MJ, Scherzinger AL and Whitlock D.
1996
The Visible Human Male: a technical report.
Journal of the American Medical Informatics Association, 3: 118 - 130.

Swatland HJ.
1994
Structure and Development of Meat Animals and Poultry. Florida, CRC Press.

Tekscan.
2005
Tekscan Flexiforce User manual (Revision F).
Tekscan Inc., South Boston, MA.

Tekscan.
2008
Tekscan Flexiforce: Frequently Asked Questions
Retrieved 28 May, 2008, from http://www.tekscan.com/flexiforce/flexifaq.html.

Van De Graaf KM.
2002
Human Anatomy.
6th, Boston, McGraw-Hill.

Van den Bogert AJ, Gerritsen KGM and Cole GK.
1998
Human muscle modelling from a user's perspective.
Journal of Electromyography and Kinesiology, 8(2): 119-124.

Van Loocke M, Lyons CG and Simms CK.
2008
Viscoelastic properties of passive skeletal muscle in compression: Stress-relaxation behaviour and constitutive modelling.
Journal of Biomechanics, 41(7): 1555-1566.

Vaughan CL, Davis BL and O'Connor JC.
1992
Dynamics of human gait. Champaign, IL, Human Kinetics Publishers.

Viano DC and King AI.
2000
Biomechanics of chest and abdomen impact. pp. 398-409 In: Bronzino, JD. eds. The biomedical engineering handbook. Boca Raton, CRC Press LLC.

Vining GG.
1998
Statistical methods for engineers. London, Brooks/Cole.

Voisin JL.
2006
Clavivle, a neglected bone: morphology and relation to arm movements and shoulder architecture in primates.
The Anatomical Record, 288A: 944-953.

Ward SR and Lieber RL.
2005
Density and hydration of fresh and fixed human skeletal muscle.
Journal of Biomechanics, 38(11): 2317-2320.

Wild DM, Fisher JD, Kim SG, Ferrick KJ, Gross JN and Palma EC.
2004
Pacemakers and Implantable Cardioverter Defibrillators: Device Longevity Is More Important Than Smaller Size: The Patient's Viewpoint.
Pacing and Clinical Electrophysiology, 27(11): 1526-1529.

Wilkoff BL.
2006
Pacemaker and ICD Malfunction--An Incomplete Picture.
Journal of the American Medical Association, 295(16): 1944-1946.

Wilson DC, Niosi CA, Zhu QA, Oxland TR and Wilson DR.
2006
Accuracy and repeatability of a new method for measuring facet loads in the lumbar spine.
Journal of Biomechanics, 39(2): 348-353.

Winby CR, Lloyd DG and Kirk TB.
2008
Evaluation of different analytical methods for subject-specific scaling of musculotendon parameters.
Journal of Biomechanics, 41(8): 1682-1688.

Zajac FE, Neptune RR and Kautz SA.
2003
Biomechanics and muscle coordination of human walking: Part II: Lessons from dynamical simulations and clinical implications.
Gait & Posture, 17(1): 1-17.

Appendices

A. Voltage-force conversion method for force sensors

A.1. Overview

Converting the sensor voltage data (V_N) to sensor force data (F_N),using the most suited post-explant calibration curves, was limited by the *in vivo* calibrated sensor voltage (ΔV_{Ncal}) and zero-load offset voltage (V_{Noff}) that could not be verified *in vivo*. Furthermore, median filtering of sensor voltage data only removed maximum RF noise spikes (not minimum RF noise spikes). For this reason a voltage-force conversion was developed which considered these limitations.

The voltage-force conversion method that was developed applied a custom high-pass filter to the sensor voltage data to remove minimum noise peaks. In addition, it approximated the zero-load offset voltage ($V_{Noff} \cong F_{N0} = 0$) per sensor per experiments, using the sensor voltage obtained when the baboon was at rest (V_{Nrest}) as reference for each experiment.

By combining Eq. (19) and Eq. (23), which were derived in the subsequent sections, the final equation that yielded an approximated sensor force data point (F_N) for experiment *m* that formed part of the series of experiments *d,* was,

$$F_N = f_2\left(V_N - V_{Nvmin}\,{}^{series\,,d}_{exp\,,m}\right) \tag{13}$$

This equation required the following inputs: the measured sensor voltage data point (V_N), the valid minimum sensor voltage over the whole series of experiments, but specific to that particular experiment where V_N was measured ($V_{Nvmin}\,{}^{series\,,d}_{exp\,,m}$) and the 5th order polynomial function that described the most suited calibration curve of that particular sensor that was offset to the origin (f_2).

The voltage-force conversion method (consisting of the formulation of the custom high-pass filter and the derivation of Eq. (13)) was developed by performing the following steps:

A.2 Custom high-pass filter for obtaining the valid minimum sensor measurement per experiment
A.3 Assumptions regarding sensitivity and sensor voltage offset
A.4 Adjustment of *in vivo* sensor data for use with post-explant calibration curves
A.5 Utilizing resting sensor voltage to accommodate for variation of valid minimum sensor voltage.

These steps are numbered according to the subsequent sections in which further explanation is presented.

A.2. Custom high-pass filter for obtaining the valid minimum sensor measurement per experiment

The voltage-force conversion method had to compensate for the drift of the unknown zero-load offset voltage (V_{Noff}), expected to change for each experiment. However, the value of V_{Noff} could not be verified *in vivo*. It was therefore required to approximate V_{Noff} per sensor per experiment, which was essential for determining the actual force on the sensor (F_N) corresponding to the sensor measurement (V_N).

Using the minimum sensor voltage (V_{Nmin}) measured during an experiment to approximate the V_{Noff} was not deemed viable, because the possibility existed that signal noise was still present after filtering (Section 3.6.1). The presence of minimum noise spikes in the V_N signal implied that the minimum measured sensor (V_{Nmin}) was less than the actual (or valid) minimum sensor voltage (V_{Nvmin}) producible by the sensor so that,

$$V_{Nmin} < V_{Nvmin} \tag{14}$$

Therefore, V_{Nmin} could not necessarily be used to approximate V_{Noff}, because a value for V_{Nmin} caused by minimum noise spikes would cause errors and inconsistencies when calculating F_N. A minimum sensor voltage had to be determined, which was not a result of noise, but a valid sensor measurement, i.e. V_{Nvmin}.

Due to the high sampling rate of the *in vivo* normal force measurement system (1000 Hz), it was assumed that the number of data points in the lower sensor voltage ranges caused by minimum noise spikes (present in the data after filtering) was minimal. To establish the presence of these infrequently occurring data points, the following example was considered: the data plotted in Figure 48 was obtained from a single sensor during a typical experiment on a conscious baboon. Sorting the V_N data points in an ascending order (Figure 48a) and plotting a histogram of the same data (Figure 48c) revealed that certain V_N data points at the lowest values occurred very infrequently. Furthermore, a sharp decrease in V_N was observed from the level where the majority of V_N data points occurred to where some of these lowest values occurred. Percentile values of the V_N data (V_{Nperc}) were plotted in 0.25 percentile increments on these figures – the diamonds plotted in Figure 48b and Figure 48d. Considering the all the different values of V_{Nperc}, a point can be observed where V_{Nperc} drops significantly compared to the preceding values of V_{Nperc} in the direction of decreasing percentile increments. This could be interpreted as a few data points of V_N that occurred very infrequently or as minimum spikes caused by noise.

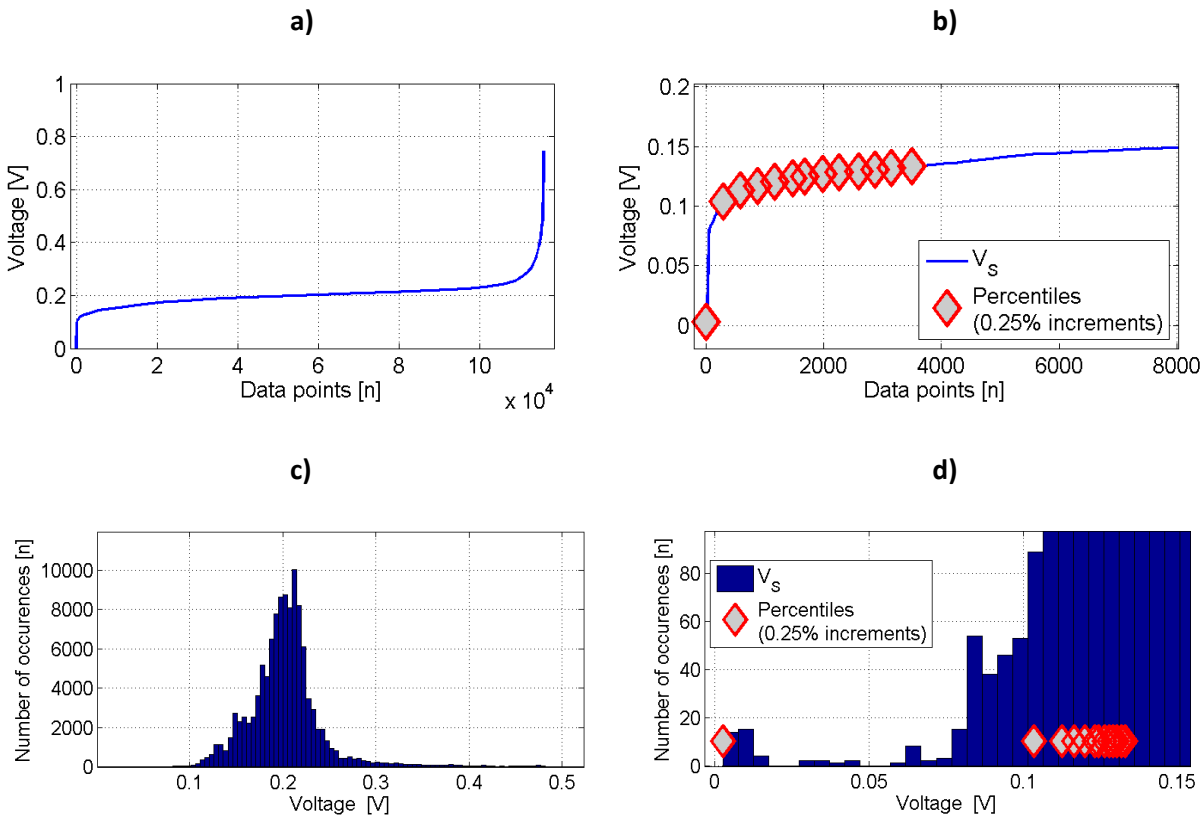

Figure 48: Sensor voltage (V_N) data from of a typical experiment indicating, a) the V_N data sorted in an ascending order, b) a zoomed view of the V_N data sorted in an ascending order, indicating the 0^{th} to the 3^{rd} percentile in 0.25 percentile increments, c) a histogram of the V_N data points and d) a zoomed view of the histogram of the V_N data points, indicating the 0^{th} to the 3^{rd} percentile in 0.25 percentile increments.

Comparing these different values of V_{Nperc} for the same sensor between different experiments within the same series is shown in Figure 49. It can be seen that 0^{th} percentile ($V_{Nperc\text{-}P0}$ or V_{Nmin}) did not necessarily follow the same trends as the other corresponding percentile voltages, e.g. $V_{Nperc\text{-}P0.50}$, $V_{Nperc\text{-}P1.25}$ etc. Similar to the values of V_{Nperc} shown in Figure 48b and Figure 48d, this could also be interpreted as a few data points of V_N that occurred very infrequently or as minimum spikes caused by noise. This was a further indication of the possible presence of noise in the V_N data. Therefore, it was not clear whether these few data points observed in the lower voltage range were caused by a physical load on the IPM or whether this was a result of an unknown source of noise. To accommodate for this uncertainty, certain steps were taken in an attempt to eliminate this uncertainty in order to determine a reasonable value of V_{Nvmin}, as described below.

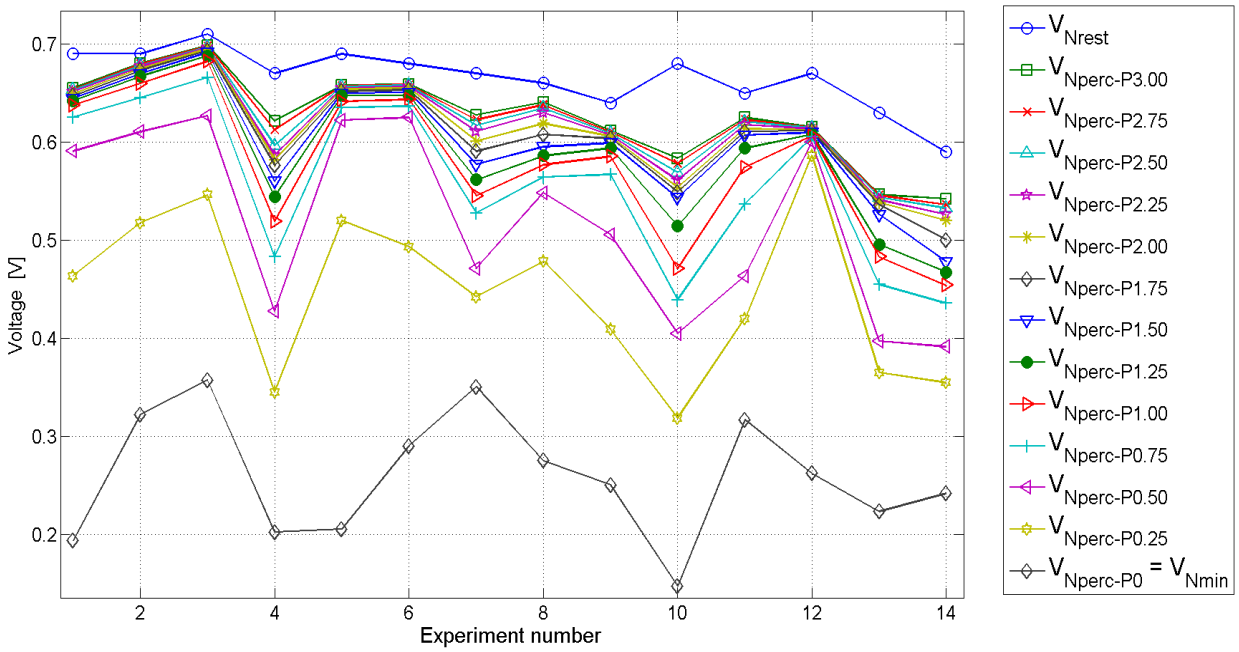

Figure 49: Lower percentiles of a single sensor over a whole series of experiments. The percentile values are indicated in 0.25 percentile increments.

The V_{Nvmin} per sensor, per experiment, was obtained as explained below and as shown in Figure 50:

1. All of the V_N data points were sorted in an ascending order;
2. V_{Nperc} was calculated for the 0th to 3rd percentile in 0.25 percentile increments;
3. The calculated V_{Nperc} was plotted against the corresponding percentile increment (diamonds);
4. The slope of the straight line between every pair of adjacent percentile increments $\left(\frac{\Delta(V_{Nperc})}{\Delta(perc)}\right)$, was calculated;
5. A conservative filter threshold (λ) was chosen for $\frac{\Delta(V_{Nperc})}{\Delta(perc)}$ to distinguish between V_N data points that were considered valid and those considered invalid (i.e. due to the possible presence of noise);
6. The percentile located between $\frac{\Delta(V_{Nperc})}{\Delta(perc)} < \lambda$ and $\frac{\Delta(V_{Nperc})}{\Delta(perc)} > \lambda$ was identified as V_{Nvmin}.

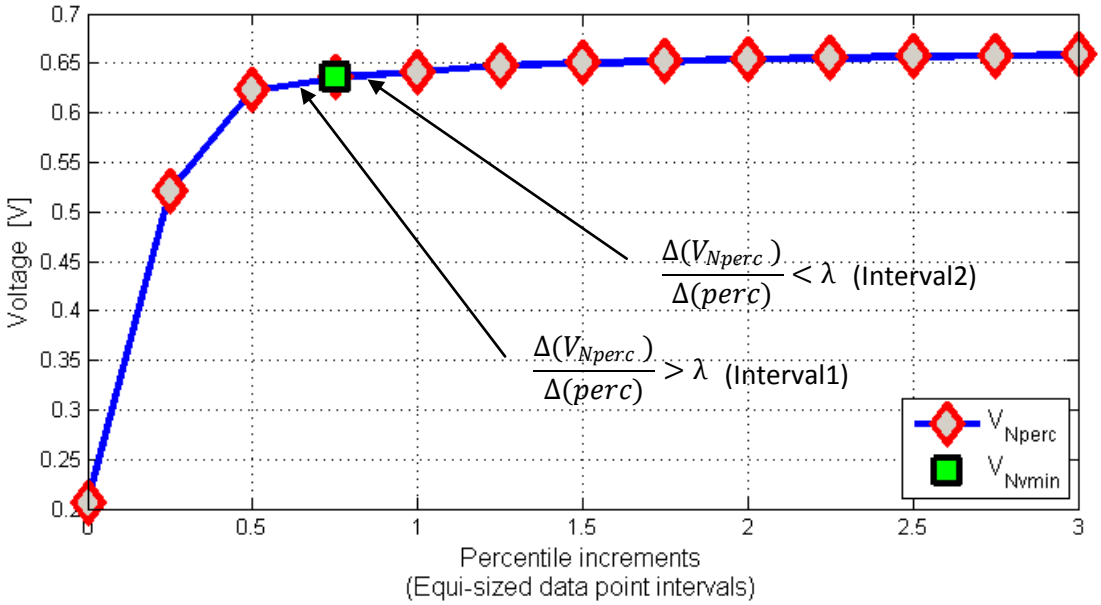

Figure 50: Lower range percentiles of sensor voltages against percentile increments for a typical experiment, with data points between each percentile increment being equal. The 0th-percentile to 3rd-percentile are shown, as well as the identified valid minimum sensor voltage for the monitor event

In order to show that the resulting V_{Nvmin} obtained from this procedure yielded a value for V_{Nvmin} with a higher certainty of not being noise, consider two adjacent, equi-sized, data point intervals (Figure 50) from the lowest 3% of V_N data points, e.g. Interval 1 and Interval 2. If the value of $\frac{\Delta(V_{Nperc})}{\Delta(perc)}$ for Interval 2 is smaller than for Interval 1 then the following is revealed:

- There was an increased rate in the drop of V_N over the same number of data points from Interval 2 to Interval 1;
- If V_{Nmin} (or $V_{Nperc\text{-}P0}$) and data points close to V_{Nmin} were indeed noise, then there was an increased probability that some of the data points in Interval 1 were noise, compared with those in Interval 2.

The value of $\frac{\Delta(V_{Nperc})}{\Delta(perc)}$ is dependant on the size of the percentile increments and is only comparable if the size of the considered percentile increments remain the same, which was done accordingly when applying this method to the V_N data. A conservative λ of 0.05 was chosen which was found to be practical for all experiments, based on results that were obtained.

This method of removing noise from the signal was effectively a custom high-pass filter. Following this approach, the V_{Nvmin} was determined for each sensor during each experiment.

A.3. Assumptions regarding sensitivity and sensor voltage offset

The exact ΔV_{Ncal} and V_{Noff} of a sensor could not be verified *in vivo*, since it was not possible to perform a calibration procedure on a sensor *in vivo*. Therefore, these parameters had to be approximated based on assumptions about sensor behaviour (Section 3.2.1.1) and varying experimental conditions which influenced these parameters. These assumptions were:

1. Each IPM experienced unique loading conditions, but similar temperatures during all *in vivo* experiments;
2. The change of ΔV_{Ncal} and V_{Noff} was unique for every sensor considered and were considered to be independent of each other;
3. Sensor conditioning prior to implantation (4 weeks) and during the healing period (6 weeks) was deemed sufficient for ΔV_{Ncal} and V_{Noff} to have reached stabilization prior to commencement of the *in vivo* experiments;
4. The change in ΔV_{Ncal} from the first experiments performed to the most suited post-explant calibration curve obtained was sufficiently small to use the ΔV_{Ncal} obtained from the post-explant calibration curve (per sensor) for all *in vivo* experiments;
5. The total resting force on the principal surface of the IPM, F_{NTrest} (and therefore also resting force per sensor, F_{Nrest}) remained constant during a single experiment (<5 min) – the acute loadings on the sensors were not sustained long enough to cause a significant drift of V_{Noff};
6. The F_{NTrest}, (and therefore also F_{Nrest}) remained constant for a whole series of experiments, since experimental loading conditions were not expected to change significantly (<8 days for conscious activity and <3 hours for experiments on anaesthetized baboons) – however, the V_{Noff} was expected to drift between different experiments under constant loading due to the intrinsic sensor behaviour;
7. The F_{NTrest} (and therefore also F_{Nrest}) decreased after each sequential series of experiments, due to changing experimental conditions. This was assumed due to the expected change of the "state" of the muscle, i.e. An initial decrease due to the expected loss of conscious muscle tone upon anaesthetization, a further decrease was expected due to the removal of connective tissue surrounding and skin overlying the muscle, and a further decrease due to a complete unloading of the sensors upon explantation;
8. For sensors conditioned to experimental loading and temperature conditions, the stabilization of V_{Noff} occurred at a sufficiently fast rate to assume its stability prior to commencement of a series of experiments (between 10-20 minutes (Otto et al. 1999));
9. The variability of V_{Noff} was accurately reflected in the reference V_{Nrest} measurements.

A.4. Adjustment of *in vivo* sensor data for use with post-explant calibration curves

Consider the curves illustrated in Figure 51 and the subsequent explanation.

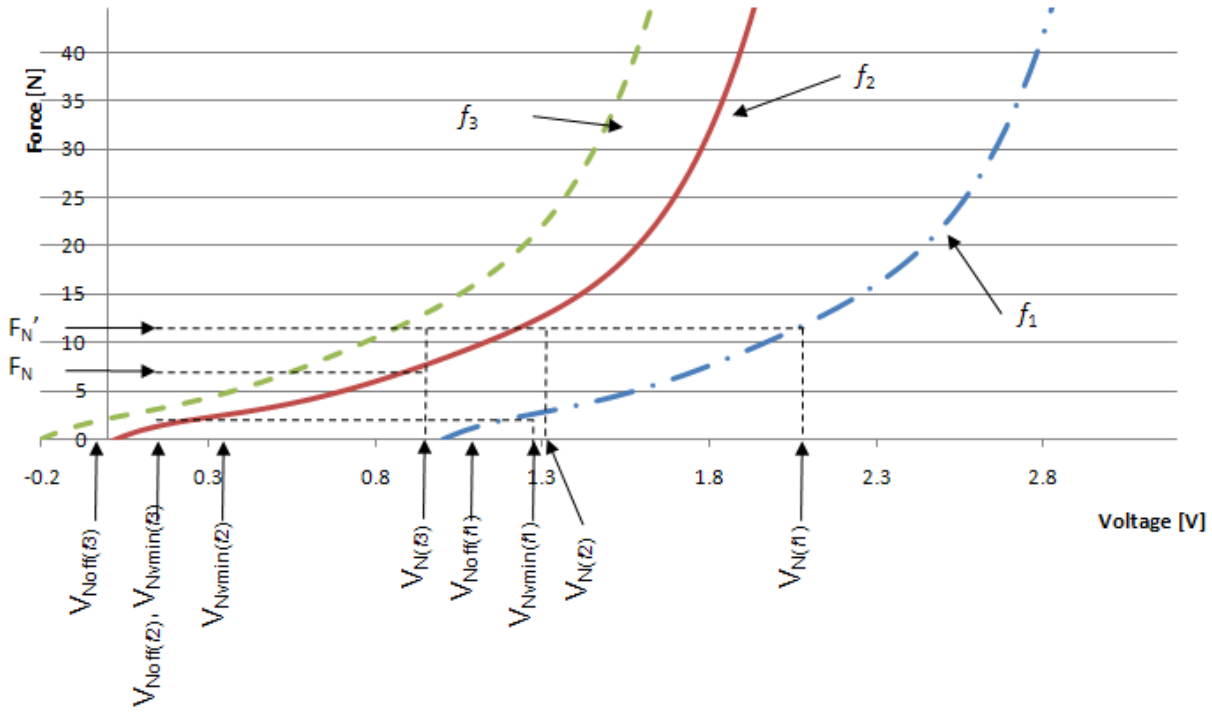

Figure 51: Adjusting an arbitrary in vivo sensor voltage data point (V_N) to obtain its corresponding approximated sensor force data point (F_N). For purposes of illustration, the scale of this figure is exaggerated.

If it were possible to obtain a calibration curve for the *in vivo* sensor whilst implanted, it would yield the raw calibration curve, f_1. An arbitrary *in vivo* sensor voltage measurement, $V_{N(f1)}$, would lie on f_1, and a value of the actual force applied to the sensor, F_N', could be obtained as follows:

$$F_N' = f_1(V_{N(f1)}) \tag{15}$$

However, the only curve available to approximate this unknown calibration curve was the post-explant calibration curve, f_2, which was offset to the origin by $V_{Noff(f2)}$. As assumed in the preceding section, the change of ΔV_{Ncal} between the *in vivo* experiments and the post-explant calibration remained constant. Therefore, $V_{N(f1)}$ could simply be offset by $V_{Noff(f1)}$, which results in $V_{N(f2)}$ on f_2, expressed as follows:

$$F_N' = f_2(V_{N1} - V_{Noff\,1}) = f_2(V_{N2}) \tag{16}$$

But $V_{Noff(f1)}$ could not be verified *in vivo*, and therefore the valid minimum of the acquired sensor data, $V_{Nvmin(f1)}$ (Section A.5 below), was used to approximate $V_{Noff(f1)}$:

$$V_{Noff\,(f1)} \cong V_{Nvmin\,(f1)} \tag{17}$$

By offsetting $V_{N(f1)}$ by $V_{Nvmin(f1)}$, the $V_{Nvmin(f1)}$ was used as the zero-load voltage offset, instead of $V_{Noff(f1)}$. However, adjusting the sensor data point $V_{N(f1)}$ by using $V_{Nvmin(f1)}$ yielded the actual force measured by the sensor which lies on an unknown adjusted calibration curve, f_3, which only yielded the actual force when calculated as follows,

$$F_N{}' = f_3\left(V_{N1(f1)} - V_{Noff\,1(f1)}\right) = f_3\left(V_{N3(f3)}\right) \tag{18}$$

Using only available data, $V_{N3(f3)}$ was inserted directly into f_2 to obtain the measured value of the actual force (F_N),

$$F_N = f_2\left(V_{N(f1)} - V_{Nvmin\ (f1)}\right) = f_2\left(V_{N(f3)}\right) \tag{19}$$

When Eq. (19) is rewritten in terms of f_2, the actual force measured is,

$$F_N{}' = f_2\left(V_{N(f2)}\right) \tag{20}$$

Therefore, the error between the actual and measured force was obtained by subtracting Eq. (20) from Eq. (19),

$$F_{Nerr} = F_N^{'} - F_N = f_2\left(V_{N(f2)}\right) - f_2\left(V_{N(f3)}\right) \tag{21}$$

F_N was always equal to F_N' or underestimated, because the following condition was expected for all experiments performed,

$$V_{Noff\ (f1)} \leq V_{Nvmin\ (f1)} \tag{22}$$

Despite the error in estimating F_N', based on the stated assumptions and available data, this approach provided a reasonable approximation of F_N'. The size of F_{Nerr} (i.e. the accuracy) depended on how well $V_{Nvmin(f1)}$ approximated $V_{Noff(f1)}$.

With this adjustment of the *in vivo* sensor data for use with most suited post-explant calibration curves, as shown in Eq. (19), the next step was to approximate the absolute values of F_N data in order to compare forces measured amongst different sensors, amongst different experiments within the same series and amongst experiments from different series.

A.5. Utilizing resting sensor voltage to accommodate for variation of valid minimum sensor voltage

In order to obtain absolute force measurements (as opposed to relative force measurements), zero-loads need to be identified. The V_{Nvmin} could not be used as a zero-load measurement, since it depended on the specific loads exerted on the sensor during an experiment – experimental loading was uncontrolled and unregulated. In other words, the minimum force exerted on a sensor per experiment was not repeatable. A measurement that was repeatable between experiments needed to be used.

Considering a series of experiments, the most repeatable *in vivo* measurement was considered to be V_{Nrest}, since the F_{Nrest} was reasonably expected to remain constant for the whole series of experiments – even though F_{Nrest} was unknown. The V_{Nrest} was expected to only change minimally due to intrinsic sensor drift. Therefore, approximating the V_{Noff} required the use of a repeatable reference measurement, namely V_{Nrest}. A method was formulated to do this, which utilized the distance of V_{Nvmin} relative to V_{Nrest}, defined as the distance "below rest", or ΔV_{Nbr}. Considering the assumption of a constant ΔV_{Ncal} for all *in vivo* experiments (Section A.3), it followed that the maximum ΔV_{Nbr} of all experiments of a series was valid for each experiment within that series. Therefore, subtracting the maximum ΔV_{Nbr} of a series of experiments from the repeatable reference measurement (V_{Nrest}) of a single experiment within that series, a V_{Nvmin} specific for that experiment was obtained, even if that value was not measured during that particular experiment. When the V_{Nvmin} for each experiment within this series was similarly determined, each experiment within that particular series yielded an equal value of F_{Nrest} – in line with the assumption of a constant F_{Nrest} for all experiments within that series. Mathematically, this method was expressed for an arbitrary experiment *m*, in a series of experiments *d*,

$$V_{Nvmin}{}_{exp,m}^{series,d} = V_{Nrest}{}_{exp,m}^{series,d} - \max[\Delta V_{Nbr}]_{exp,all}^{series,d} \quad (23)$$

Applying this method to two arbitrary experiments within the same series of experiments, *p* and *q*, with unknown raw *in vivo* calibration curves f_{1p} and f_{1q} and different V_{Nrest} and V_{Nvmin} respectively, is demonstrated in Figure 52. These two calibration curves were offset by the V_{Nvmin} calculated in Eq (23) for each experiment, to obtain f_{3p} and f_{3q}, which are both equal to f_3 as indicated in the figure.

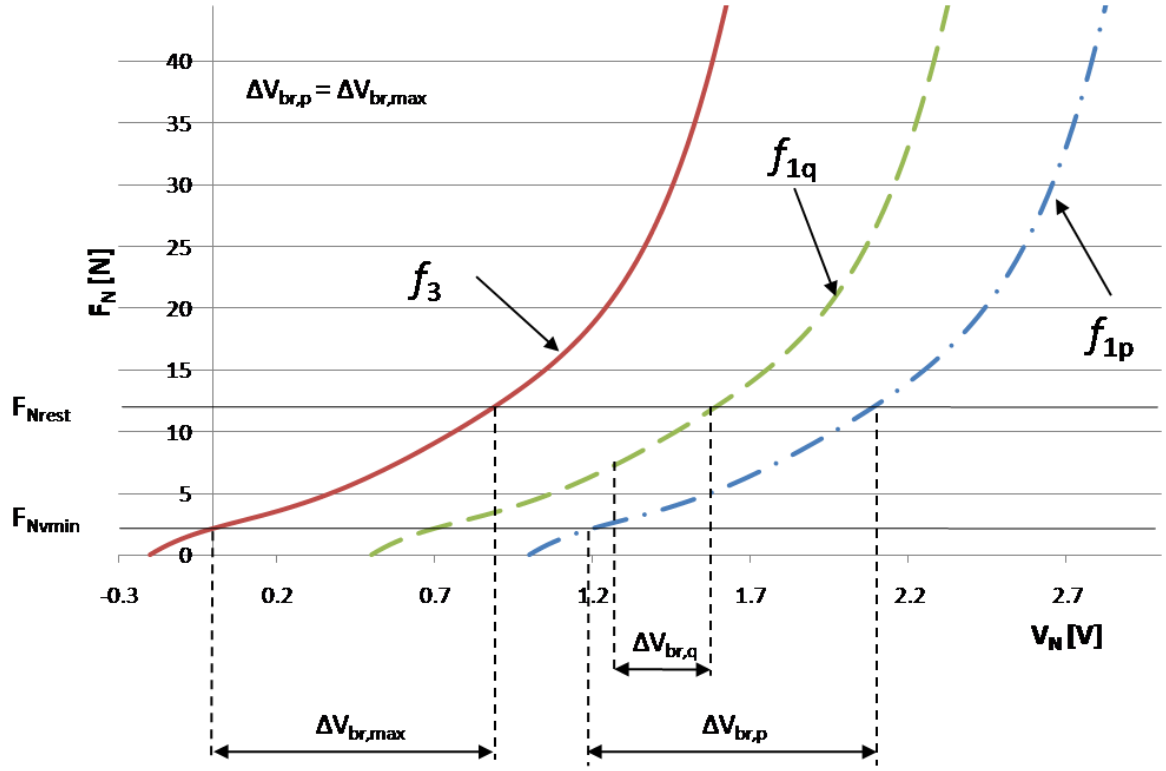

Figure 52: Demonstrating the method for utilizing the maximum distance from the valid minimum sensor voltage (V_{Nvmin}) relative to the resting sensor voltage (V_{Nrest}) for comparable force estimations (F_N) between experiments in the same series. The "below rest" interval (ΔV_{Nbr}) for each experiment is shown, from which the largest interval was chosen to calculate V_{Nvmin} for each, and offset to obtain $f_3 = f_{3p} = f_{3q}$.

This method provided a means to accommodate for the experiments where a zero-load force was not reached and ensured that force measurements between different experiments within a series were comparable. It relied on a zero-load (or a minimum load that was repeatedly reached) exerted on a sensor at least at one instance during a whole series of experiments. Considering the large amount of data planned to be recorded and the various activities performed, achieving of zero-load during the in vivo experiments was considered to be a reasonable assumption. This also implied that not only were the force measurements comparable between experiments from the same series, but also amongst different series of experiments. Furthermore, it meant that these force measurements obtained reflected the absolute force measured by the sensors.

B. *In vivo* morphometric and force measurements

Table 11: In vivo morphometric measurements and force results from experiments on conscious baboons, range of motion, 76 mm Chatillon and eStim experiments.

Description	Test subject information					
Morphometric measurements						
Baboon #	447		449		575	
Implant mass [kg]	21		21.5		19.3	
Explant mass [kg]	24.7		23		20.7	
Implant date [in 2008]	15-May	15-May	15-May	15-May	15-May	15-May
Explant date [in 2008]	28-Jul	03-Jun	26-Jun	24-Jul	24-Jul	24-Jul
Implant position	SubM	SubQ	SubQ	SubM	SubM	SubQ
Implant side	Right	Left	Right	Left	Right	Left
IPM device #	SN068	SN064*	SN071*	SN069	SN076†	SN074†
M_m [g]$	82.0	154.0	166.0	125.0	149.0	164.0
V_m [cm^3]$	70.0	135.0	150.0	120.0	135.0	140.0
ρ_m [g/cm^3]‡	1.171	1.141	1.107	1.042	1.104	1.171
L_m^{meas} [mm]	150.0	150.0	180.0	170.0	195.0	170.0
$w_{m,IPM}$ [mm]	92.5	95.0	80.0	90.0	85.0	95.0
$w_{m,cb}$ [mm]	42.5	60.0	50.0	47.5	5.0	52.5
$t_{m,cb}$ [mm]	5.0	4.0	6.5	4.0	4.5	3.5
PCSA [cm^2]**	7.7	14.8	13.7	11.6	11.4	13.5
Experiments on conscious baboons (conscious exp.)						
Number of experiments [n]	20	-	-	19	10	14
Duration of experiments [min:sec]	76:41	-	-	78:55	38:44	69:09
F_{NTmax} [N]	31.6	-	-	137.7	62.3	24.9
F_{NTrest} [N]	14.3	-	-	23.7	28.7	17.6
$F_{NTmean} \pm F_{NTstd}$ [N]	14 ± 1.3	-	-	24.6 ± 3.4	27.3 ± 3.2	17.3 ± 1.5
$F_{NTmedian}$ [N]	14.2	-	-	24.2	27.8	17.3
$P_{NTmedian}$ [kPa]††	5.5	-	-	9.5	10.8	6.8
Range of motion experiments (ROM)						
F_{NTmax} [N]	39.1	-	-	47.6	17.1	20.5
F_{NTrest} [N]	9.8	-	-	16.3	14.1	15.6
$F_{NTmean} \pm F_{NTstd}$ [N]	10.9 ± 5.1	-	-	17.7 ± 7	14.1 ± 0.6	15.7 ± 1.5
$F_{NTmedian}$ [N]	9.6	-	-	15.9	14.0	15.7
$P_{NTmedian}$ [kPa]††	3.8	-	-	6.2	6.2	5.5
76 mm Chatillon experiments (chat76)						
F_{NTmax} [N]	96.5	-	-	63.8	34.1	35.4
F_{NTrest} [N]	15.4	-	-	10.5	16.1	24.5
$F_{NTmean} \pm F_{NTstd}$ [N]	40.8 ± 26.1	-	-	27.3 ± 17.4	21.6 ± 5.6	24.8 ± 3.4
$F_{NTmedian}$ [N]	30.4	-	-	18.2	19.8	24.8
$P_{NTmedian}$ [kPa]††	12.0	-	-	7.2	7.8	9.8
Electrical stimulation experiments (eStim)						
F_{NTmax} [N]	9.2	55.8	41.7	90.7	-	-
F_{NTrest} [N]	5.1	8.6	8.9	14.1	-	-
$F_{NTmean} \pm F_{NTstd}$ [N]	5.5 ± 0.8	12.9 ± 7.3	13.1 ± 9.3	23.5 ± 20.9	-	-
$F_{NTmedian}$ [N]	5.2	8.7	8.9	14.1	-	-
$P_{NTmedian}$ [kPa]††	2.0	3.4	3.5	5.6	-	-
F_{ILmax} [N]$$	60.9	184.3	155.1	85.0	-	-

*Prematurely explanted (during eStim experiments, SN066.2 and SN066.1 was implanted subM as replacement)
†No data obtained due to supportive equipment malfunction
$For whole *pectoralis major* muscle (combined clavicular, sternal and ribs portions)
‡For $\rho_m = M_m/V_m$
**For $L_m/L_m^0 = 1$ (see Eq. (9))
††Pressure exerted on IPM with principal surface area of 2539 mm^2
$$Mean and maximum values of peaks extracted from F_{IL} data

Table 12: In vivo force measurement of 12 mm Chatillon experiments

Description	Test subject information													
Manual external compressions with 12 mm endplate experiments (chat12) - SN068 & SN069														
Baboon #	447							449						
Explant mass [kg]	24.7							23						
Implant position	SubM							SubM						
Implant side	R							L						
IPM device #*	SN068							SN069						
Sensor #	s1	s2	s3	s4	s5	s6	Total‡‡	s1	s2	s3	s4	s5	s6	Total‡‡
F_{NTmax} [N]	22.49	4.78	19.24	27.81	30.29	96.13	182.6	57.23	10.40	19.84	59.44	54.97	179.28	328.4
F_{NTrest} [N]	2.2	0.9	1.7	3.1	1.4	2.8	21.8	3.3	1.5	1.9	3.4	2.6	4.1	30.1
$F_{NTmean} \pm F_{NTstd}$ [N]	2.6 ± 2.3	0.9 ± 0.5	1.9 ± 1.8	3.6 ± 3.2	2.6 ± 4	5.3 ± 10.7	30.2 ± 18.9	10.1 ± 11.6	1.5 ± 0.4	1.8 ± 1.4	3 ± 2.3	3.2 ± 4.9	10 ± 16.4	53.2 ± 35.2
$F_{NTmedian}$ [N]	2.2	0.9	1.6	3.1	1.4	2.6	22.4	3.3	1.5	1.7	3.0	2.4	4.1	37.6
$P_{NTmedian}$ [kPa]††	0.9	0.3	0.6	1.2	0.5	1.0	8.8	1.3	0.6	0.7	1.2	1.0	1.6	14.8
Manual external compressions with 12 mm endplate experiments (chat12) - SN076 & SN074														
Baboon #	575													
Explant mass [kg]	20.7													
Implant position	SubM							SubQ						
Implant side	R							L						
IPM device #	SN076							SN074						
Sensor #	s1	s2	s3	s4	s5	s6	Total‡‡	s1	s2	s3	s4	s5	s6	Total‡‡
F_{NTmax} [N]	16.062	6.2534	9.457	11.45	8.9373	20.552	56.3	21.306	6.6921	507.05	7.4792	4.468	19.779	937.7
F_{NTrest} [N]	6.1	0.9	0.6	4.6	0.9	2.7	28.1	1.5	5.3	272.8	1.6	0.5	4.6	514.1
$F_{NTmean} \pm F_{NTstd}$ [N]	6.2 ± 1.7	1 ± 0.4	1 ± 1.2	4.4 ± 0.9	1 ± 1	3.2 ± 2.7	30.1 ± 5.3	5.3 ± 3.4	4.7 ± 1.1	192 ± 104.6	1.5 ± 1	0.6 ± 0.4	4.7 ± 2.8	374.9 ± 189.4
$F_{NTmedian}$ [N]	6.0	0.9	0.6	4.5	0.8	2.5	28.3	5.4	4.8	243.3	1.5	0.5	4.4	462.0
$P_{NTmedian}$ [kPa]††	2.4	0.3	0.2	1.8	0.3	1.0	11.1	2.1	1.9	95.8	0.6	0.2	1.7	181.9

*SN064 and SN071 that were prematurely explanted are not indicated in this table

††Pressure exerted on IPM with principal surface area of 2539 mm^2

‡‡Total normal force calculated using Eq. (8)

Table 13: Resting force measured by individual sensors (F_{Nrest}) and calculated total resting force on the principle surface of IPM (F_{NTrest}). All forces are in Newtons.

SN068	**s1**	**s2**	**s3**	**s4**	**s5**	**s6**	**Total‡‡**	**Individual sensors**	
Series of experiments								**mean ± std**	**max**
Conscious exp.	1.2	1.9	1.2	0.9	1.1	1.6	14.3	1.3 ± 0.4	1.9
ROM	0.4	0.7	0.6	0.9	0.9	2.0	9.8	0.9 ± 0.6	2
Chat76	3.0	0.7	0.6	1.7	1.1	1.4	15.4	1.4 ± 0.9	3
Chat12	2.2	0.9	1.7	3.1	1.4	2.8	21.8	2 ± 0.9	3.1
eStim	0.3	0.6	0.0	0.6	0.6	0.7	5.1	0.5 ± 0.3	0.7
SN069	**s1**	**s2**	**s3**	**s4**	**s5**	**s6**	**Total‡‡**	**Individual sensors**	
Series of experiments								**mean ± std**	**max**
Conscious exp.	2.2	1.6	1.9	1.6	1.7	4.2	23.7	2.2 ± 1	4.2
ROM	0.8	0.9	2.2	1.8	1.3	2.1	16.3	1.5 ± 0.6	2.2
Chat76	0.9	0.5	0.7	1.5	0.6	1.6	10.5	1 ± 0.5	1.6
Chat12	3.3	1.5	1.9	3.4	2.6	4.1	30.1	2.8 ± 1	4.1
eStim	0.6	0.5	2.9	0.6	0.8	2.5	14.1	1.3 ± 1.1	2.9
SN076	**s1**	**s2**	**s3**	**s4**	**s5**	**s6**	**Total‡‡**	**Individual sensors**	
Series of experiments								**mean ± std**	**max**
Conscious exp.	4.4	1.1	1.1	4.2	2.4	2.9	28.7	2.7 ± 1.4	4.4
ROM	2.0	0.7	0.5	2.4	0.5	1.8	14.1	1.3 ± 0.9	2.4
Chat76	1.9	1.1	0.7	2.7	1.3	1.3	16.1	1.5 ± 0.7	2.7
Chat12	6.1	0.9	0.6	4.6	0.9	2.7	28.1	2.6 ± 2.3	6.1
eStim	-	-	-	-	-	-	-	-	-
SN074	**s1**	**s2**	**s3**	**s4**	**s5**	**s6**	**Total‡‡**	**Individual sensors**	
Series of experiments								**mean ± std**	**max**
Conscious exp.	3.8	0.8	2.9	0.7	0.5	1.0	17.6	1.6 ± 1.4	3.8
ROM	1.9	3.0	2.3	0.2	0.5	0.8	15.6	1.4 ± 1.1	3
Chat76	3.3	5.7	2.5	0.3	0.6	1.1	24.5	2.3 ± 2.1	5.7
Chat12	1.5	5.3	272.8	1.6	0.5	4.6	514.1	47.7 ± 110.3	272.8
eStim	-	-	-	-	-	-	-	-	-
SN066.1	**s1**	**s2**	**s3**	**s4**	**s5**	**s6**	**Total‡‡**	**Individual sensors**	
Series of experiments								**mean ± std**	**max**
eStim	0.0	2.7	0.8	0.6	0.8	0.0	8.9	0.8 ± 1	2.7
SN066.2	**s1**	**s2**	**s3**	**s4**	**s5**	**s6**	**Total‡‡**	**Individual sensors**	
Series of experiments								**mean ± std**	**max**
eStim	0.0	2.6	0.8	0.6	0.8	0.0	8.6	0.8 ± 0.9	2.6

‡‡Total normal force calculated using Eq. (8)

C. Results of the strongest intraspecific correlation obtained from linear regression analysis

The results of the intraspecific correlation of case C of Table 7 are given below. It includes the regression summary (Table 14), Analysis of variance (ANOVA, Table 15), correlations of regression coefficients matrix (Table 16), histogram of the residuals (Figure 53), normal probability plot of the residuals (Figure 54) and a plot of the observed F_{NT} values vs. the residuals (Figure 55).

The correlating different regressors to each other individually resulted in feasible correlations interpretable at the hand of physical factors. This observation was evident from the regression coefficients matrix, which yielded no irregularities. The normal probability plot and histogram of the residuals revealed an acceptable normal distribution of the residuals. Furthermore, plotting the residuals against the observed F_{NT} response also did not present any obvious systematic residual distribution patterns evident of model misspecification.

Table 14: Summary of multiple linear regression analysis performed for case C of Table 7.

N=51	**Regression Summary for Dependent Variable: F_{NT} [N]** **R= .83994793; R^2= .70551252; Adjusted R^2= .67990491** **F(4,46)=27.551; p<.00000; Std.Error of estimate: 12.693**					
	Beta	**Std.Err. of Beta**	**B**	**Std.Err. of B**	**t(46)**	**p-level**
Intercept			-1055.78	126.1576	-8.36874	0.000000
F_{IL} [N]	-0.592421	0.300270	-0.24	0.1217	-1.97296	0.054527
L_m^{meas} [mm]	1.897869	0.209917	3.24	0.3588	9.04103	0.000000
$w_{m,IPM}$ [mm]	1.535595	0.200890	5.95	0.7784	7.64397	0.000000
σ_m [kPa]	1.175980	0.308209	434.62	113.9087	3.81553	0.000404

Table 15: Analysis of variance (ANOVA) of the multiple linear regression analysis performed for case C of Table 7.

Effect	**Analysis of Variance; DV: F_{NT} [N]**				
	Sums of Squares	**df**	**Mean Squares**	**F**	**p-level**
Regress.	17754.10	4	4438.524	27.55090	0.000000
Residual	7410.72	46	161.103		
Total	25164.82				

Table 16: Correlations of the regression coefficients of the multiple linear regression analysis performed for case C of Table 7.

Variable	**Correlations of Regression Coefficients B; DV: F_{NT} [N]**			
	F_{IL} [N]	**L_m^{meas} [mm]**	**$w_{m,IPM}$ [mm]**	**σ_m [kPa]**
F_{IL} [N]	1.000000	-0.340097	-0.259748	-0.962665
L_m^{meas} [mm]	-0.340097	1.000000	0.913277	0.387071
$w_{m,IPM}$ [mm]	-0.259748	0.913277	1.000000	0.288321
σ_m [kPa]	-0.962665	0.387071	0.288321	1.000000

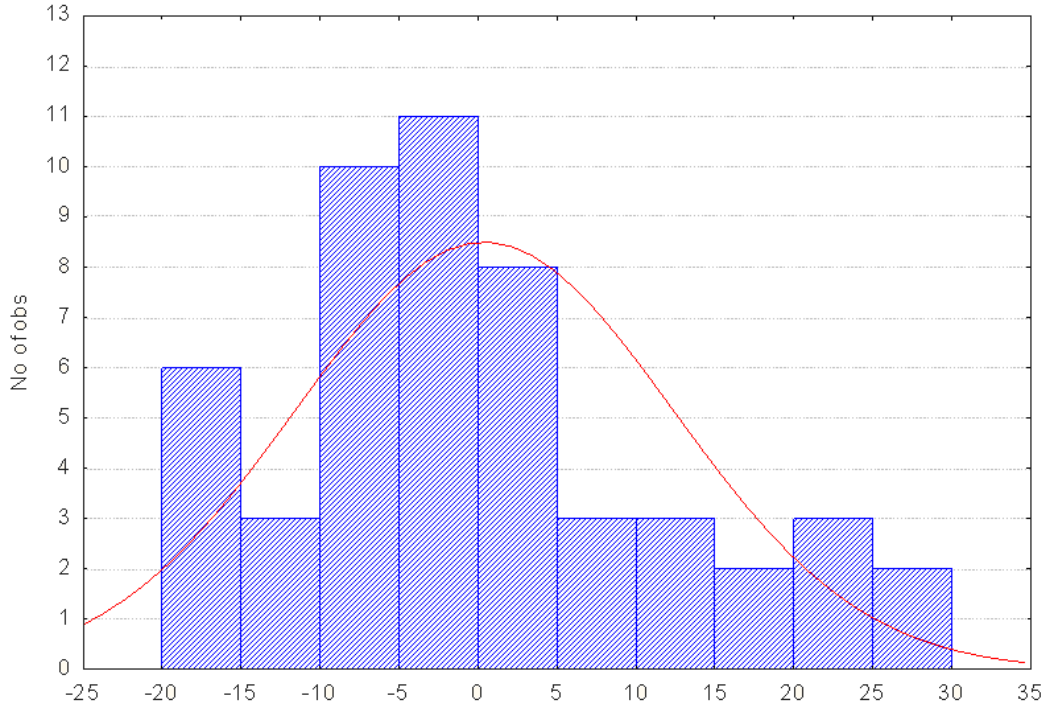

Figure 53: A histogram showing the distribution of residuals obtained from the multiple linear regression analysis performed for case C of Table 7. The smooth line shows the expected normal.

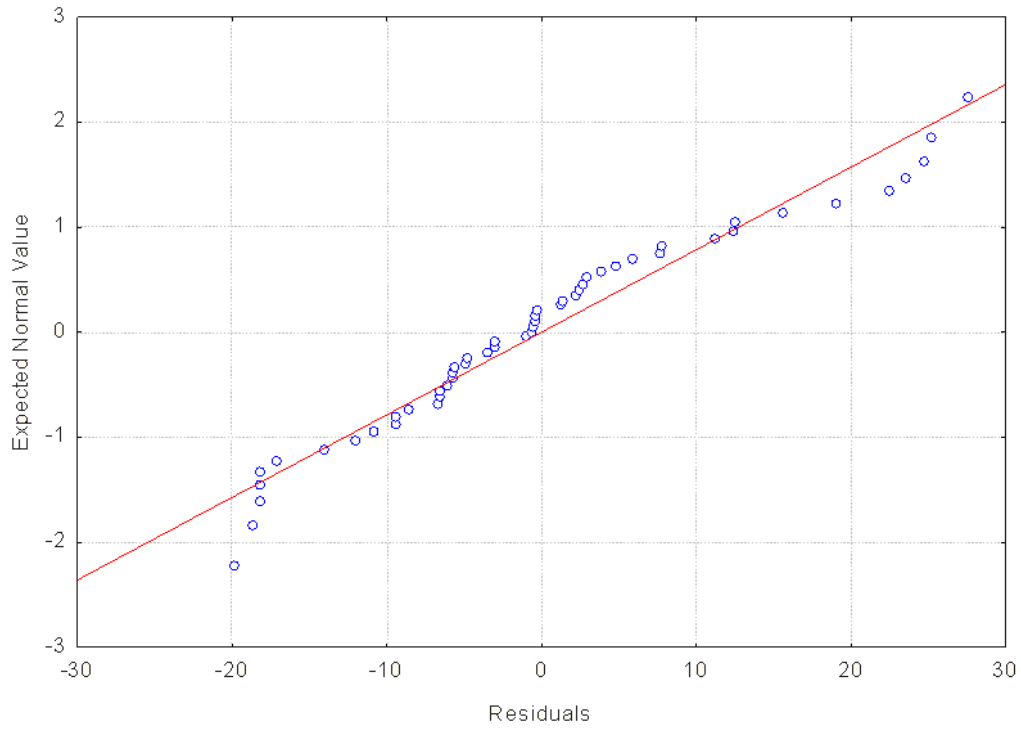

Figure 54: Normal probability plot of the residuals which shows the expected normal values against the corresponding residual values, obtained from the multiple linear regression analysis performed for case C of Table 7.

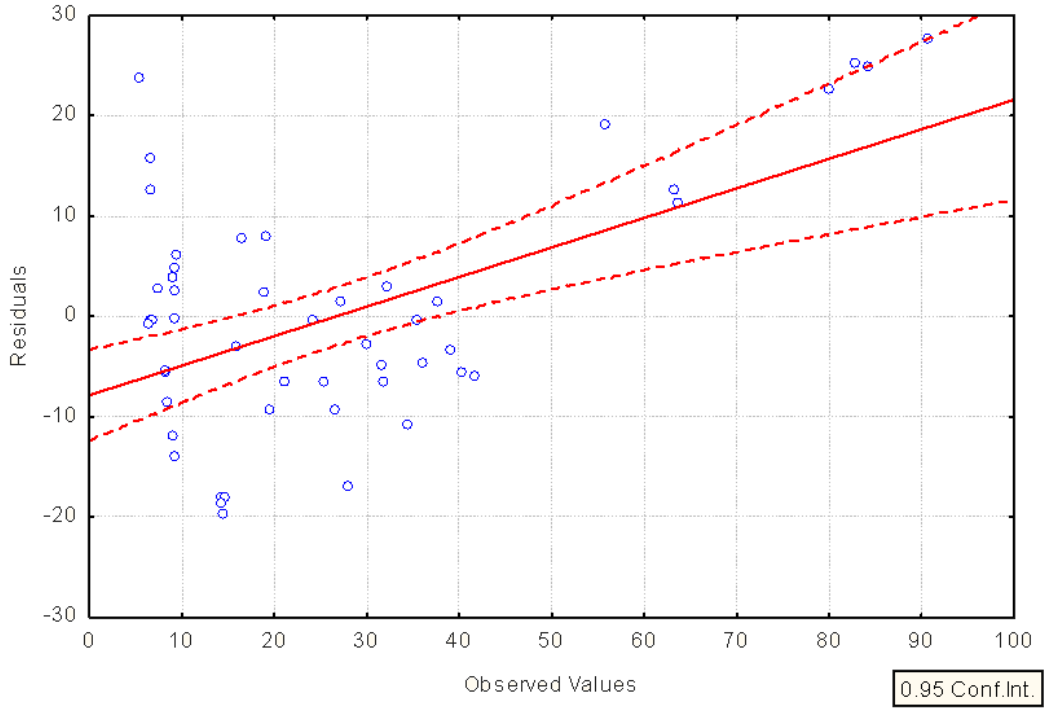

Figure 55: Observed values of F_{NT} against the corresponding residuals, obtained from the multiple linear regression analysis performed for case C of Table 7.